A Novel Foldable Stent Graft

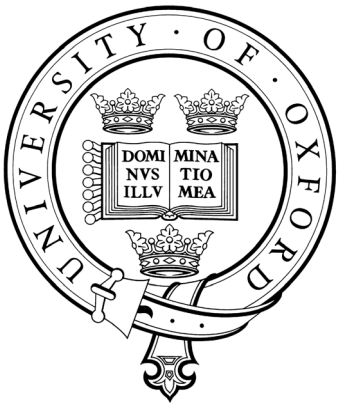

Kaori Kuribayashi

St. Catherine's Collage Oxford

Thesis submitted for the degree of Doctor of Philosophy
in the Department of Engineering Science
at University of Oxford
Trinity Term, 2004

To my parents

ABSTRACT

A Novel Foldable Stent Graft

Kaori Kuribayashi

St. Catherine's College
A dissertation submitted for the degree of Doctor of Philosophy
in Department of Engineering Science at University of Oxford, Trinity Term 2004

This dissertation concerns the structural design of medical stent grafts. A new type of an innovative stent graft has been developed. Unlike the conventional stent grafts which consist of a wire mesh and a covering membrane, the proposed stent graft can be made from a single folded sheet of material.

Firstly, a detailed symmetric design of a foldable cylindrical tube for the new stent graft has been presented. Folding is achieved by dividing the structure into a series of identical elements with hill and valley folds as in origami (Japanese art of paper folding). The folding patterns allow the stent graft to be folded and expanded both radially and longitudinally. The relationships among the design of the elements, the number of elements in the circumferential and longitudinal directions and the folded dimensions of the stent graft have been derived. It has been found that compact folding in the radial direction can be achieved by increasing the number of circumferential elements. A geometric mismatch during deployment has also been identified. The elements have to deform when the structure is expanded. Optimum designs which minimise the deformation have been found.

Secondly, a new stent graft with helical folds has also been designed to improve radial strength and ease the deployment process. Helical folds are introduced by adjusting the joining position of the two edges of a sheet that had been symmetrically jointed in the symmetric design. The relationships among the number of elements in one complete circumference of a helix, the helical angle and the radius of the helical type stent graft have been established. The locations for the helical folds are optimised for easy folding by considering both geometric aspects of folding and the buckling patterns of a thin-walled tube under torsion, which are found analytically.

Thirdly, using numerical analysis of the finite element method (FEM) the strain level and overall deformation of the stent graft during deployment has been calculated.

Finally, the stent graft has been manufactured to verify the concept. A number of prototypes of the stent graft, which are the same size as standard oesophageal and aortal stent grafts, have been produced successfully using the same materials as current stent grafts of stainless steel and shape memory alloy (SMA) sheets. The patterns of folds on the materials are produced by photochemical etching. It has also been demonstrated that the SMA stent grafts self-expand smoothly and gradually by a near body temperature.

Keywords: stent graft, structural design, foldable structure, helical structure, geometric analysis, numerical analysis, shape memory ally sheet, photochemical etching.

ACKNOWLEGEMENT

This work described in this dissertation was carried out in the Department of Engineering Science at the University of Oxford. I really enjoyed my research. This dissertation could not be accomplished without the co-operations of so many people. I extend my sincerest thanks and gratitude.

The long list of acknowledgement must begin with Dr. Zhong You. He gave me a lot of wonderful opportunities at the University of Oxford. He directed me into the field of deployable structures. I enjoyed our discussion, which always brought me many interests.

I would like to thank Professor Gilliane Sills, my college advisor, for her support and encouragement. Many people at the Department of Engineering Science helped me with my work at various stages. I have had wonderful colleagues from 18 different countries, which is amazing. In particular, my thanks must go to Gwyn Lintern. Thanks to Richard Kelly, Nguyen Giang Kenneth Kar, Nguyen Lam, Yan Chen, Jackie Sim, Andras Lengyel, Davide De Focatiis, Miguel Pena, Gert Bartholomeeusen, John Pickhaver, Sotiris Psomas, Claus Wisser, Mark Poter, Clive Baker and Alison Payne. Their great friendships, and contribution to many memorable and enjoyable occasions are appreciated.

I would also like to extend my gratitude to Mr. Cyril Band who assisted me on photochemical etching on top of his already busy schedule. Also, he and his partner Penny Gledhill make me feel that England is my second home. I will never forget their warm support. I would like to acknowledge Dr. Koichi Tsuchiya for supplying shape memory alloy sheets, his useful discussions and encouragement. I also would like to thank Dr. Neil Morgan, Dr. Peter Leigh for having useful discussions and helps.

In Oxford, I had met so many interesting, energetic and ambitious people. Thanks to Stephen Lui, Mei Yi Lok, Alex Hearn, Bob Goodson and Jenna Phillips and Michelle Chew.

Financial support of Kobe-Oxford scholarship is gratefully acknowledged. I would also like to thank the British Council for supporting my research in Japan. Thanks to St. Catherine's College for the support of several travel funds to attend conferences and workshops. I also thank ISIS innovation for the support the application of an international patent.

Most importantly, I express my greatest gratefulness to my parents, my brother and sister and all my family members for their tremendous support. I am also extremely grateful to my boyfriend, Takafumi Shigetomi for his huge support and encouragement from Japan. To all of them I cannot thank you enough.

I hope that the idea of the new stent graft will become a real product and it could help many patients in the future.

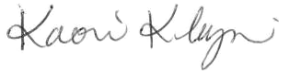

Kaori Kuribayashi

CONTENT

CHAPTER 1 INTRODUCTION

CHAPTER 2 REVIEW OF PREVIOUS WORK

PART I DESIGNS AND ANAYSIS

CHAPTER 3 FOLDABLE CYRINDRICAL TUBES AS A NEW STENT GRAFT

PART II MANUFACTURE

CHAPTER 6 MANUFACTURING AN ORIGMI STENT GRAFT

CHAPTER 7 FINAL REMARKS

NOATION

Some symbols for the variable s and parameters used in this dissertation are provided here.

Capital letters:

A: Width of line in the developed photoresist.

A_f: Temperature of finishing of austenite crystal structure.

A_s: Temperature of starting of austenite crystal structure.

B: Width of the line after etching.

E: Young's modulus.

H_A: Helical lines of a single long fold spirally around the circumference of the helical-type cylindrical tube.

H_B: Helical lines of the helical-type cylindrical tube run diagonally from one open end to the other.

M: Mean value of $|y|$ during deployment.

M_f: Temperature of finishing of martensite.

M_s: Temperature of starting of martensite.

M^*: B19' martensitic transformation temperature.

N_{yx}: Buckling shear stress.

L: Total length of the foldable cylindrical tube.

L^*: Radio of the value of L in the fully folded configuration respect to in the fully expanded configuration.

R: Radius of the specimen after heating.

R_0: Radius of the roller for the bending test.

R_{o1}: Outer radius between node O_0 and B of the foldable cylindrical tube.

R_{o2}: Outer radius between node O_0 and A of the foldable cylindrical tube.

R_f: Temperatures of finishing of R phase martensite crystal structure.

R_i: Inner radius between node O_0 and O of the foldable cylindrical tube.

R_s: Temperature of starting of R phase martensite crystal structure.

R^*: Radio of the value of R_{o1} in the fully folded configuration respect to in the fully expanded configuration.

R^*_m: R phase martensitic transformation temperature.

U: Undercut.

Small letters:

d: Etching depth.

h: Effective thickness of the shell $h = t/\sqrt{1-\nu^2}$.

m: Number of the element in horizontal or circumference directions of the foldable cylindrical tube.

m_b: Number of the buckling line of peak folds.

n: Number of the element in vertical or longitudinal directions of the foldable cylindrical tube.

n_A: Position of the nods at the centre folds of FE model.

n_b: Slope of the buckling lines.

n_h: Number of hill folds.

n_t: Total number of folds.

n_x: Number of the elements at the groove in the x - axis.

n_y: Number of the elements at the groove in the y - axis.

n_z: Number of the elements at the groove in the z - axis.

n_v: Number of valley folds.

l : Length between nodes A and B.

l_a: Length between nodes $E_2A_1$and F_2B_1.

l_o: original length between nodes A_1 and B_1

t: Thickness of the cylindrical tube.

y: Value of $(R_{o1}\text{-}R_{o2}) / l$.

w_g: Width of the groove at the centre of the FE model.

w: Displacement in the radial direction under torsion.

Greek letters:

α_1: Angle, $\angle DAO$.

α_2: Angle, $\angle DAB$.

β_A: Angle of H_A with respect to the horizontal base line.

β_B: Angle of H_B with respect to the horizontal base line.

δ: Central angle, $\angle AO_0C/2$.

δ_b: Angle between the buckled line and the x - axis.

ε: Strain of bended surface.

ϕ: Angle, $\angle AO_oC'/2$.

φ: Angle, $\angle BQO'$.

ν: Poison's ratio.

θ: Deployment angle, $\angle ABC/2$.

Θ_i: Angles between the folding line with respect to the horizontal $i = 1, 2, 3\cdots$.

θ_0: Deployment angle when the cylindrical tube is fully folded.

θ_1: Deployment angle when the cylindrical tube is fully expanded.

ξ: Angle between the folds between nodes O and B and nodes O and P.

CHAPTER 1

INTRODUCTION

This introduction contains a short description of the issues that initiated this D.Phil dissertation, including a background and historical outline of stents and stent grafts. The aim and scope of the research are outlined, followed by a layout of this dissertation.

1.1 Background of stents and stent grafts

A stent is a type of flexible tubular medical device which is capable of being folded into small dimensions for minimum invasive surgery, and then expanded to open up a blocked organ and also to protect a weakened wall in the human body. There are two types of stents: ordinary stents, made of a wire frame, and stent grafts in which a thin cover attaches to the stent. They are used, for example, in the treatment of such diseases as stenosis, aneurysm or cancer. Compared with traditional methods (e.g. open surgery, radiotherapy or chemotherapy) minimum invasive surgery using stents causes less pain and scarring and reduces recovery time for the patient, as well as providing lower health-care cost (Fischman, et al. 1994; Serruys, et al. 1994).

Figure 1.1 illustrates the stent treatment for a blocked coronary artery caused by arteriosclerosis. Arteriosclerosis is a disease caused by hardening of the arterial walls due to deposits of plaque including lipids, cholesterol crystals and calcium salts, which narrow and reduce the space available for blood flow. Coronary artery disease is the largest killer, responsible for more than one of every five deaths in 2003, according to the American Heart Association.

Figure 1.1 Illustration of a stent treatment of a narrowed artery (source: Heart Center Online).

(a) (b)

Figure 1.2 Telescopic views of (a) before and (b) after stent treatment of an oesophagus cancer (source: Livingston).

As shown in Figure 1.1, a stent is made from wire mesh in a tubular profile. It is folded into a catheter so that it can be delivered from a femoral artery with very small incision in the groin to the diseased artery. A balloon initially placed inside the folded stent is then inflated to expand the stent. The balloon and catheter are subsequently removed, while the stent remains permanently in place. The stent is also used for the treatment of cancer (Chung and Qadir 1998; Cowling and Adam 1998; Roseveare, et al. 1998). Figure 1.2 shows photographs of a blocked oesophagus due to cancer before and

after the stent treatment (Livingstone). It can be seen that the passage is dramatically improved.

The term *stent* appeared in the late 19th century, derived from the splint used by British dentist Charles Stent to stabilise skin grafts. More than half a century later, in 1964, Dr. Charles Dotter first tried using polymer tubes in arteries to treat arterial shrinkage, which was followed by later attempts of using wire coils made from stainless steel (Kutryk and Serruys 1999). Before the stent became a routine clinical implantation, a balloon angioplasty was widely performed to open a blocked site in the body (Gruntzig, et al. 1979). However, re-occlusion occurred after removal of the balloon because of the elastic recoil of the artery wall. To overcome the limitation of the balloon, angioplasty stents were developed. The stent techniques have improved dramatically in the last twenty years and are now widely used in various locations throughout the body (Adam, et al. 1997). The success of stent technology is best illustrated by its rapidly expanding market, which approached a total of $2 billion in 2003 and is expected to reach $5 billion by 2005 (Smith 2002).

Compared to angioplasty treatment, the ratio of restenosis after insertion of the stent reduces to 15-20% from 33%-50% (Kurnik and Martens 2003). Unfortunately, restenosis is still a problem with the stent as the surrounding tissue grows through the netting and blocks the lumen (Edelman and Rogers 1996; Gottsauner-Wolf, et al. 1996). When this happens, it is not possible to remove the stent. Thus, it is quite normal that additional stents are placed inside the original stent to reopen the blocked lumens.

Stent grafts, consisting of a thin membrane/graft around a wire mesh stent, have been developed as an effective way for preventing restenosis (Hills, et al. 1998; Watson 1998). A typical example is shown in Figure 1.3(a). The stent graft is also used for supporting a weakened wall, such as that occurring during an aortic aneurysm, see Figure 1.3(b).

Figure 1.4 shows x-ray angiograms before and after the implantation of a stent graft (Kawaguchi and Ishimaru 2002). Figure 1.4(a) shows a thoracic aortic aneurysm. Considered high risk for open surgery, the patient was referred for endovascular repair with a stent graft. A complete exclusion of the aneurysm is shown in Figure 1.4(b).

The figure originally presented here cannot be made available via ORA for copyright reasons.

(a) **(b)**

Figure 1.3 (a) A TALENT stent graft made by World Medical (source: Dolmatch, 2000). (b) Illustration of the stent graft for supporting weakened aorta aneurysm (source: Adam, 1997).

The figure originally presented here cannot be made available via ORA for copyright reasons.

(a) **(b)**

Figure 1.4 Angiograms of a thoracic aortic aneurysm (a) before and (b) after implantation of stent graft (source: Kawaguchi, 2002).

The first endovascular stent graft repair to an abdominal aortic aneurysms (AAA) was performed by Parodi, Palmz and Barone in 1991 (Parodi, et al. 1991). In the following years the treatment of a thoracic aortic aneurysm (TAA) with the stent graft was first carried out by Dake and Mitchell (Dake, et al. 1994; Mitchell 1997). Approximately 205,000 new patients are diagnosed with aortic aneurysm each year. Presently approximately 100,000 procedures per year are performed worldwide. Compared with the conventional treatment for aortic aneurysm of open surgery which carries significant health risks for many older patients, the stent graft repair procedure is much superior, so that it is expected to expand from about 40% of the total patients treated in 2002 to 67% in 2007[1]. To overcome the complications of the stent grafts and to achieve this expected market expansion, the stent graft designs, delivery and expansion devices, surgical monitoring devices, and stent graft procedures need to be improved. An important aspect is the improvement of the stent graft structural design, as described below.

As shown in Figure 1.3, the typical stent grafts currently in use consist of two pieces: an expandable wire mesh stent and a soft covering membrane. The membrane is either attached to the stent at proximal and distal ends only, or it is stitched more securely on the outside or inside of the wire stent at discrete points to avoid geometric incompatibility between the stent and its cover. Therefore, it is common that uneven distribution of stress or entanglement on the cover material occur due to both the deployment and to the plastic motions in the aorta after insertion. These stress on the cover result in stent graft fatigue (Chuter 2002; Drake 2003).

Figure 1.5 shows various forms of stent graft fatigue including metallic fractures, fabric ruptures and suture breakages. These failures cause endoleaks (persistent flow into the aneurysm through the stent graft), aneurysm ruptures and death (Jacobs, et al. 2003; Jacobs, et al. 2003).

[1] AAA Stent Grafts, Still Under Scrutiny, "*Medtech Insight*" Aug. 2003

(a) **(b)** **(c)**

Figure 1.5 Clinical examples of fatigue in Boston Scientific Vanguard endovascular graft. (a) and (b) Structure disruption and (c) fabric fatigue and wear holes on prosthesis surface (source: Jacobs, 2003a,b).

Migration of the stent grafts due to inadequate fixation or as a result of material fatigue is also a problem of AAA and TAA stent grafts (Drake 2003). Furthermore, the complicated design of the stent grafts, such as the stitching of the membrane over the stent (Figure 1.3b), leads to high manufacture costs. Hence some doctors make stent grafts by themselves, which leads to an inconsistency in their quality and reliability (Matsumoto 1999).

1.2 Aim and scope

The aim of the work described in this dissertation is to improve the structural design of stent grafts by developing a new type of a single piece stent graft. The new stent graft has an integrated cover with much simpler geometry and no compatibility problem between wire stent and cover. The expanding mechanism of wire mesh and cover will

be considered together. In addition, it has a more reliable expanding performance and lower manufacture cost than the currently available two-piece stent grafts.

A current trend in stent and stent graft research is to develop a drug-eluting stent to prevent restenosis for cardiovascular stents, and to grow tissues so that biological anchors can be produced at the aortic wall (Hiatt, et al. 2001; Schwertz and Vaitkus 2003; Wey, et al. 2003). There have been very few investigations of the structural aspects of the stents or stent grafts. The research work presented in this desideration will focus on the structural aspects of the improved stent graft.

The project includes the geometrical conceptual design of the stent graft, and the analysis and manufacture of a novel stent graft for oesophageal and aortal diseases. The stent grafts presented in this dissertation are named *origami stent grafts* due to the fact that paper folding patterns used in the Japanese art of origami are employed to produce the tubular stent grafts.

1.3 Layout of dissertation

This dissertation consists of two major topics: design and analysis of the origami stent graft, and its manufacture.

A brief overview of previous work is given in Chapter 2. Design characteristics of existing stents and stent grafts, stenting techniques, and the engineering aspects of stents are reviewed. The possibilities of applying principals of foldable structures and origami paper folding techniques are discussed. An overview of materials, such as stainless steel and shape memory alloy which are used in existing stents, is also given.

Chapters 3, 4 and 5 address the first theme of this dissertation: the design and analysis of the origami stent graft. In Chapter 3, families of folding patterns for a foldable cylindrical tube are presented. Key dimensions such as radius and length of the origami stent grafts are examined in detail. To understand the deployment process, the

fold-shortening during deployment is calculated, which is useful to determine the optimum design for the stent graft.

In Chapter 4, a foldable cylindrical tube with helical lines as part of the folding patterns in order to increase radial stiffness is introduced. The geometric properties of the tube such as helical angle, radius and deformation are defined and analysed. Moreover the buckling pattern of a folded thin-walled tube under torsion, which consists of a set of folds, is considered to optimise the locations of the folds for the origami stent graft with helical lines.

In Chapter 5, using numerical analysis of the finite element method (FEM), strain and deformation of the folds in the stent graft in its folded configuration is calculated. The deformed shape of a thin cylindrical tube without any folds is also identified and is compared with the pattern of folds for the origami stent graft.

The second theme of the dissertation is contained in Chapter 6: manufacture of the origami stent graft. The stent graft is manufactured using stainless steel sheets and two types of Titanium/Nickel (TiNi) shape memory alloy (SMA) sheets. The patterns of folds on stainless steel sheet are produced by photochemical etching. Processing techniques, such as photochemical etching and heat-treatment of SMA sheets are investigated. The self-expansion of the origami stent grafts with SMA by heat is also explored.

Chapter 7 contains conclusions and discusses future requirements.

CHAPTER 2

REVIEW OF PREVIOUS WORK

This chapter reviews three main topics. Firstly details of designs and characteristics of existing stents and stent grafts are presented and the engineering aspects of stent research are summarised. Secondly principles of foldable structures and mathematical aspects of origami paper folding are presented and the possibility of their applications to stent graft design are discussed. Thirdly an overview of stainless steel and shape memory alloy, which are used in the manufacture of existing stents and stent grafts, is given.

2.1 Design characteristics of stents and stent grafts

Stents and stent grafts are classified into three categories according to the anatomical location in which they are used: (i) coronary (blood vessels that supply the heart), (ii) peripheral (any other blood vessel), and (iii) non-vascular (parts of the digestive tract).

In structural terms, currently available stents can be classified as coil, mesh and slotted tubular stents (see Figure 2.1). Coil stents consist of zig-zag wires, mesh stents are made by netting metric wires, and slotted tubular stents are made of laser cut tubes. All of these are made mainly of two types of alloys: stainless steel and shape memory alloy (nickel and titanium alloy). The thickness of the struts is between 50 and 140 μm. A biodegradable poly-*l*-lactic acid (PLLA) stent has also been developed (Labinaz, et al. 1995; Tamai, et al. 2000). Unlike metallic stents which remain in the body permanently and may be obstacles to additional treatments (e.g., repeat angioplasty and bypass surgery), temporary biodegradable stents may be an ideal alternative to metallic stents in terms of compliance and tissue responses. Key features of these stents include high

(a) **(c)**

Figure 2.1 Existing stents. (a) Coil stent (Spiral Z, Cook); (b) slotted tubular stent (Palmaz-Schatz, Cardis/J&J) and (c) mesh stent (Wallstent, Boston Scientific).

expansion rate, high strength, good flexibility and good tractability (Flueckiger, et al. 1994; Phillips, et al. 1998; Kutryk and Serruys 1999; Dyet, et al. 2000).

A stent graft, also known as a covered stent, is composed of one of the above-mentioned stents with an attached synthetic material cover. Table 2.1 lists abdominal aortic aneurysm (AAA) stent grafts. Some of the stent grafts have a tubular shape, see Figure 2.2(a), while others are branched, see Figure 2.2(b).

The ideal material of the stent graft is flexible and thin, which provides for the capability of the stent being folded into small dimensions for minimum invasive surgery, and a high level of stiffness to avoid material damage. The most common covers for stent grafts include a thin knitted membrane of PTFE (poly-tetra-fluoro-ethylene) and woven polyester of Dacron, which have been widely used as artificial grafts in blood vessels. Their thickness is between 0.1 and 0.3 mm.

Table 2.1 AAA stent graft systems

Product name	Manufacturer	Stent material	Graft material	Diameter (mm)	Delivery Diameter (Fr.)[2]
AneuRX	Medtronic	nitinol	Dacron	20-28	21
Ancure	Guidant	stainless steel	Dacron	20-26	27
Excluder	W. L. Gore & Assoc.	nitinol	PTFE	-	18
Zenith	Cook	stainless steel	Dacron	-	18, 20
Lifepath AAA	Edwards Lifesciences/Baxter	Elgiloy	Dacron	20-28	21
Talent	World Medical Inc.	stainless steel	Dacron	18-38	22, 24
Carvita	Carvita	Elgiloy	corethane	5-45	21
Aruba	Cordis/J&J	nitinol	Dacron	-	-
Vangaurd III	Boston Scientific	nitinol	Dacron	22-26	21

The figure originally presented here cannot be made available via ORA for copyright reasons.

(a) **(b)**

Figure 2.2 Two existing stent grafts.

(a) Excluder (W. L. Gore & Assoc) and (b) AneuRx (Medtronic).

[2] 1Fr. = 0.33 mm.

The most important parameters of the stents and stent grafts are the diameters and lengths in fully folded and expanded configurations. Normally, the stent or stent graft whose diameter is 10-20% larger than the vessel diameter is used so that they can anchor to the vessel wall when expanded. The dimensions of stents and stent grafts for cardiovascular use are around 4-6 mm in diameter and 10-40 mm in length in their fully expanded configuration. They are folded into a catheter of 2-3 mm (6-7 Fr.). The dimensions of stents and stent grafts for aorta or oesophagus are 10-40 mm in diameter and 30-60 mm in length when fully expanded. They are compressed into a catheter of 7-8 mm (18-24 Fr.) (Esato, et al. 1999). Examples of the expansion diameter of the AAA stent grafts and the size of the catheter are shown in Table 2.1.

There are two methods of expansion in use. The first involves a stent being gradually deformed under the influence of a cylindrical balloon inflated from the inside with a deployment pressure of 709-1216 kPa (7-12 atm). Figure 2.3(a) shows photographs taken during the expansion of a stent using this balloon technique. Once the stent is expanded, the balloon is deflated and withdrawn. The other method is self-expansion as shown in Figure 2.3(b). The self-expanding stents and stent grafts are normally made from shape memory alloys. The stent is packed like a compressed spring inside a sheath so that it can be passed through a narrow space. Once it reaches the intended site, the sheath is withdrawn gradually and the stent expands freely to resume its natural enlarged shape. The advantage of the self-expanding stent is that extra expanding tools (e.g., a balloon and air pump) are not required and also, accidents, such as the stent expanding more than the diameter of the lumen due to the high-pressure inflation of the balloon, can be avoided.

(a) **(b)**

Figure 2.3 (a) Deployment sequence of a stent deployed by an inner balloon and (b) a self-expanding stent (source: Kurnik, 1999).

2.2 Engineering research of stents

Most articles published in engineering journals deal mainly with mechanical properties of stents. Experimental studies of the stent have been reported widely. The first study on the deformation characteristics of self-expanding metallic stents was given in 1988 (Fallone, et al. 1988). Agrawal also showed the deformation characteristics of polymeric stents fabricated from poly-*l*-lactic acid (Agrawal and Clark 1992). In these works, the effects of stent diameter and wire caliber were discussed. Schrader discovered that some stents show superior strength to others due to differences in strut diameter, design and metal properties (Schrader and Beyar 1998). Because an increase in the strut diameter not only provides higher stiffness but also reduces the longitudinal flexibility, he suggested that no more than an adequate mechanical support should be considered when designing or selecting stents. Mechanical tests also showed that slotted tubular stents have a greater radial strength to withstand higher external pressures than coil stents (Rieu, et al. 1999).

Mechanical properties of the stents have also been analysed numerically using finite element method (FEM) to understand stent expansion mechanisms, recoil and

structural failure of balloon-expandable stents (Dumoulin and Cochelin 2000; Etave, et al. 2001; Migliavacca, et al. 2002).

Mechanical action of the artery wall after implantation of the stent has also been investigated. A report by Rogers showed that restenosis was due to the damage of cells during the deployment of the stent because of forces imposed on the luminal surface (Rogers and Edelman 1995) The effect of the number of stent struts on tissue in-growth was studied by using mathematical models and clinical tests (Garasic, et al. 2000). 2D FE analysis of balloon-artery interactions during stent placement was presented by Rogers, et al. (1999). 3D FE analysis of the stent-artery interaction during stent deployment was examined by Auricchio, et al. (2000). Stress distribution and the degree of tissue prolapse (i.e. narrowing of the lumen as a result of elastic deformation of the vessel wall) within stented vessels were determined using FEM (Prendergast, et al. 2003).

In vitro tests before animal test are also important to verify stent designs. Expansion force, flexibility, compressibility and stability of stainless steel wire stents were measured by Maeda, et al. (1992). Experimental studies of oesophageal covered stents for preventing migration were carried out using clay to simulate stenosis (Makutani, et al. 2000). The effect of blood flow for the expansion of the stent graft was examined by Kawaguchi and Ishimaru (2002).

2.3 Foldable structures and their applications to stent graft design

Foldable structures are structures that can be folded compactly for delivery and be expanded when necessary. Well-known examples include tents and umbrellas. There are also foldable structures in nature, for instance, a leaf is folded as a bud and expanded when it grows (Kobayashi, et al. 1998). In recent years, there has been an explosion in foldable structure technologies, particularly in the aeronautical fields, where devices such as solar arrays and antennas must be packed into small bundles for

transport, and then expand to become useable. (Miura 1993; You and Pellegrino 1997). Depending on their mechanical behaviour, foldable structures can be classified into two types: mechanisms and deformable structures. Mechanisms do not induce any deformation in the structural components, e.g., a pair of scissors. Deformable structures, on the other hand, are those whose deployment involves deformation of the structure; e.g., balloons and springs.

Two foldable structures most relevant to the design of an expandable stent graft are shown in Figure 2.4. The structure in Figure 2.4(a) is a well-known spatial mechanism forming structure, the deployable hyperbola (Hilbert and Cohn-Vossen 1952). The diameter of this structure decreases when expanded in a longitudinal direction. The problem for applying the concept to stent graft design is that the struts are connected by universal joints, which may significantly increase the complexity of the deployment and cost of manufacture, particularly in small dimensions.

The structure in Figure 2.4(b) is a deformable structure based on the buckling pattern of a thin-walled tube. The buckling process can be reversed if the buckling folds in the collapsed tube are replaced by foldable hinge lines (Guest 1994a). This foldable structure can be folded by shortening the overall length as shown in Figure 2.5. However, the diameter of the structure does not alter very much during expansion, making it unsuitable for use as a stent graft because one of the crucial requirements for a stent graft is that its folding reduces its diameter. Nevertheless, this design indicates that it is possible to produce a collapsible and expandable cylinder using a simple folding pattern rather than a system of complex joints. Jointless structures such as these usually have the simplest structural forms, and are therefore extremely useful for small structures such as the stent grafts.

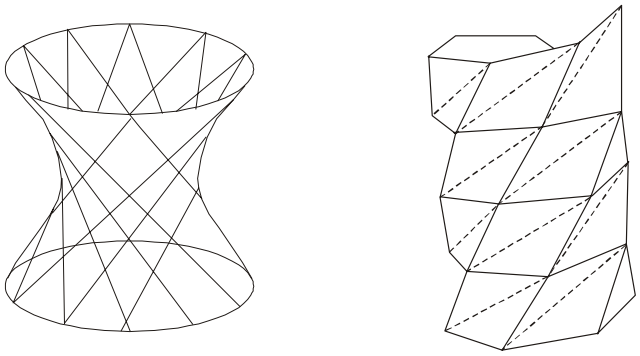

Figure 2.4 Two existing concepts for deployable cylinders: (a) a hyperbola made of straight struts and (b) a collapsible cylindrical tube.

The figure originally presented here cannot be made available via ORA for copyright reasons.

Figure 2.5 Folding sequence of the collapsible cylindrical tube (source: Guest, 1994a).

2.4 Principles of origami

The foldable tube reviewed in the previous section indicates that tubular structures can be folded simply by introducing folds. It is worthwhile to examine the basic mathematics behind origami paper folding methods, as stent grafts are also made from thin membranes.

Origami is an ancient Japanese art. It employs two types of straight folds: namely hill and valley. Most literature gives conditions to enable a sheet to be folded up completely, i.e., it is required that there should be no voids in the package (Fushimi 1980; Miura 1993; Kawasaki 1998; Nojima 1999). These conditions are illustrated in Figure 2.6, and are described in the following section.

In Figure 2.6, assuming n_v valley folds and n_h hill folds meet at node O, the total number of folds, n_t, is defined as:

$$n_t = n_h + n_v \tag{2.1}$$

When the sheet is partially folded, the sheet behaves as that shown in Figure 2.6(b). The shape of the folded sheet is a polygon as shown in its sectional view of the line between nodes A and B in Figure 2.6(c). The sum of interior angles of the polygon is $(n_t - 2)\times 180^o$. Each of the interior angles varies during folding, and when the sheet is folded completely the angles of valley and hill folds become either 360^o or 0^o, respectively. That is:

$$(n_t - 2)\times 180^o = n_v \times 360^o \tag{2.2}$$

Consequently, substituting Equation (2.1) to Equation (2.2) gives

$$|n_h - n_v| = 2 \tag{2.3}$$

Thus,

$$n_t = 2(1 + n_v) \tag{2.4}$$

Therefore, it is found that 2 is the minimum number of the folds required to fold a sheet, whenever different folds meet at a common point there should be at least 4 folds, and the total number of the folds is always an even number.

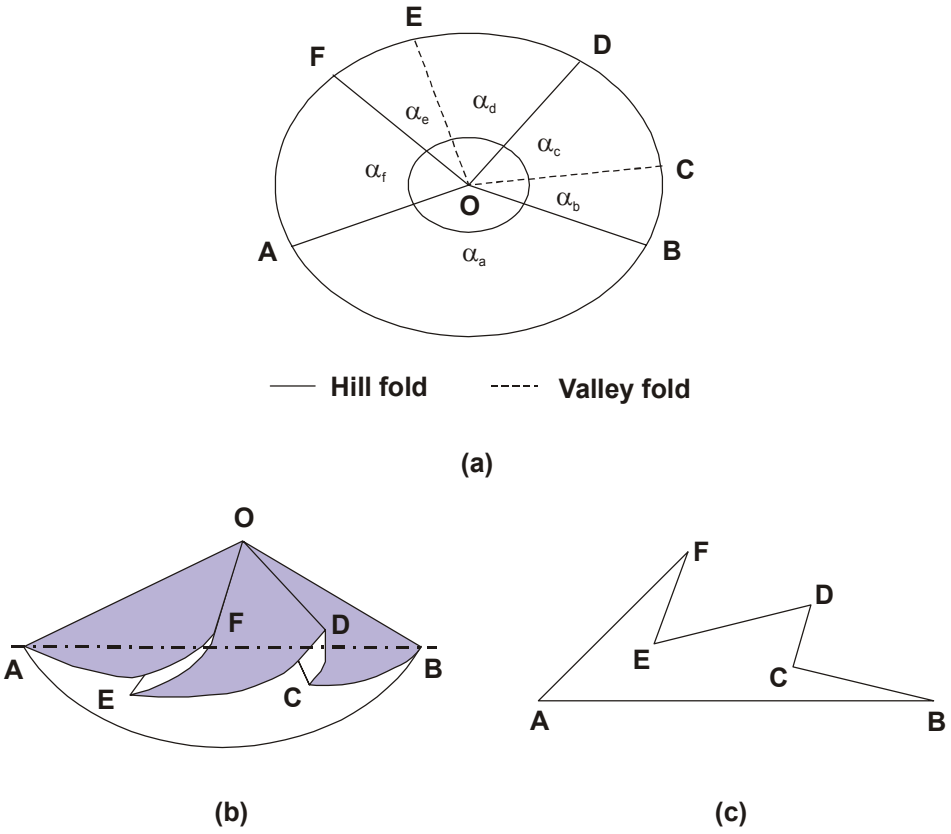

Figure 2.6 Sheet with folds when it is (a) completely open and (b) partially folded. (c) A schematic diagram of the section of folds.

For the folding pattern given in Figure 2.6(a) the sums of the alternating centre angles must be

$$\alpha_a + \alpha_c + \alpha_e = \alpha_b + \alpha_d + \alpha_f = 180^o \tag{2.5}$$

This can be proven easily by examining the completely folded configuration of the sheet. In origami, this condition is known as Fushimi's theorem.

Figure 2.7 shows an example of the foldable sheet with one node and four folds. The solid lines 1, 2 and 3 and the broken line 4 represent hill and valley folds, respectively. Due to Equation (2.5), we have:

$$180^o - \alpha + \gamma = 180^o - \beta + \beta - \gamma + \alpha \tag{2.6}$$

Consequently,

$$\alpha = \gamma \tag{2.7}$$

Similarly, in the case of the folding sheet with one node and six folds shown in Figure 2.8, there is

$$\beta - \alpha = \delta - \gamma + \theta \tag{2.8}$$

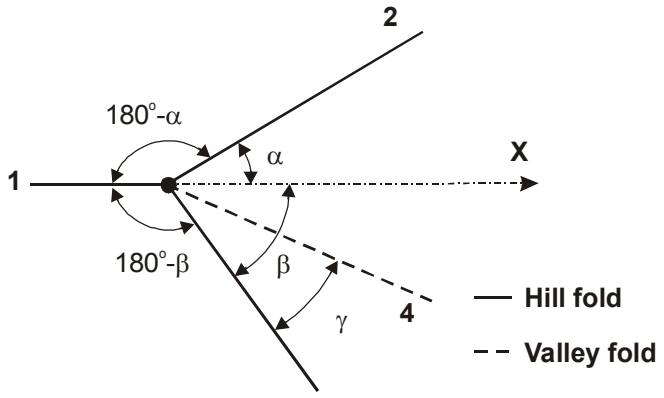

Figure 2.7 Angles among four folds meeting at one node.

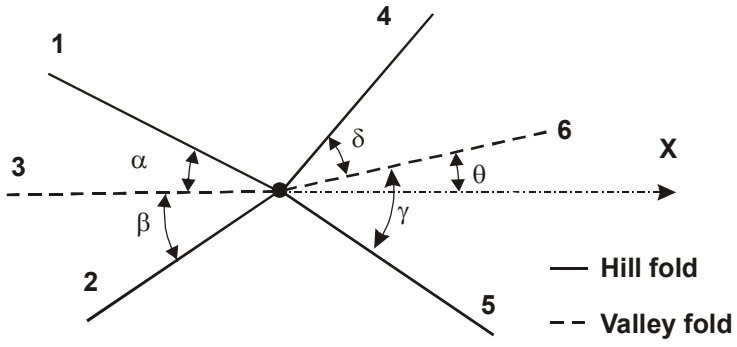

Figure 2.8 Angles among six folds meeting at one node.

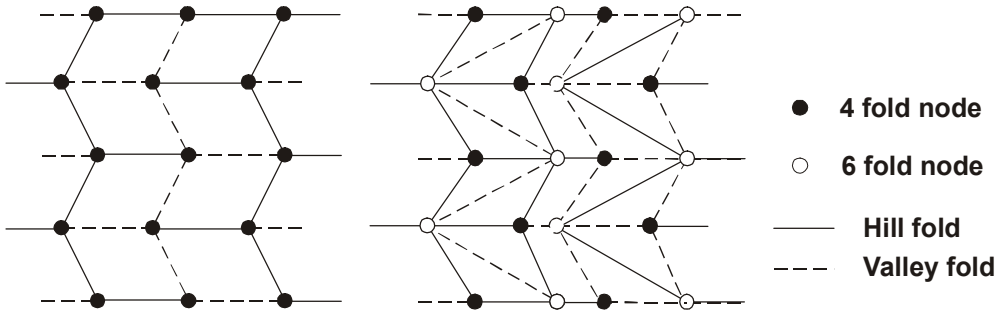

Figure 2.9 (a) The Miura-ori and (b) its more complex variation.

The fundamental relationships for folding a sheet can be applied to generate compact folding. A pattern, in Figures 2.9(a) known as the *Miura-ori*, has been applied to the design of foldable maps as well as solar antennas, which can be folded compactly and expanded easily and effectively (Miura, et al. 1980; Miura 1993). Figure 2.9(b) is a more complex variation of the *Miura-ori* with one node and four or six folds (Nojima 1999). A number of researchers have explored folding patterns for wrapping membranes in a similar manner (Guest and Pellegrino 1992; You 1994).

Using these fundamental conditions of origami, it is possible to design a foldable cylindrical tube. The angles of the folding pattern for the foldable cylinder were investigated by Nojima (1999). Figure 2.10(a) shows a strip/ribbon on which the angles between the folding line i ($i = 1, 2, 3 \cdots .$) with respect to the horizontal are defined as θ_i ($i = 1, 2, 3 \cdots .$) where $0 \le \theta \le 90^{o}$. The strip changes its direction through the folding process (Figure 2.10b). The directions of the strip with respect to the horizontal after the folding are defined as $X_1, X_2, X_3 \cdots$ The angle of the direction X_1 after the first time folding is $\Theta_1 = 2\theta_1$, and the angles of the direction X_2 or X_3 after 2 or 3 times folding become $\Theta_2 = 2(\theta_1 - \theta_2)$ and $\Theta_3 = 2(\theta_1 - \theta_2 + \theta_3)$, respectively. The direction of the strip with respect to the horizontal after i times of folding is given by,

$$\Theta_i = 2\sum_{j=1}^{i} (-1)^{j+1}\theta_j \tag{2.9}$$

where Θ_i is always an even number.

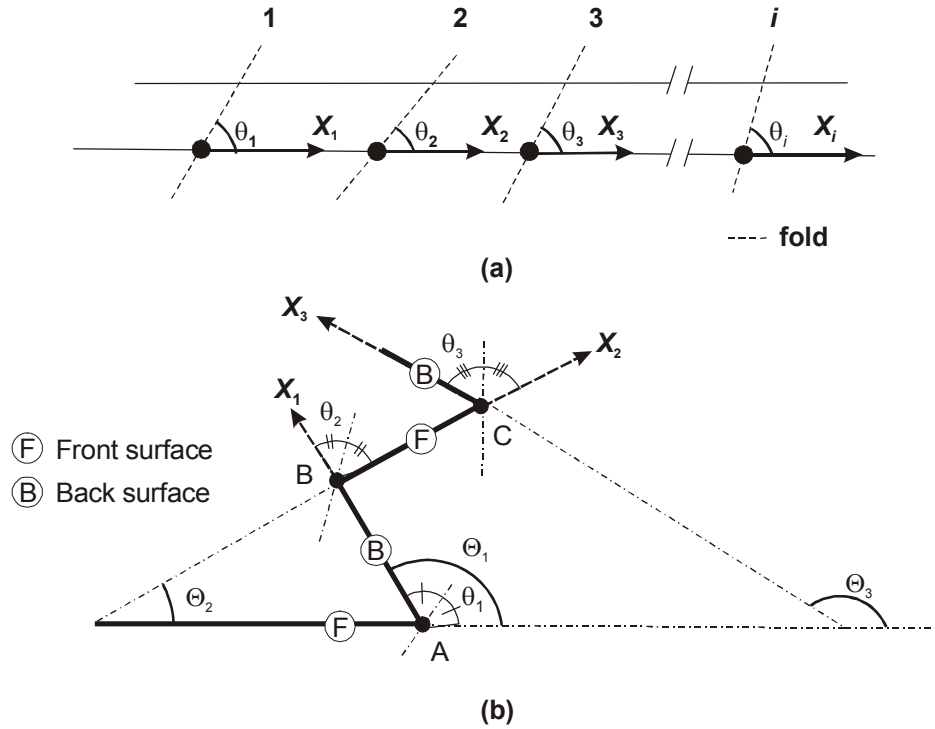

Figure 2.10 (a) Folds along a strip. (b) The change direction of the strip through the folding process.

Figure 2.11 shows an example of the deployment of a foldable cylinder when the angle α is assumed 30^{o} and $i = 6$. From Equation (2.9), in order to joint both ends without mismatch and to make a cylindrical shape the angle Θ_i has to be 360^{o} thus β is calculated as 150^{o}. The opposite edges of the sheet, A-A are jointed together to form a cylindrical tube. A number of similar foldable cylindrical tubes have been explored (Guest and Pellegrino 1994b; Sogame 1998; Nojima 1999). A photograph of one of the examples has been shown already in Figure 2.5. As mentioned, the tube can be folded in a mainly longitudinal direction. However, a foldable cylindrical tube which can be folded radially to reduce the diameter during delivery to the human body, is of interest to a stent design, and is the main focus of this dissertation.

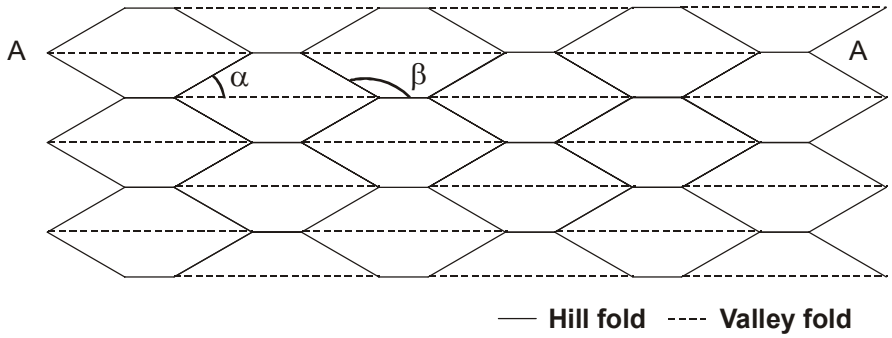

Figure 2.11 A diagram of a foldable cylindrical tube with 4 folding lines for each node in its unfolded state.

2.5 Materials

2.5.1 Stainless steel

Stainless steel has been used to make a stent as it is easy to fabricate and significantly cheaper than alternatives such as shape memory alloy. Among the hundreds of types of the stainless steels, 316L which consists of an austenitic steel, an alloy primarily of iron, chromium, and nickel with extra low carbon has better corrosion resistance compared with other types of stainless steel, and is thus ideal for medical application. It is most widely used for current stents and stent grafts.

2.5.2 Shape memory alloy (SMA)

SMA is also used in existing stents and stent grafts. SMA is a material which is able to remember shapes. This unique phenomenon was discovered in an alloy of copper and zinc in 1938 by A. B. Greninger and V. G. Mooradian. Later research revealed shape memory effects in other alloys as diverse as gold-cadmium, iron-platinum, iron-nickel and stainless steels. The phenomenon received worldwide attention in the 1960s when TiNi SMA, an alloy of titanium and nickel, was produced by W. J. Buehler (Buehler 1963).

In general, the shape memory effect (SME) of SMA can be triggered either thermally or mechanically. Figure 2.12 shows the stress-strain curve of one-way SMA, which is triggered by thermal action. The alloy is deformed with up to 8% of strain at an ambient temperature, which is more than 10 times larger than the yield strain of the conventional stainless steel as shown in Figure 2.12, and does not return to its original shape when the load is released. However, the alloy can completely recover its original shape when raised to a higher temperature.

Usually the SME involves two different crystal phases at the microstructural level; one stable phase at high temperature, the austenite phase (or the parent phase), and the other lower temperature phase, the martensite phase. The austenite phase usually has a cubic structure, represented by a square in Figure 2.13. The martensite structure is obtained by shearing deformation of the austenite. This is accomplished by the relative displacement of the atoms without breaking the bonding between them, and is called the martensitic transformation. Depending on the shear direction, martensite with two different orientations can form, referred to as variants or martensitic twins.

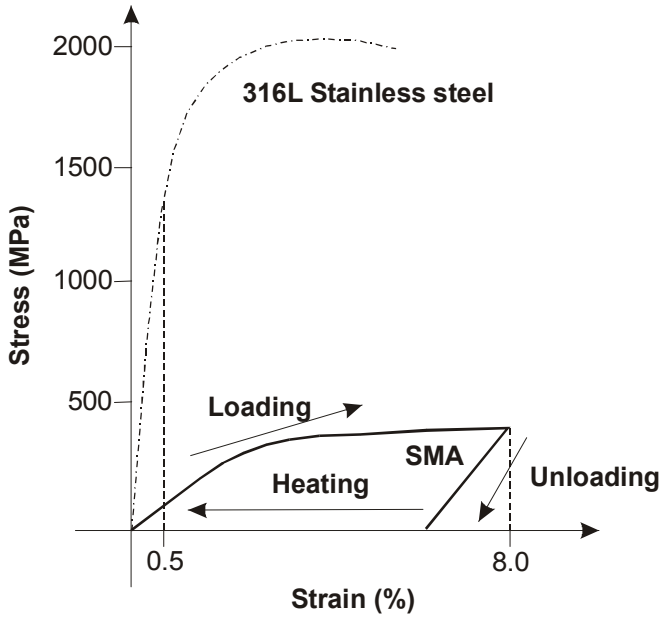

Figure 2.12 Illustration of stress-strain curves of SMA.

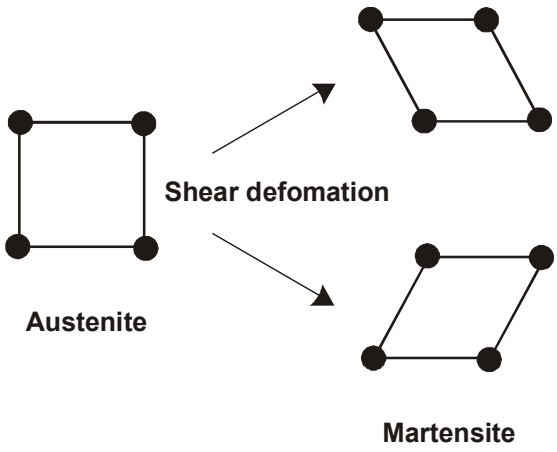

Figure 2.13 Illustrations of crystal phases of SMA.

Figure 2.14 shows the schematic diagrams of the crystal structures in the one-way SMA. It also shows the illustration of an example of a specimen with one-way SME. In this case, the specimen remembers the straight shape. When the austenite phase of the SMA is cooled to a lower temperature, a self-accommodating arrangement of the martensite variant forms (Figure 2.14a), which is composed of alternative layers of variants with opposite shear directions. The boundaries between these variants are highly mobile. Thus the material deforms easily under external forces, resulting in the specimen being bent and the martensite becomes non self-accommodating arrangement (Figure 2.14b). On reheating, the crystal structures start to change and the shape recovery begins (Figure 2.14c) and eventually become the single austenite phase (Figure 2.14d). At that time, the specimen is back to its original shape. Once the shape has recovered, there is no change in shape when the bar is cooled, though the material goes back to the self-accommodating martensite shown in Figure 2.14(a).

By repeating this one-way effect, the material can also be 'trained' to exhibit a 'two-way' memory. It remembers two configurations, for example, it may remember the straight and semi-circular shapes of the bar shown in Figures 2.14(a) and (c), and changes its shape between the two states on cooling and heating, respectively.

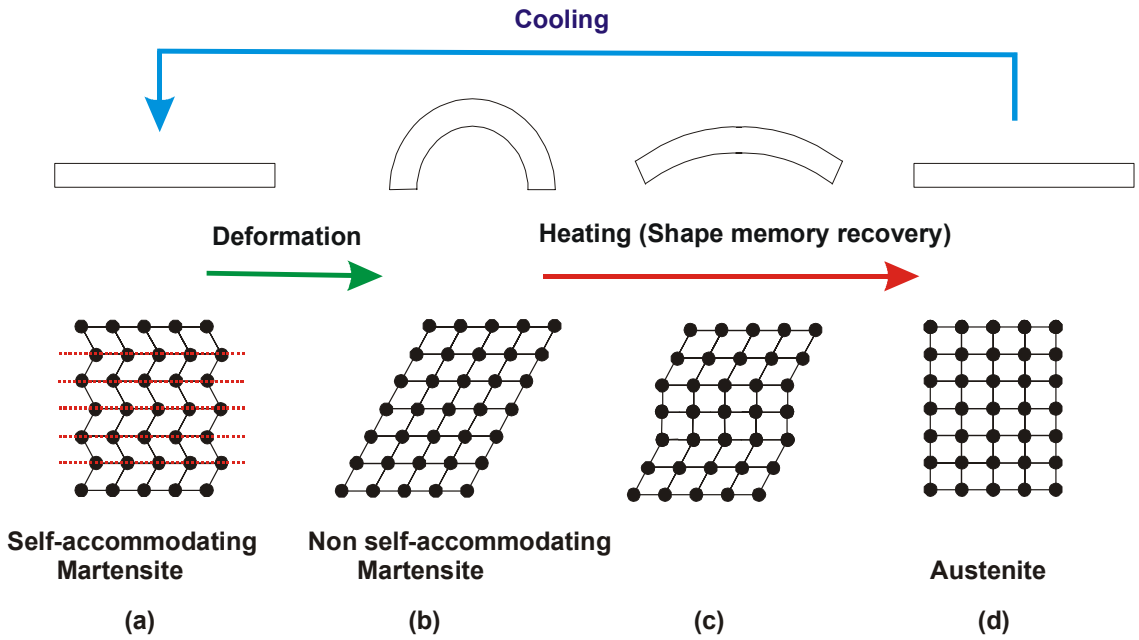

Figure 2.14 (a)-(d) Schematic diagrams of the shape memory recovery.

In the phenomenon of shape memory recovery shown in Figure 2.14, the temperatures which change the phases between martensite and austenite are called transformation temperatures. The transformation temperatures at which the phase transformation from martensite to austenite is initiated and fully completed on heating are called A_s and A_f, respectively. And the temperatures at which the phase transformation from austenite to martensite on cooling is initiated and fully completed are called M_s and M_f, respectively.

The transformation temperatures are determined by a number of factors, such as material composition, the amount of cold-work and heat treatment parameters. Among these material composition is the most important parameter (Gotman 1997; Saburi 1998). Figure 2.15 shows the relationship between A_f and alloy composition in TiNi alloy. When the Ni content is higher than 50at%, which is Ni-rich, A_f starts to decrease. A_f is very sensitive to changes in Ni content. For example, for a 0.01at% change in Ni content, there is a 150K decrease in A_f.

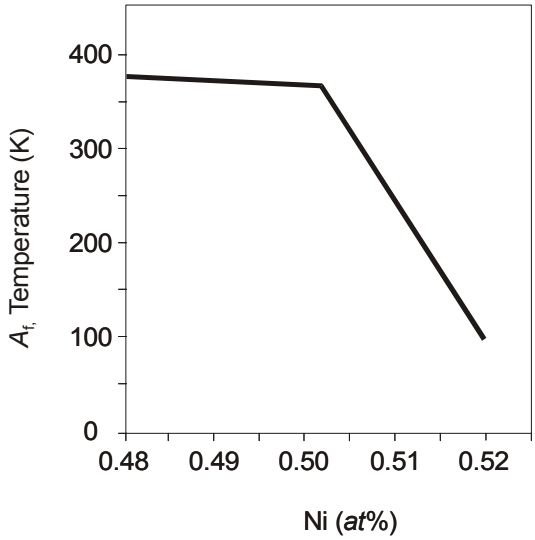

Figure 2.15 A_f vs. ratio of Ni in TiNi SMA.

It is also possible to trigger the SME of SMA mechanically due to the property of *superelasticity*. This occurs when SMA is used at a higher temperature than A_f. Figure 2.16 shows the stress-strain curve of the superelastic behavior in SMA. The deformation disappears and the alloy restores its original shape, not on the application of heat, but on a reduction of stress. As shown in Figure 2.17, during this process the austenite phase is changed to the martensite phase by the external force. Most self-expandable stents make use of superelasticity rather than temperature-induced shape alternation.

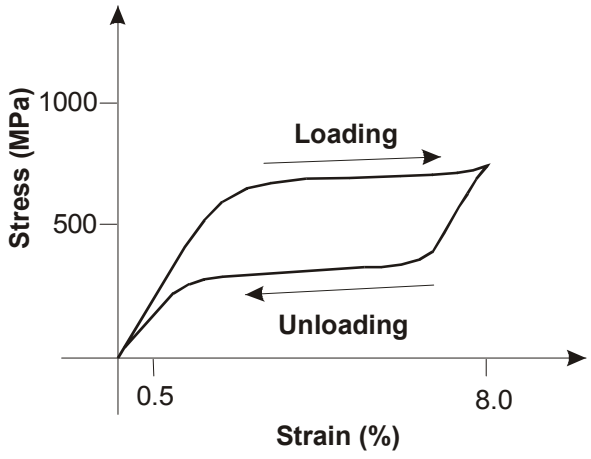

Figure 2.16 Illustrations of stress-strain curves of a superelastic behavior in SMA.

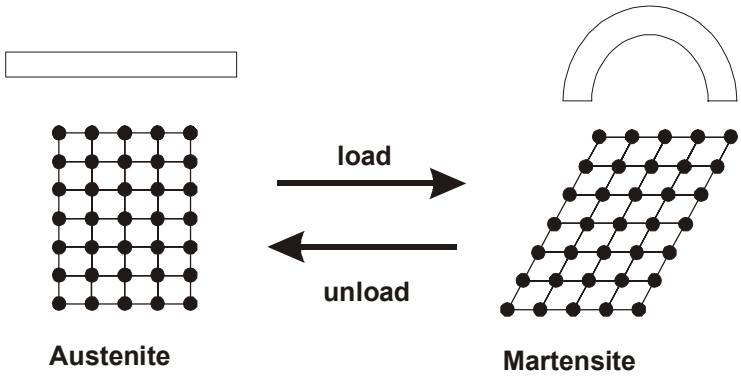

Figure 2.17 Schematic diagram of superelasticity.

At present, SMA materials are produced in wire, tubular and sheet forms. Many applications make use of the SMA wire and tubular configurations. In aerospace and aviation industries, for instance, tube and pipe connectors for pneumatic and hydraulic lines and flexible satellite antennas have been manufactured (Schetky 1979). SMA wire has been applied in medical industry for a broad range of devices used in orthopedics, neurology, cardiology and interventional radiology (Lipscomb and Nokes 1996). Self-expanding stents and stent grafts are among the most successful medical TiNi SMA applications (Domschke, et al. 1990; Cowling, et al. 1998b; Marks, et al. 1999; Cowling 2000).

Compared to the wire forms, usage of SMA sheets is very limited. The only notable use of the SMA sheets is for a small structure in Micro Electro Mechanical Systems (MEMS), such as those found in the microactuators of micropumps and those used as microelectrodes for neural recording (Obermeier and Thielicke; Kuribayashi 1989; Kahn, et al. 1998; Makino, et al. 2000; Takeuchi and Shimoyama 2000). Complex rolling and annealing methods are required to produce a large and thin sheet due to the low plastic workability and high work hardening rate of SMA. Therefore commercially available SMA sheets are still very expensive, resulting in the rarity of SMA sheets in industrial products. A new method has recently been developed to

produce the sheet using ultrafine laminates of pure Ti and Ni (Tomus, et al. 2003), which can reduce the cost. This improvement to the production of SMA sheets is expected to lead to a significant expansion in the number of applications of SMA.

In most applications involving SMA sheets, the material needs to be cut with sophisticated precision methods. The SMA sheet can be cut using either photochemical etching, which uses an etchant mixture of hydrofluoric acid (HF), nitric acid (HNO_3) and water, or using electrochemical etching, which uses an etchant of sulfuric acid (H_2SO_4) and anhydrous methanol (Makino, et al. 1998; Chen and Wu 1999; Mineta, et al. 2001). Other processing methods including laser cutting and electro-discharge machining (Kohl, et al. 1994) are thermal processes, which may influence the characteristics of the SME (Reynaerts, et al. 1996; Haferkamp, et al. 2001). Etching is less expensive and offers a finer control over the etching depth so that precise and complex designs may be produced. Moreover, as shown in Figure 2.18, the surface of an etched sample is smoother than the one cut by laser (Skrobanek, et al. 1998).

(a) **(b)**

Figure 2.18 Surface of TiNi after (a) laser cutting and (b) electrochemical etching (source: Kohl 1994).

2.5.3 SMA for stents and stent grafts

The distinct characteristics of the SMA enable it to be used for medical devices. The ability of SMA to recover a designed shape allows the production of stents and stent grafts which are self-expanding at body temperature. The transformation temperature A_f can be adjusted to be less than the body temperature allowing it to be used for self-expanding stents and stent grafts. This eliminates the necessity for extra deployment devices, e.g., balloons, for an expansion.

As illustrated by the black line in Figure 2.19, a stent is compressed into the delivery system following the loading curve from point O to A. After the sheath is withdrawn, the stent starts to expand and is back to its original shape following the unloading path of the stress-strain curve from point A to B shown by the red dash line. At point B the stent reaches the diameter of the vessel lumen and is against the vessel

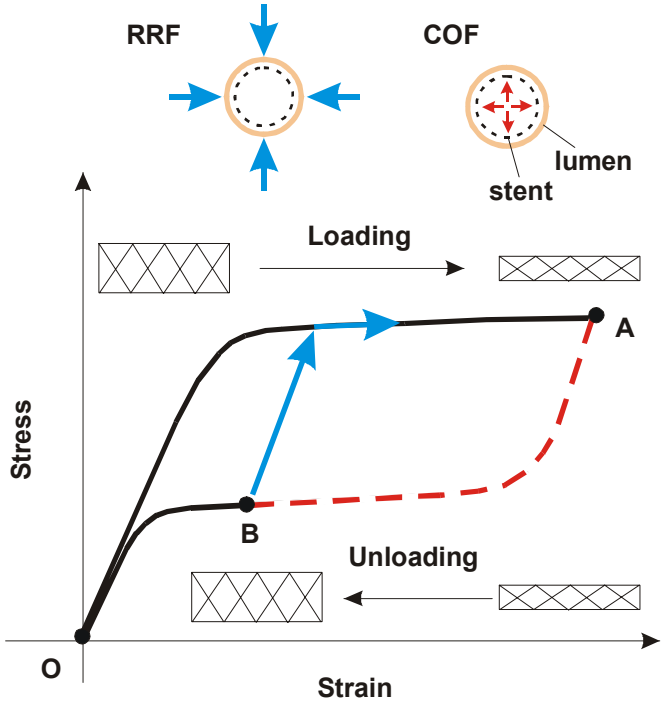

Figure 2.19 Illustration of high resistant deformation force

wall with small outward force (COF, chronic outward force). If the vessel contracts through spasms or is compressed from the outside, the stent resists deformation with a larger force (RRF, radial resistive force) which is indicated by the blue arrow. Therefore, SMA stents can withstand external pressure. (Friend and Morgan 1999; Stoeckel 2000).

Biocompatibility is the ability of material to be accepted by the body. It is related to the corrosion behavior of the material. TiNi SMA forms a passive titanium oxide layer that acts as a physical barrier to nickel oxidation and also offers chemical protection against corrosion (Moorleghem, et al. 1998; Ryhanen 1999). Tests show that there is no significant increase in the level of nickel in blood after the implant of a TiNi SMA. Such an increase would be expected if the SMA were not biocompatible (Duerig, et al. 1999). TiNi SMA also shows no cytotoxic (cell-damaging) effects.

Ferromagnetic materials that are often used in surgery typically have large magnetic susceptibilities, causing field distortion and Magnetic Resonance Imaging (MRI) artifacts around implanted metal objects. TiNi SMA is non-ferromagnetic with a lower magnetic susceptibility than some materials, such as stainless steel (Duerig, et al. 1999). Therefore, the TiNi SMA stent can be detected by MRI during an operation without the problem of artifacts (Holton, et al. 2002), which greatly aids doctors to insert and position the stents.

CHAPTER 3

FOLDABLE CYLINDRICAL TUBE AS NEW STENT GRAFT

A stent graft is a tubular foldable structure as discussed in Chapter 1. In this chapter, a new type of an innovative stent graft is developed based on novel folding patterns of the cylindrical tube. The chapter deals mainly with the geometric aspects of the stent graft.

A new design of the foldable cylindrical tube is considered in Sections 3.1 in which the tube is divided into a number of foldable elements. Section 3.2 gives the geometric properties of a basic element such as radius. Condition regarding the connection of the basic elements in a longitudinal direction is considered in Section 3.3. In the following sections, Sections 3.4 and 3.5, other geometric properties of the foldable cylindrical tube such as length and deformation are defined and analysed. Section 3.6 generalises the basic element and its geometric properties are also defined. In Section 3.7, the results of the geometric properties of the new stent graft are discussed. This is followed by a discussion of variations of the folding patterns in Section 3.8 for both cylindrical and conical tubes. Section 3.9 concludes this chapter.

It is important to note that the analysis presented in this chapter is purely geometric in which material deformation during deployment and the thickness of the models are not considered.

3.1 Foldable cylindrical tube as a stent graft

The crucial requirement in the design of a cylindrical tubular stent graft is that it can be folded in its radial direction, and when folded its radius is minimised so that it can be delivered to the human body with ease. To achieve compact packaging of the tubular stent graft, carefully designed folds are introduced. These folds will behave as line hinges so that more complex joints or sliding wires are not required. The stent graft must also have a simple structural form. The pattern of the folds used in the stent graft is inspired by the *pineapple folding pattern* using triangular units (Kresling 1995).

Figure 3.1 shows photographs of the foldable cylindrical tube model with a pineapple folding pattern made of a single sheet of paper in its fully folded and deployed configurations, respectively. It becomes a cylindrical tube in the fully expanded configuration.

The details of the folding pattern are given in Figure 3.2. The solid and broken lines represent hill and valley folds which form peak and trough creases, respectively. As shown in Figure 3.2(a), the element has a square shape and its folding pattern is symmetrical both vertically and horizontally. As shown in Figure 3.2(b), the pattern of the folds comprises the square elements which are repeated over the entire area of the sheet. The total numbers of the elements in horizontal and vertical directions are denoted as m and n, respectively. The elements on even rows are shifted half an element in comparison with those on odd rows illustrated in bold outline in the figure. The opposite edges of the sheet, a_1-a_2-a_3 and b_1-b_2-b_3 are joined together to form a cylindrical tube. It is also noted from Figure 3.2(b) that there are six folds intersecting at those points marked by black dots. They satisfy Equations (2.4) and (2.5) which are the fundamental relations of the number of the hill and valley folds and of the angles for folding a sheet as described in Chapter 2.

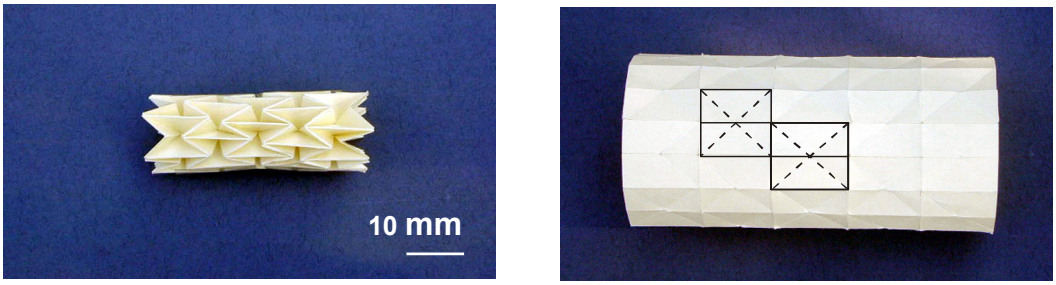

Figure 3.1 Photographs of the foldable cylindrical tube with a pineapple folding pattern in its (a) fully folded and (b) fully deployed configurations.

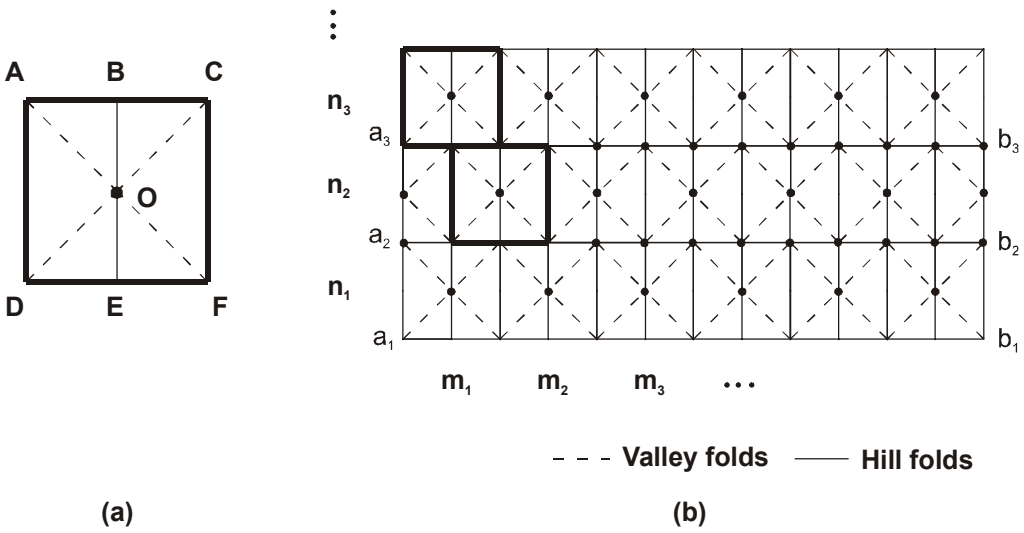

Figure 3.2 (a) A basic element and (b) development of the basic pattern.

One of the most interesting properties of the folding pattern is that it causes the cylinder to fold and expand both longitudinally and radially. Hence, both the length and the diameter of the tube decrease during folding and increase during expanding. The folded configuration of each element also makes the tube flexible. These properties are suitable for the stent graft design because it can be packaged compactly and it has a

certain amount of flexibility when folded. Furthermore, the folds rather than a more complex hinging mechanism allow the stent graft to fold neatly and expand simply without causing any such problems as tangling and rupturing.

3.2 Generalised rectangular element

3.2.1 The element

The pineapple folding pattern is, in fact, a special case of a family of more general folding patterns. Consider a more general rectangular basic element shown in Figure 3.3(a). The angles $\angle DAO$ and $\angle OAB$ can be denoted as α_1 and α_2, respectively, and $\alpha_1 + \alpha_2 = 90^o$. Let l represent the length AB ($AB = AC/2$). Obviously, a row of such elements can be mapped onto a sheet, see Figure 3.3(b). By joining a_1-a_2 with b_1-b_2, a tube is formed.

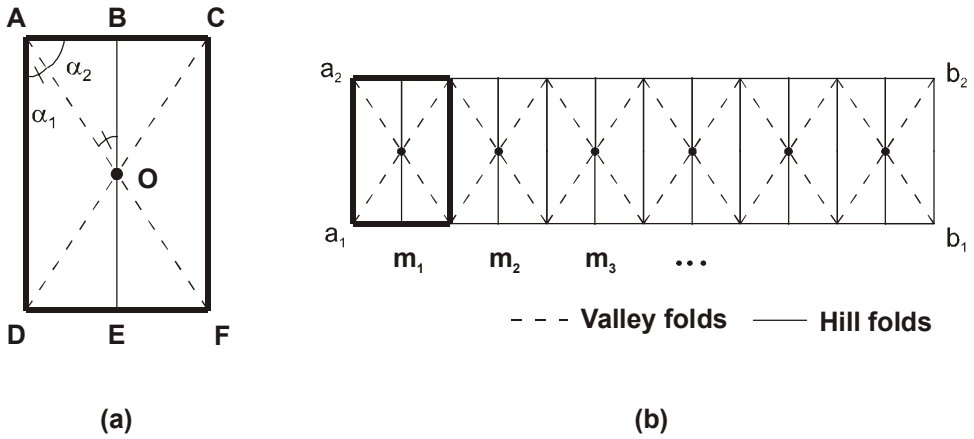

Figure 3.3 (a) Generalised rectangular element and (b) formation of a tube with such elements.

3.2.2 Central and deployment angles

Figure 3.4 shows a perspective view of the foldable cylindrical tube formed by a single row of the rectangular elements. The *central angle*, δ, is defined as $\angle AO_0C/2$, which depends on the number of the circumferential elements, *m*, and can be calculated as

$$\delta = \frac{360^o}{2m} = \frac{180^o}{m} \tag{3.1}$$

δ must remain constant during deployment.

Now consider a single element of the tube during deployment, shown by the perspective view in Figures 3.5(a)-(c). It is assumed that the rest of the elements behave exactly the same. It should be pointed out that the deployment of the tube goes through two phases. During the first phase, the element deploys until nodes A, B and C become co-liner, i.e., the rectangular element is flattened. The *deployment angle*, θ, is defined as $\angle ABC/2$. When the tube is fully folded, node O will reach the projection position of O_0, and θ becomes the fully folded deployment angle, θ_0. From Figure 3.5(a),

$$AQ = AB\sin\theta_0 = l\sin\theta_0 \tag{3.2}$$

and from Figure 3.5(d),

$$AQ = O_0A\sin\delta \tag{3.3}$$

When O and the projection of O_0 overlap, $O_0A = OA\sin\alpha_1 = l$,

$$\theta_0 = \delta \tag{3.4}$$

During the first phase θ alters from θ_0 to 90^o.

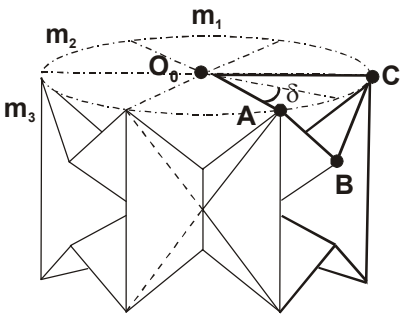

Figure 3.4 Perspective view of a tube formed by a row of the rectangular elements.

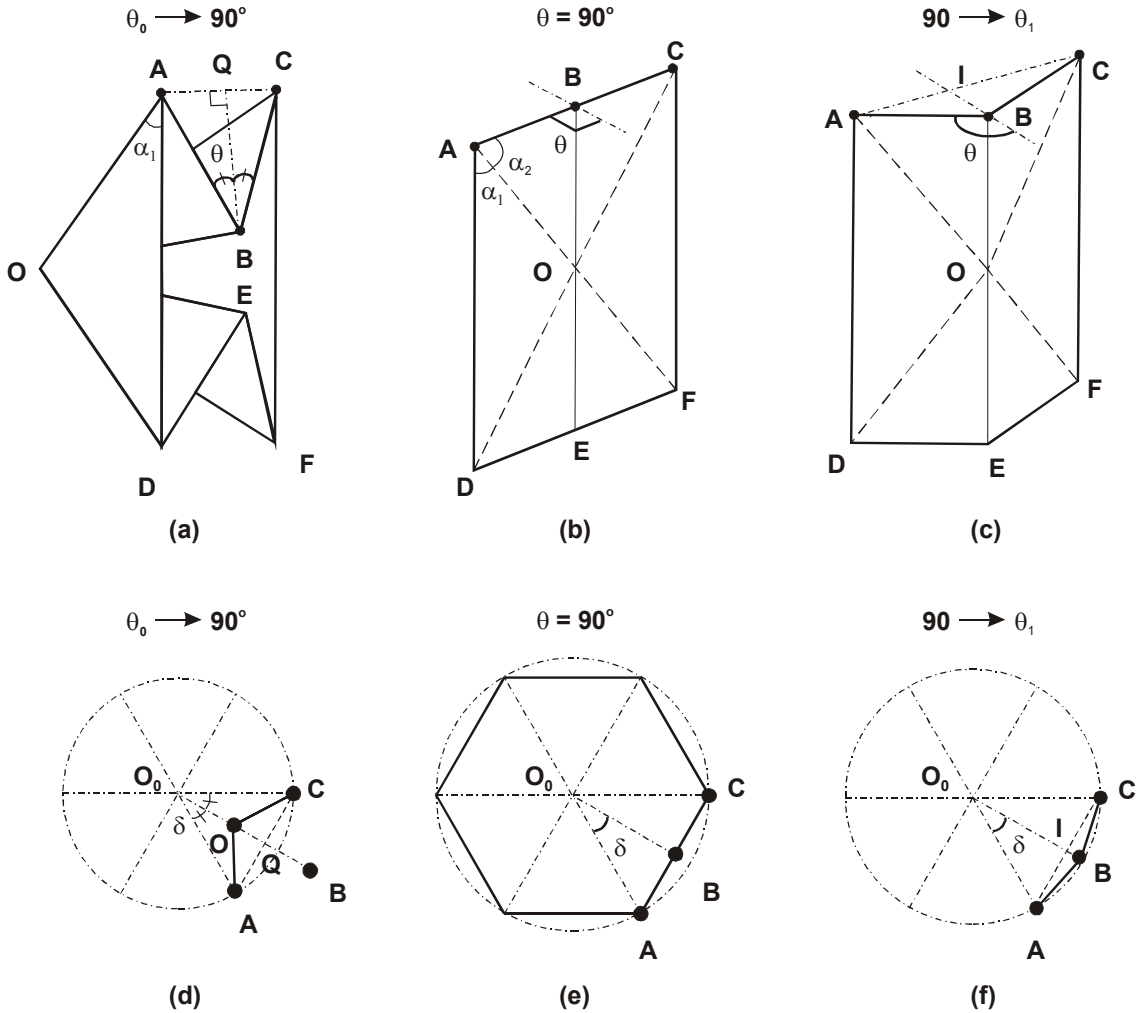

Figure 3.5 (a), (b) and(c) Perspective and (d), (e) and (f) projective views of a single element during deployment.

Then, on the second phase of deployment the central crease between nodes B and E moves outwards in the radial direction. In order to make θ larger than 90^o and continually increase as the tube deploys, the *deployment angle*, θ, is redefined as an outside angle (angle more than 90^o and less than 180^o) as shown in Figure 3.5(c). θ reaches θ_1, the fully expanded deployment angle, when the tube is fully deployed. For this instance,

$$\theta_1 = 180^o - \angle ABO_0 \tag{3.5}$$

where

$$\angle ABO_0 = \frac{180^o - \delta}{2} \tag{3.6}$$

Thus

$$\theta_1 = 90^o + \frac{\delta}{2} \tag{3.7}$$

Table 3.1 shows how the deployable angles, θ_0 and θ_1, in its fully folded and expanded forms, vary with the different values of the number of elements, *m*. As *m* increases, both θ_0 and θ_1 decrease.

Table 3.1 Deployment angles vs. *m*

m	4	6	8	9	12	18
θ_0 (deg.)	45	30	22.5	20	15	10
θ_1 (deg.)	112.5	105	101.25	100	97.5	95

3.2.3 Radius during deployment

The radius of the stent graft is one of the most important geometric properties measured during the deployment process of the cylindrical tube. It is possible to calculate the change in radius during deployment of the foldable cylindrical tube using a single row of the rectangle elements.

Based on the projection of the tube, see Figure 3.5(a), denote

$$R_{o1} = O_0 B \tag{3.8}$$

$$R_{o2} = O_0 A \tag{3.9}$$

and

$$R_i = O_0 O \tag{3.10}$$

where O_0 is a node at a central axis in a longitudinal direction.

During the first phase of deployment, i.e., $\theta_0 \le \theta \le 90^o$, a typical element is shown in Figure 3.6. Combining it with Figure 3.5(d) gives

$$R_{o1} = O_0 B = \frac{AC/2}{\tan\delta} + O'B \tag{3.11}$$

$$R_{o2} = O_0 A = \frac{AC/2}{\sin\delta} \tag{3.12}$$

$$R_i = O_0 O = \frac{AC/2}{\tan\delta} - OO'_p \tag{3.13}$$

where

$$AC = 2l\sin\theta \tag{3.14}$$

Substituting Equation (3.14) into (3.12) gives

$$R_{o2} = \frac{l\sin\theta}{\sin\delta} \tag{3.15}$$

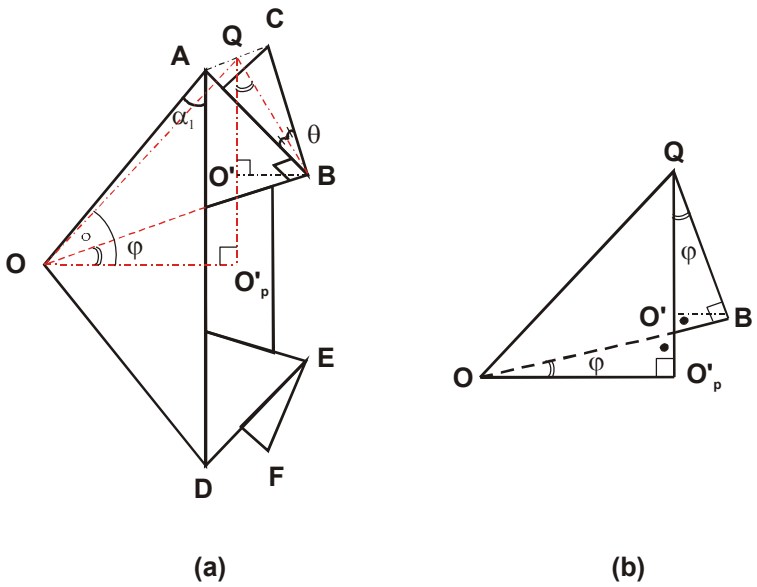

Figure 3.6 Rectangular element during the first phase of deployment. (a) Perspective view and (b) side projection of the top half of the element.

It is noted that in Figure 3.6(a) node B sticks out off the plane formed by nodes A, C, F and D by length *O'B*. Because *OB* is perpendicular to both *AB* and *BC*, *OB* is also perpendicular to *BQ*. From Figure 3.6(b), *O'B* is given by

$$O'B = BQ\sin\varphi = l\cos\theta\sin\varphi \tag{3.16}$$

where

$$\varphi = \angle BQO' = \angle O'OO'_{\mathrm{p}} = \angle QOO'_{\mathrm{p}} - \angle QOB \tag{3.17}$$

Back to Figure 3.6(a) again,

$$\angle QOO'_{\mathrm{p}} = \arcsin\left(\frac{QO'_{\mathrm{p}}}{OQ}\right) = \arcsin\left(\frac{AD}{2OQ}\right) \tag{3.18}$$

and

$$\angle QOB = \arccos\left(\frac{OB}{OQ}\right) \tag{3.19}$$

while

$$AD = \frac{2l}{\tan\alpha_1},\ OB = \frac{AD}{2} = \frac{l}{\tan\alpha_1} \tag{3.20}$$

and

$$OQ = \sqrt{OA^2 - AQ^2} \tag{3.21}$$

where

$$OA = \frac{l}{\sin\alpha_1},\ AQ = l\sin\theta \tag{3.22}$$

Substituting Equations (3.20) to (3.22) into (3.18) and (3.19) and then into (3.17) gives

$$\varphi = \arcsin\left(\frac{AD}{2OQ}\right) - \arccos\left(\frac{OB}{OQ}\right)$$

$$= \arcsin\left(\frac{\cos\alpha_1}{\sqrt{1-\sin^2\theta\sin^2\alpha_1}}\right) - \arccos\left(\frac{\cos\alpha_1}{\sqrt{1-\sin^2\theta\sin^2\alpha_1}}\right) \tag{3.23}$$

Hence, from Equation (3.16)

$$O'B = l\cos\theta\sin\left[\arcsin\left(\frac{\cos\alpha_1}{\sqrt{1-\sin^2\theta\sin^2\alpha_1}}\right) - \arccos\left(\frac{\cos\alpha_1}{\sqrt{1-\sin^2\theta\sin^2\alpha_1}}\right)\right]$$

$$= l\cos\theta\frac{\cos^2\alpha_1 - \sin^2\alpha_1\cos^2\theta}{1-\sin^2\theta\sin^2\alpha_1} \tag{3.24}$$

Thus, using Equation (3.11)

$$R_{o1}=\frac{l\sin\theta}{\tan\delta}+l\cos\theta\frac{\cos^2\alpha_1-\sin^2\alpha_1\cos^2\theta}{1-\sin^2\theta\sin^2\alpha_1} \tag{3.25}$$

For the basic rectangle element, as shown in Figure 3.6, $OB=QO'_p$. $\Delta OQO'_p$ and ΔOQB are therefore equal triangles, so,

$$OO'_p=QB=l\cos\theta \tag{3.26}$$

Substituting Equation (3.26) into (3.13) gives

$$R_i=\frac{l\sin\theta}{\tan\delta}-l\cos\theta \tag{3.27}$$

On the second phase of deployment, i.e., θ varies from 90^o to θ_1, see Figures 3.5(c) and (f). With regards to the radii, it is found that

$$R_{o1}=\frac{AC/2}{\tan\delta}+IB=\frac{l\sin\theta}{\tan\delta}-l\cos\theta \tag{3.28}$$

$$R_{o2}=\frac{AC/2}{\sin\delta}=\frac{l\sin\theta}{\sin\delta} \tag{3.29}$$

$$R_i=R_{o1}=\frac{l\sin\theta}{\tan\delta}-l\cos\theta \tag{3.30}$$

in which

$$IB=-l\cos\theta \tag{3.31}$$

Then, when the tube is fully deployed, i.e., $\theta = \theta_1$,

$$R_i = R_{o1} = R_{o2} = \frac{l}{2\sin\frac{\delta}{2}} \tag{3.32}$$

Results of the radii with various α_1 and m during deployment will be given in Section 3.7.

3.3 Connection of the elements in a longitudinal direction

In the previous section only a single row of the elements has been considered. However, elements are also connected in a longitudinal direction to form a long foldable cylindrical tube as shown in Figure 3.2(b) where a row of the elements are shifted by a half element with respect to the neighbouring rows. Let us draw attention to the rectangle elements which are located on two adjacent rows and they are to be connected together, see Figure 3.7. Now we will try to identify the condition in order to design the foldable cylindrical tube with the rectangle elements. The key values of the element angle α_1 and element number m will be discussed.

In Figure 3.7, before the top element is connected to the lower element the radii of nodes E_2 and F_2 are R_{o1} and R_{o2}, respectively, which have been defined in the previous section. For the lower element, assuming that it behaves exactly the same as the upper element during deployment, the radii of nodes A_1 and B_1 are R_{o2} and R_{o1}, respectively, before it is connected to the element above. To enable these two rows of the elements to be connected with full geometric compatibility, the radii of nodes E_2 and A_1, and nodes F_2 and B_1 must be equal throughout the deployment, i.e.,

$$R_{o1} = R_{o2} \tag{3.33}$$

or

$$\frac{l\sin\theta}{\tan\delta}+l\cos\theta\frac{\cos^2\alpha_1-\sin^2\alpha_1\cos^2\theta}{1-\sin^2\theta\sin^2\alpha_1}=\frac{l\sin\theta}{\sin\delta} \tag{3.34}$$

on the first phase of deployment from Equations (3.25) and (3.15), and,

$$\frac{l\sin\theta}{\tan\delta}-l\cos\theta=\frac{l\sin\theta}{\sin\delta} \tag{3.35}$$

on the second phase of deployment from Equations (3.28) and (3.29).

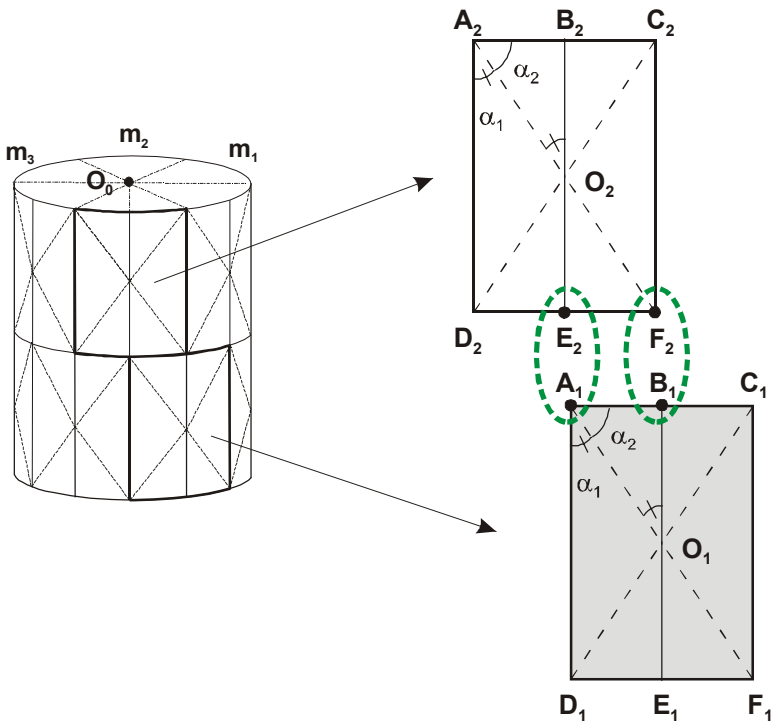

Figure 3.7 Connection of two adjacent elements.

However, it has been found that Equations (3.34) and (3.35) hold only for certain deployable angles θ's . For instance, when $m = 6$, Equation (3.1) gives $\delta = 180^{\circ} / 6 = 30^{\circ}$ and if $\alpha_1 = 45^{\circ}$, Equation (3.34) holds if $\theta = 33^{\circ}$ and $\theta = 72^{\circ}$, and Equation (3.35) holds for $\theta = 105^{\circ}$ where the tube is fully deployed at the end of phase two. Hence mismatch between R_{o1} and R_{o2} is occurring during deployment so that the tube deforms during deployment. The value of the difference between R_{o1} and R_{o2}, normalised by the length of nodes A and B, l, is denoted as y, which is

$$y = \frac{R_{o1} - R_{o2}}{l} \tag{3.36}$$

The optimum design which can be minimised the deformation of the tube is that where y is close to zero.

For m = 6, Figure 3.8 shows curves of y against θ for various α_1 and α_2 where $\alpha_1 + \alpha_2 = 90^{\circ}$. When $\alpha_1 = 45^{\circ}$, the value of y becomes zero when $\theta = 33^{\circ}, 72^{\circ}$ and 105° as indicated earlier. Also, when $\alpha_1 = 30^{\circ}$, the value of y becomes zero when $\theta = 74^{\circ}$ and 105°. When $\alpha_1 = 60^{\circ}$, the value of y becomes zero only when $\theta = 105^{\circ}$, i.e., the tube is fully folded. It is obvious that the value of y is closer to zero for every θ when $\alpha_1 = 45^{\circ}$ than when $\alpha_1 = 30^{\circ}$ or 60°. Therefore, the optimal angle α_1 could be approximately 45°. In the following, we will try to define and calculate a precise value of the optimal value of α_1.

A value M of $|y|$ during deployment is considered, which is given by

$$M = \int_{\theta_0}^{\theta_1} |y| \, \mathrm{d}\theta \tag{3.37}$$

where $\int_{\theta_0}^{\theta_1} |y| \, \mathrm{d}\theta$ is the area bounded by the curve y and the axis of $y = 0$ in Figure 3.8, and the ordinates at θ_0 and θ_1 which are deployment angles when the tube is fully

folded and expanded. M becomes minimal with respect to α_1 under the following condition

$$\frac{\mathrm{d}M}{\mathrm{d}\alpha_1} = 0 \tag{3.38}$$

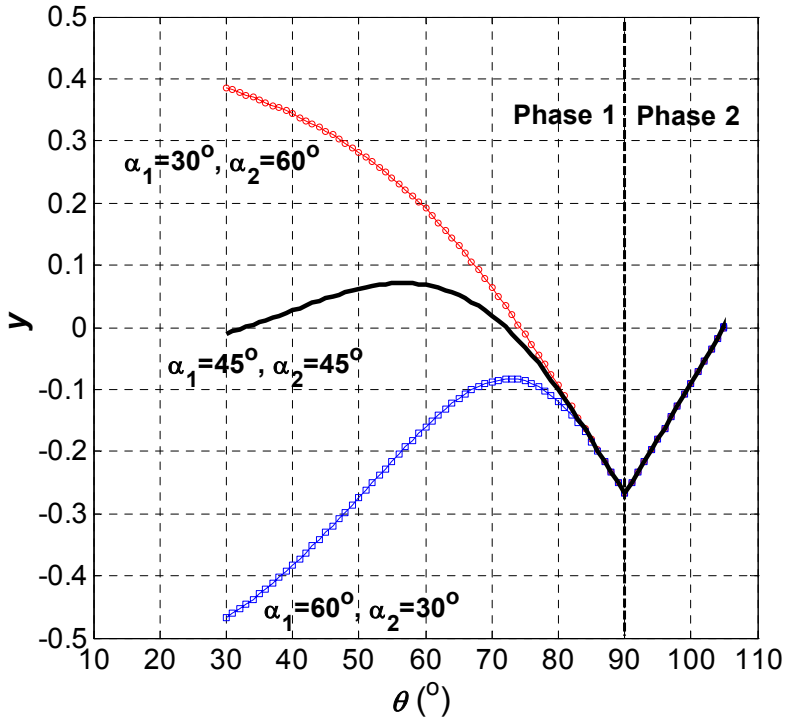

Figure 3.8 y vs. θ for the rectangle elements with various α_1 when m = 6.

From Equation (3.38), it is found that for m = 6 M becomes minimum when $\alpha_1 = 46.7^{\circ}$. The value of y with respect to θ for the rectangle elements when $\alpha_1 = 45^{\circ}$ and 46.7° is shown in Figure 3.9. The optimum design is $\alpha_1 = 46.7^{\circ}$ and $\alpha_2 = 43.3^{\circ}$. We will consider the case where the element is not rectangular in shape later in Section 3.6. As shown in the figure, the value of $|y|$ becomes maximum when $\theta = 90^{\circ}$. We need to pay more attention to the fact that when $\theta = 90^{\circ}$, the value of $|y|$ becomes very large in all cases. This large mismatch will cause problems for deployment, which will be discussed in detail in Section 3.7.

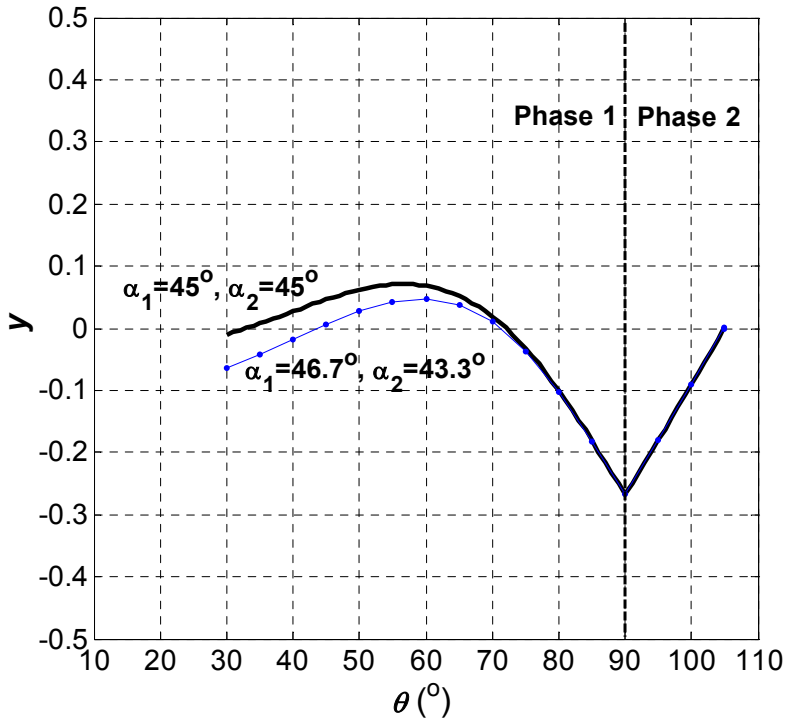

Figure 3.9 y vs. θ for the rectangle elements with α_1 = 45° and 46.7° when m = 6.

3.4 Length during deployment

As mentioned in Section 3.1, the length of the foldable cylindrical tube increases during expansion and decreases during folding. Once the elements are connected longitudinally, the other important geometric property of the stent graft, the total length of the foldable cylindrical tube, is calculated.

The total length L of the tube with the rectangle elements is defined in Figure 3.10. It is assumed that all elements behave exactly the same during deployment and the mismatch between each rows is not taken into account. During the first phase of deployment, i.e., $\theta_0 \le \theta \le 90^{\circ}$, L is given by

$$L = n \times AD - (n-1) \times O'Q \tag{3.39}$$

where AD has been calculated in Equation (3.20) and

$$O'Q = BQ \cos\varphi \tag{3.40}$$

in which φ has been calculated in Equation (3.23) and

$$BQ = l \cos\theta \tag{3.41}$$

Substitution of Equation (3.41) into Equation (3.40) gives

$$O'Q = \frac{l \sin 2\alpha_1 \cos^2\theta}{1 - \sin^2\alpha_1 \sin^2\theta} \tag{3.42}$$

Hence

$$L = n\frac{2l}{\tan\alpha_1} - (n-1)\frac{l \sin 2\alpha_1 \cos^2\theta}{1 - \sin^2\alpha_1 \sin^2\theta} \tag{3.43}$$

On the second phase of deployment, i.e., θ varies from 90^o to θ_1, L is given by

$$L = n\frac{2l}{\tan\alpha_1} \tag{3.44}$$

Results of the length calculations with various α_1, m and n during deployment will be given in Section 3.7.

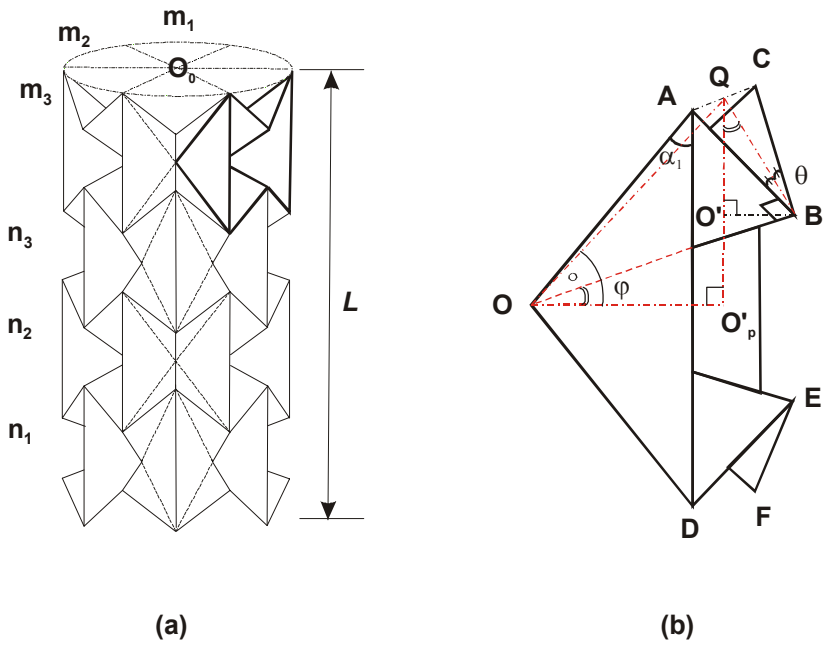

Figure 3.10 (a) Perspective view of the foldable cylindrical tube with rectangle elements and (b) one element during deployment.

3.5 Deformation during deployment

In Section 3.3 it has been found that the foldable cylindrical tube deforms during deployment because of the mismatch between the tube elements connected in the longitudinal direction. In this section the geometric parameter of the shortening of the fold during deployment is calculated to understand the deployment process. The results are useful in the determination the optimum design for the stent graft.

In Section 3.4 (Figure 3.7), it has been explained that in the top element, before it is connected to the lower element, the radii of nodes E_2 and F_2 are R_{o1} and R_{o2}, respectively. For the lower element, assuming that it behaves exactly the same as the top element during deployment, the radii of nodes A_1 and B_1 before it is connected to the element above are R_{o2} and R_{o1}, respectively. After connecting these two elements, the mismatch occurs. Assume that the radii R_{E2A1} and R_{F2B1} of the nodes E_2 or $A_1$and F_2 or B_1 are $(R_{o1} + R_{o2})/2$. In the cylindrical coordinate system, the coordinates of nodes E_2 or A_1 are ($R_{E2A1}, \delta_{E2A1}, Z_{E2A1}$) and those of nodes F_2 or B_1 are ($R_{F2B1}, \delta_{F2B1}, Z_{F2B1}$) where $\delta_{E2A1} = 0$; $\delta_{F2B1} = 180^o / m$, in which m is the number of the elements in the circumferential direction. If we denote the length between the nodes E_2 or $A_1$and F_2 or B_1 as l_a, we have

$$l_a = \left[\left(R_{E2A1} \cos\delta_{E2A1} - R_{F2B1} \cos\delta_{F2B1} \right)^2 + \left(R_{E2A1} \sin\delta_{E2A1} - R_{F2B1} \sin\delta_{F2B1} \right)^2 + \left(Z_{E2A1} - Z_{F2B1} \right)^2 \right]^{\frac{1}{2}}$$

$$= \left[\left(\frac{R_{o1} + R_{o2}}{2} - \frac{R_{o1} + R_{o2}}{2} \cos\left(\frac{180^o}{m} \right) \right)^2 + \left(\frac{R_{o1} + R_{o2}}{2} \sin\left(\frac{180^o}{m} \right) \right)^2 + \left(Z_{E2A1} - Z_{F2B1} \right)^2 \right]^{\frac{1}{2}} \quad (3.45)$$

R_{o1} has been calculated in Equations (3.25) and (3.28), and R_{o2} has been calculated in Equations (3.15) and (3.29). It is assumed that the difference between Z_{E2A1} and Z_{F2B1} is equal to the length $O'Q$. $O'Q$ was initially calculated using

Equation (3.42) when the mismatch was not taken into account. Now because the length between nodes E_2 or A_1 and nodes F_2 or B_1 is l_a, we need to modify Equation (3.42) where l_a replaces l. Hence

$$Z_{E2A1} - Z_{F2B1} = O'Q = \frac{l_a \sin 2\alpha_1 \cos^2 \theta}{1 - \sin^2 \alpha_1 \sin^2 \theta} \tag{3.46}$$

Considering Equations (3.46) and (3.45), we have

$$l_a = \left\{ \frac{\left(1 - \sin^2 \alpha_1 \sin^2 \theta\right)^2}{\left(1 - \sin^2 \alpha_1 \sin^2 \theta\right)^2 - \left(\sin 2\alpha_1 \cos^2 \theta\right)^2} \times \frac{\left(R_{o1} + R_{o2}\right)^2}{2} \left[1 - \cos\left(\frac{180^o}{m} \right) \right] \right\}^{\frac{1}{2}} \tag{3.47}$$

Results of the deformation of the fold with various α_1 and m during deployment are given in Section 3.7.

3.6 Generalisation of the basic element and its geometric properties

Only a rectangular element has been considered so far. The value of $\alpha_1 + \alpha_2$ is always 90^o. However, the element does not necessarily have to be rectangular. In this section an alternative design of the element will be explored.

A more general element is shown in Figure 3.11(a) where node B' replaces B. B' can be below or above B. The geometric parameters, such as radii, length and deformation of the cylindrical tube can be calculated accordingly.

Similar to the basic element in Section 3.3, R_{o1}, R_{o2} and R_i are defined as

$$R_{o1} = O_0 B' \tag{3.48}$$

$$R_{o2} = O_0 A \tag{3.49}$$

and

$$R_i = O_0 O \tag{3.50}$$

see Figure 3.11(b).

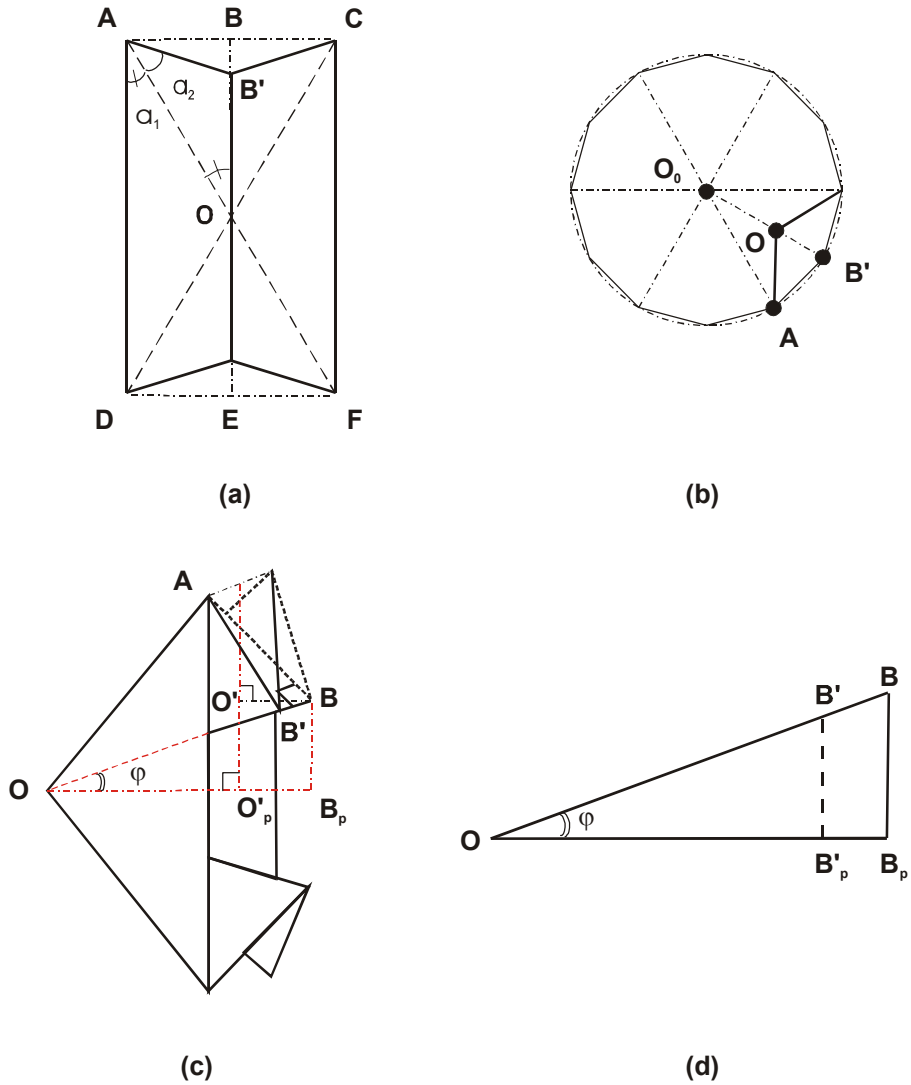

Figure 3.11 (a) A generalised element; (b) cross section views of the tube; (c) perspective view of the element and (d) geometric details.

From Figure 3.11(c) and (d),

$$R_{o1} = O_0O + OB'_p = R_i + OB_p \frac{OB'}{OB} \tag{3.51}$$

R_{o2} remains the same as it is in Equations (3.15) and (3.29) and R_i can also be found from Equations (3.27) and (3.30). Geometrically,

$$\frac{OB_p}{OB} = \cos\varphi \tag{3.52}$$

$$OB' = OB - BB' \tag{3.53}$$

where

$$\cos\varphi = \frac{\sin 2\alpha_1 \cos\theta}{1 - \sin^2\alpha_1 \sin^2\theta} \tag{3.54}$$

$$OB = \frac{l}{\tan\alpha_1} \text{ and } BB' = \frac{l}{\tan(\alpha_1 + \alpha_2)} \tag{3.55}$$

in which φ has been calculated in Equation (3.23). Substituting Equations (3.54) and (3.55) into (3.52) and (3.53) gives,

$$\frac{OB_p}{OB} = \frac{\sin 2\alpha_1 \cos\theta}{1 - \sin^2\alpha_1 \sin^2\theta} \tag{3.56}$$

$$OB' = \frac{l}{\tan\alpha_1} - \frac{l}{\tan(\alpha_1 + \alpha_2)} \tag{3.57}$$

Therefore, substituting Equations (3.27) and (3.30) and Equations (3.56) and (3.57) into (3.51) gives,

$$R_{o1} = \frac{l\sin\theta}{\tan\delta} - l\cos\theta + \left[\frac{l}{\tan\alpha_1} - \frac{l}{\tan(\alpha_1+\alpha_2)}\right] \times \left(\frac{\sin 2\alpha_1 \cos\theta}{1-\sin^2\alpha_1 \sin^2\theta}\right) \tag{3.58}$$

The relationships between y, which is the value of the mismatch between R_{o1} and R_{o2} normalised by l, and the deployment angle θ can also be considered. The results for various α_2 when $m = 6$ and $\alpha_1 = 45^o, 30^o$ or 60^o are drawn in Figure 3.12.

Figure 3.12(a) shows the value of y against θ when $\alpha_1 = 45^o$. When node B' is above node B, $\alpha_2 > 45^o$ and y is greater than zero. When node B' is below node B, $\alpha_2 < 45^o$ and y is smaller than zero. When $\alpha_1 = \alpha_2 = 45^o$, B' and B are at the same location, y is closer to zero. Therefore, it is preferable that α_2 is around 45^o to reduce mismatch between R_{o1} and R_{o2} during deployment. From Equation (3.38), the optimum design is when α_2 becomes 42.7^o. Figure 3.12(b) shows the value of y against θ when $\alpha_1 = 30^o$. y becomes closer to zero as α_2 decreases until 35.5^o. Figure 3.12(c) shows y against θ when $\alpha_1 = 60^o$. The optimum design is when α_2 becomes 44.2^o. However, it is found that the value of y varies dramatically during deployment, and $|y|$ is generally much larger than zero in comparison with the results when $\alpha_1 = 45^o$ or $\alpha_1 = 30^o$.

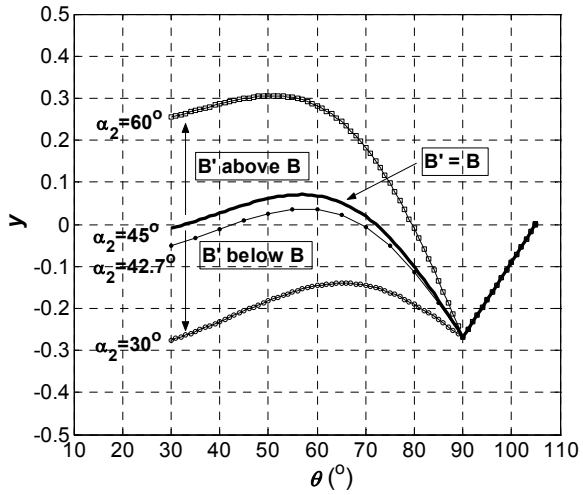

(a)

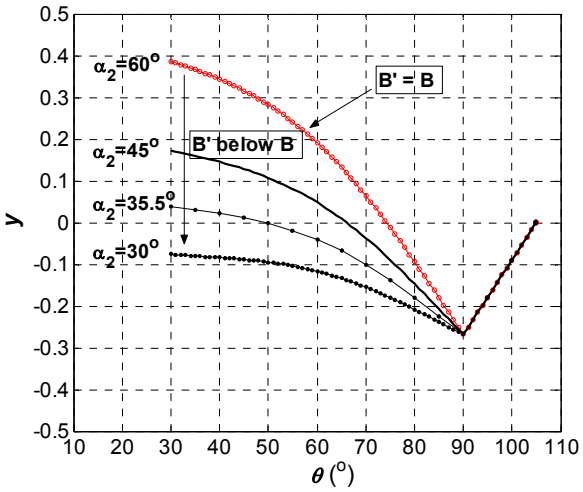

(b)

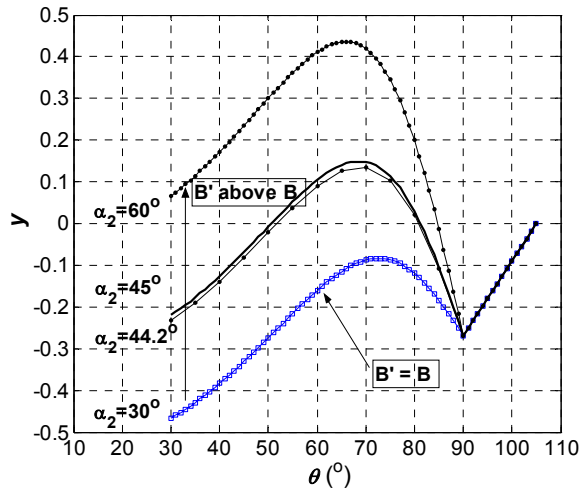

(c)

Figure 3.12 y **vs.** θ **for various** α_2 **when** m **= 6 and (a)** $\alpha_1 = 45^\circ$**, (b)** $\alpha_1 = 30^\circ$ **and (b)** $\alpha_1 = 60^\circ$**.**

Now consider the total length of the foldable cylindrical tube consisting of the general elements. Figures 3.13(a) and (b) show the perspective view of a single element during deployment and its planar projection, respectively. Since node B' replaces B, $O'Q$ in Equation (3.39) will also be replaced by $O'_2 Q$. Therefore, during the first phase of deployment, i.e., $\theta_0 \le \theta \le 90^o$, L is given by

$$L = n \times AD - (n-1) \times O'_2 Q \tag{3.59}$$

where

$$O'_2 Q = O'Q + HB' \tag{3.60}$$

in which AD and $O'Q$ has been calculated in Equations (3.20) and (3.42).

$$HB' = BB' \sin\varphi \tag{3.61}$$

where

$$BB' = \frac{l}{\tan(\alpha_1 + \alpha_2)} \tag{3.62}$$

$$\sin\varphi = \frac{\cos^2\alpha_1 - \sin^2\alpha_1 \cos^2\theta}{1 - \sin^2\theta \sin^2\alpha_1} \tag{3.63}$$

in which l is the length AB.

Substituting Equations (3.62) and (3.63) into (3.61) gives

$$HB' = \frac{l}{\tan(\alpha_1 + \alpha_2)} \frac{\cos^2\alpha_1 - \sin^2\alpha_1 \cos^2\theta}{1 - \sin^2\theta \sin^2\alpha_1} \tag{3.64}$$

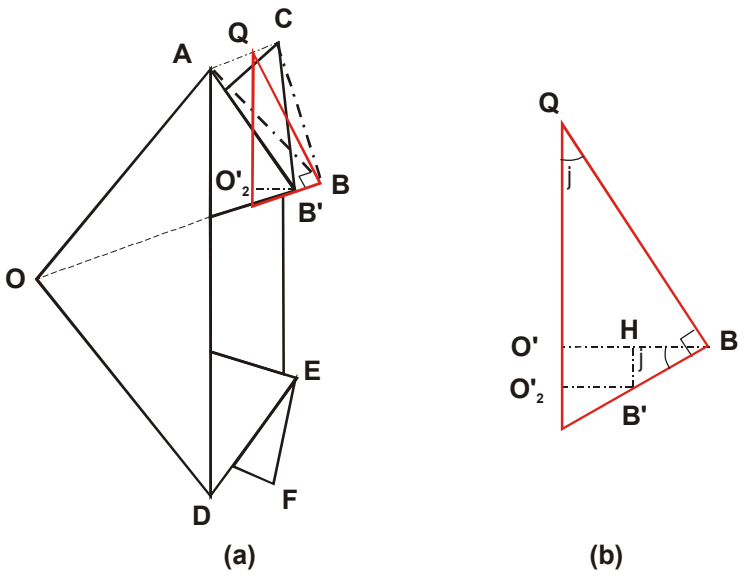

Figure 3.13 Most general element during deployment.
(a) Perspective view and (b) planar projection.

Then, substituting Equations (3.42) and (3.62) into (3.60) gives

$$O'_2 Q = \frac{l}{1-\sin^2\theta\sin^2\alpha_1}\left(\sin 2\alpha_1\cos^2\theta + \frac{\cos^2\alpha_1 - \sin^2\alpha_1\cos^2\theta}{\tan(\alpha_1+\alpha_2)}\right) \tag{3.65}$$

Consequently, L is defined as follow

$$L = n\frac{2l}{\tan\alpha_1} - \frac{(n-1)l}{1-\sin^2\theta\sin^2\alpha_1}\left(\sin 2\alpha_1\cos^2\theta + \frac{\cos^2\alpha_1 - \sin^2\alpha_1\cos^2\theta}{\tan(\alpha_1+\alpha_2)}\right) \tag{3.66}$$

On the second phase of deployment, i.e., θ varies from 90^o to θ_1, L is given by

$$L = nAD - (n-1)BB'$$

$$= n\frac{2l}{\tan\alpha_1} - \frac{(n-1)l}{\tan(\alpha_1+\alpha_2)} \tag{3.67}$$

The length l_a of the fold during deployment can also be calculated using Equation (3.45) in which the difference between Z_{E2A1} and Z_{F2B1} is equal to length $O'_2 Q$. $O'_2 Q$ has been calculated using Equation (3.65) and l needs to be replaced to $l_a \sin(\alpha_1 + \alpha_2)$ in order to take into account the mismatch between the elements. Therefore,

$$Z_{E2A1} - Z_{F2B1} = O'_2 Q = \frac{l_a \sin(\alpha_1 + \alpha_2)}{1 - \sin^2\theta \sin^2\alpha_1}\left(\sin 2\alpha_1 \cos^2\theta + \frac{\cos^2\alpha_1 - \sin^2\alpha_1 \cos^2\theta}{\tan(\alpha_1 + \alpha_2)}\right) \quad (3.68)$$

Considering Equations (3.68) and (3.45), we have

$$l_a = \left\{ \begin{array}{l} \dfrac{\left(1 - \sin^2\alpha_1 \sin^2\theta\right)^2}{\left(1 - \sin^2\alpha_1 \sin^2\theta\right)^2 - \sin^2(\alpha_1 + \alpha_2)\left(\sin 2\alpha_1 \cos^2\theta + \dfrac{\cos^2\alpha_1 - \sin^2\alpha_1 \cos^2\theta}{\tan(\alpha_1 + \alpha_2)}\right)^2} \\ \times \dfrac{(R_{o1} + R_{o2})^2}{2}\left[1 - \cos\left(\dfrac{180^o}{m}\right)\right] \end{array} \right\}^{\frac{1}{2}} \quad (3.69)$$

3.7 Models and discussions

In this section, results of radius, length and deformation of the foldable cylindrical tube during deployment will be presented. Although the optimum designs are $\alpha_1 = 46.7^o$ and $\alpha_2 = 43.3^o$, $\alpha_1 = 45^o$ and $\alpha_2 = 42.7^o$, or $\alpha_1 = 30^o$ and $\alpha_2 = 35.5^o$, the values of each α_1 and α_2 are close enough so that two special cases are considered where $\alpha_1 = \alpha_2 = 45^o$ and $\alpha_1 = \alpha_2 = 30^o$. For convenience, the model with $\alpha_1 = \alpha_2 = 45^o$ and $\alpha_1 = \alpha_2 = 30^o$ are called as Models 1 and 2, respectively. Model 1 uses the rectangular elements and Model 2 uses the general elements. Models 1 and 2 when $m = 6$ in the fully folded and expanded configurations are shown in Figure 3.14.

(a)

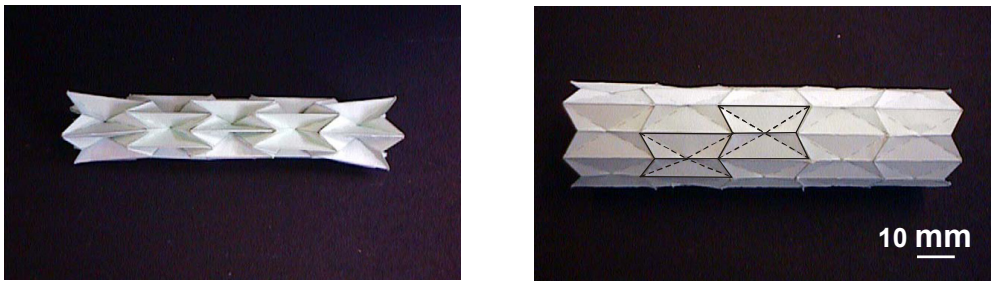

(b)

Figure 3.14 (a) Models 1 and (b) Model 2
in its fully folded and fully expanded configurations when *m* = 6.

3.7.1 Radius

Figures 3.15(a) and (b) show the outer and inner radii of each model, R_{o1}, R_{o2} and R_i of Models 1 and 2 normalized by the length l during deployment when m is 6. θ_0 and θ_1, which are deployment angles in the fully folded and expanded configurations, are 30^o and 105^o, respectively. The inner radius R_i gradually increases during deployment for both models. For Model 1, R_{o1} is greater than R_{o2} from θ being between 33^o and 72^o. For Model 2, R_{o1} is always smaller than R_{o2}. The ratio of the value of R_{o1} in the fully folded configuration to R_{o1} in the fully expanded configuration is denoted as R^*. R^* is 51.4% and 47.8% for Models 1 and 2, respectively.

Figure 3.16 shows the relationship of the ratio R^* vs. m. It is noted that R^* decreases with respect to an increasing m in both models. In other words, a larger m

enables the models to be folded more compactly in the radial direction. In comparison with Model 1, Model 2 has a lower value of R^* and hence folds more compactly until m is 9. However, the difference in the values of R^* between Models 1 and 2 becomes insignificant when m is larger than 9.

As mentioned in Chapter 2, the fully folded radius of the currently available stent grafts for the treatment of oesophageal cancer and abdominal aortic aneurysm is about 20 - 35% of the fully expanded radius. When m = 9, R^* of Models 1 and 2 is 34.7% and 33%, respectively. When m = 20, R^* becomes about 15.7% for both models. Table 3.2 shows dimensions of the origami stent graft with various values for m when the expanded diameter is 26 mm. A greater m results in more compact folding. However, it causes difficulty in folding process since each element becomes small and potentially the thickness of the stent graft material becomes an important issue. Therefore, m of the element should be selected to balance these two factors.

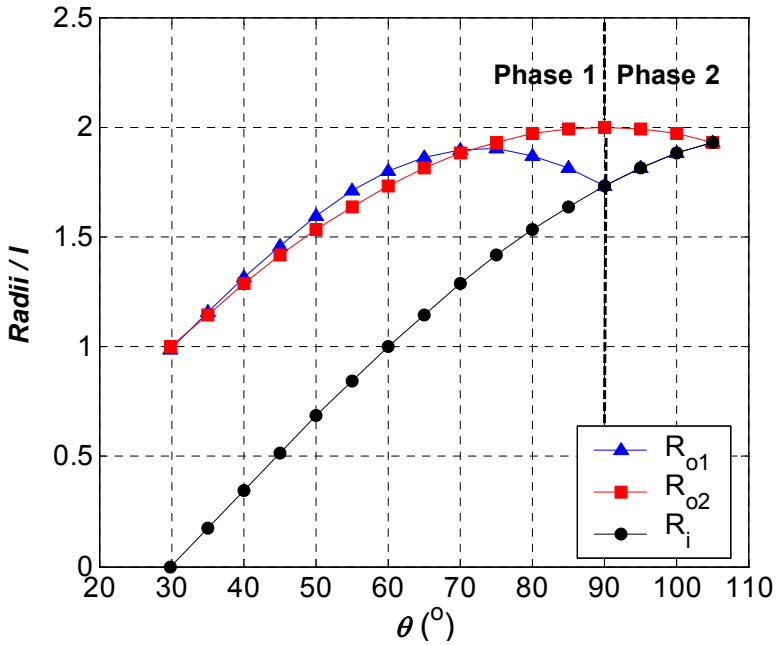

(a)

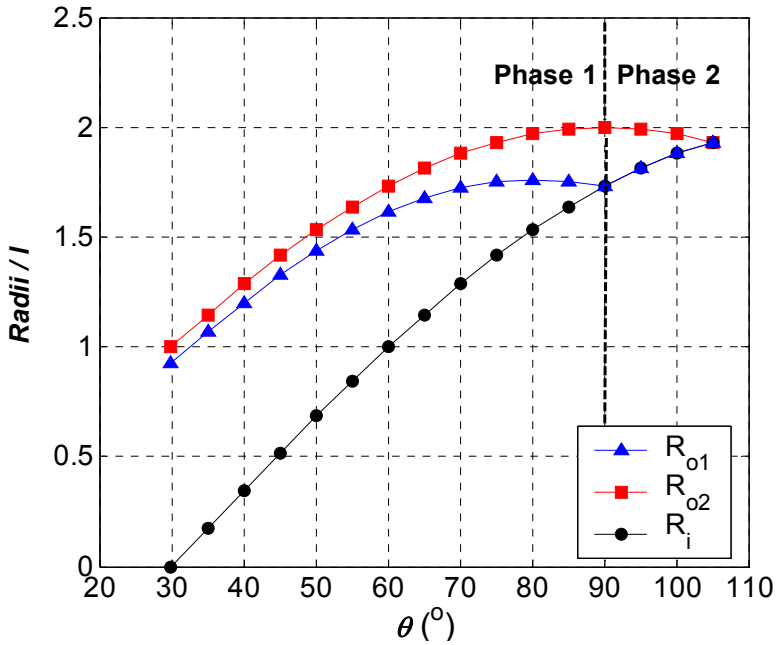

(b)

Figure 3.15 R_{o1}, R_{o2} **and** R_i **vs.** θ **when** m **= 6. (a) Model1 and (b) Model 2.**

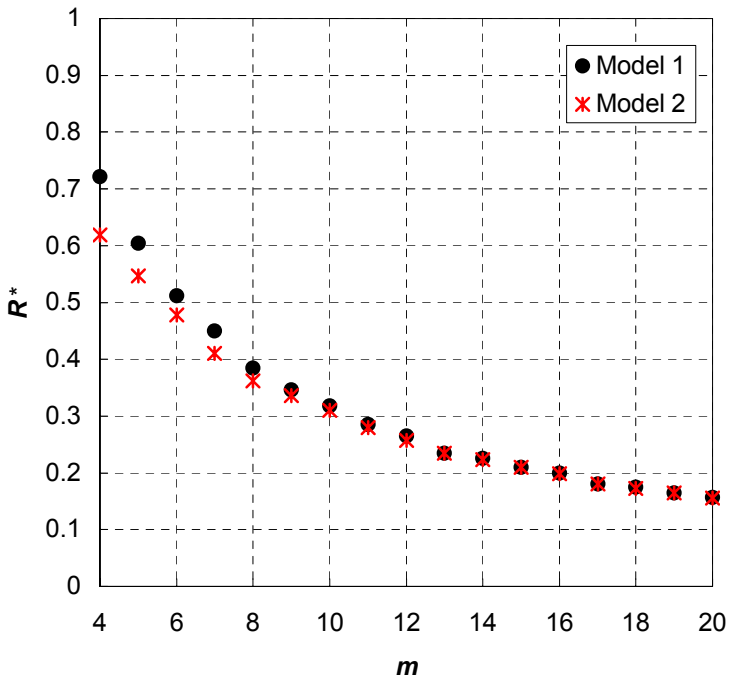

Figure 3.16 ***R**** **vs.** ***m*.**

Table 3.2 Dimensions of the origami stent graft with various *m*.

Expanded diameter (mm)	26				
m	9	12	14	16	20
R^* x 100 (%)	34.7	26.5	22.5	20.0	15.7
Folded diameter (mm)	9.00	6.89	5.85	5.2	4.08
Catheter (Fr./mm)	28/9.24	21/6.93	18/5.94	16/5.28	13/4.29
Element size (mm)	9.08	6.80	5.83	5.11	4.08

3.7.2 Length

The ratio of the total length L in the fully folded configuration with respect to in the fully expanded configuration is denoted as L^*. Figure 3.17 shows L^* versus various n for $m = 6$. It is noted that for both models, the ratio L^* slowly decreases as n increases. Both models are folded more compactly in the longitudinal direction as n increases. The value of L^* becomes nearly constant when n is greater than 8, so there is no particular benefit in increasing the number n of the elements above 8. In Model 1, it can be folded up into 63% of the length in its fully expanded configuration, while, in the Model 2, it is 86%. Compared to Model 1, Model 2 is folded less compactly in the longitudinal direction. Therefore, Model 1 is preferred for uses where longitudinal folding is desirable to allow access of the stent graft to a narrow blocked site, whereas Model 2 is preferred for uses when medical practitioners prefer the longitudinal shortening to be minimised.

Figure 3.18 shows the value of L^* of Model 1 for different values of m when $n = 8$. It is noted that L^* becomes smaller as m increases. This is because the deployable angle in the fully folded configuration, θ_0, becomes smaller as m increases. Thus a larger m reduces L^* and R^*.

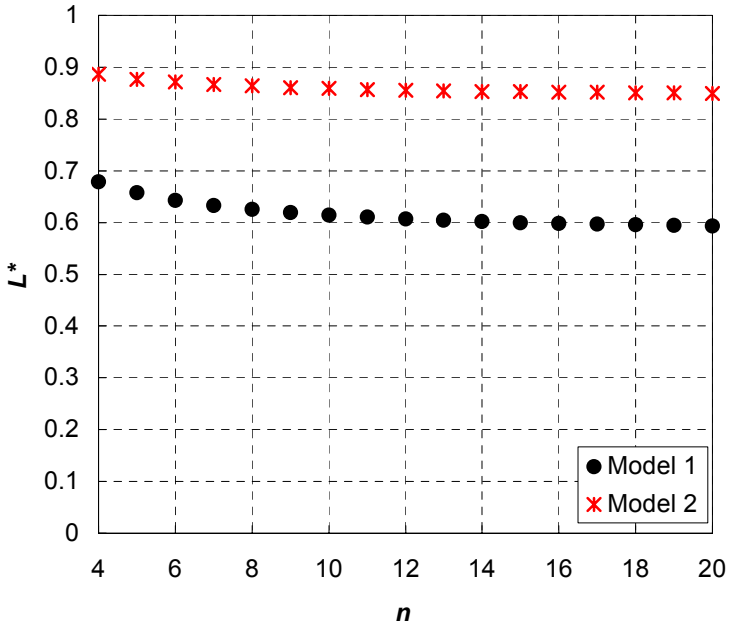

Figure 3.17 *L vs. *n* when *m* = 6.**

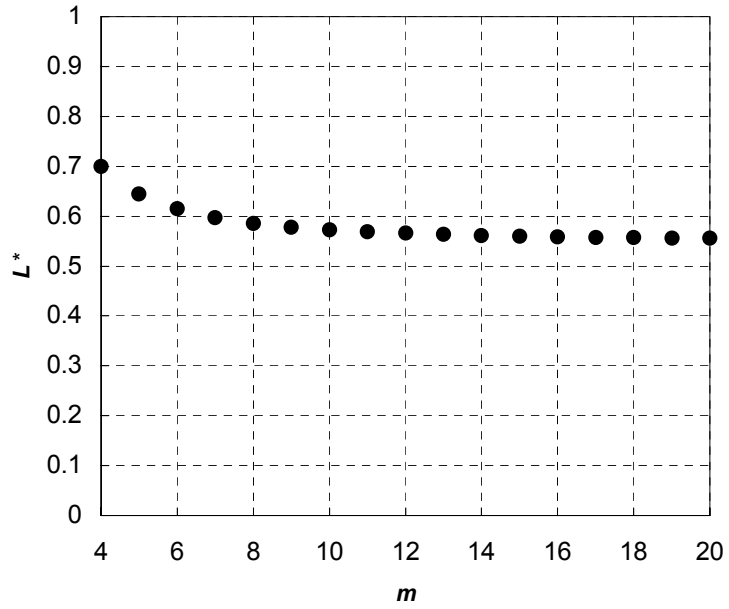

Figure 3.18 *L vs. *m* when *n* = 8.**

3.7.3 Deformation

Figure 3.19 shows a plot of l_a / l_o versus the deployable angle θ, for various element numbers m for Model 1. l_o is the original length between nodes A_1 and B_1 before connecting two elements in a longitudinal direction. Consider the initial case where $m = 6$. From the figure, it is noted that l_a / l_o becomes 1 when $\theta = 33^o$ and 72^o. This is where the foldable cylindrical tube admits unstrained configuration. Between these angles the shortening of l_a is less than 0.3%. However it increases dramatically while θ approaches 90^o. When θ becomes 105^o where the tube is fully expanded, l_a becomes equal to l_o again and the structure becomes unstrained. Moving from one unstrained configuration to the other between θ of 72^o to 105^o requires larger deformation. The structure may not be expanded smoothly, and could even be snapped. The behaviour of the shortening is different when m increases, which is shown next.

If we take m = 18, l_a is not shortened very much when θ is around 90^o. The deformation between unstrained configurations at the end of deployment, i.e. when $\theta = 85^o$ and 92.5^o, is smaller. However, it can be seen that it is shortened more at the beginning of deployment compared with the case m = 6. The optimum solution is m = 9. The shortening of l_a is less than 1.5 % during the deployment.

Figure 3.20 shows a plot of l_a / l_o versus the deployment angle θ for various element number m for Model 2. The value of l_a / l_o becomes smaller as m increases. For m = 18, the shortening of l_a is less than 0.4%, which is less than the results for Model 1.

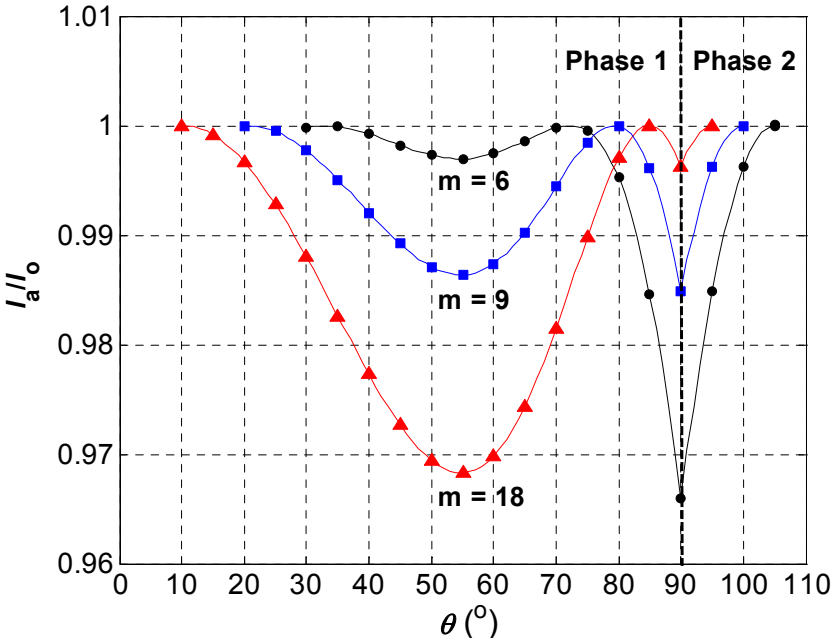

Figure 3.19 Plots of I_a/I_o vs. θ with various m for Model 1.

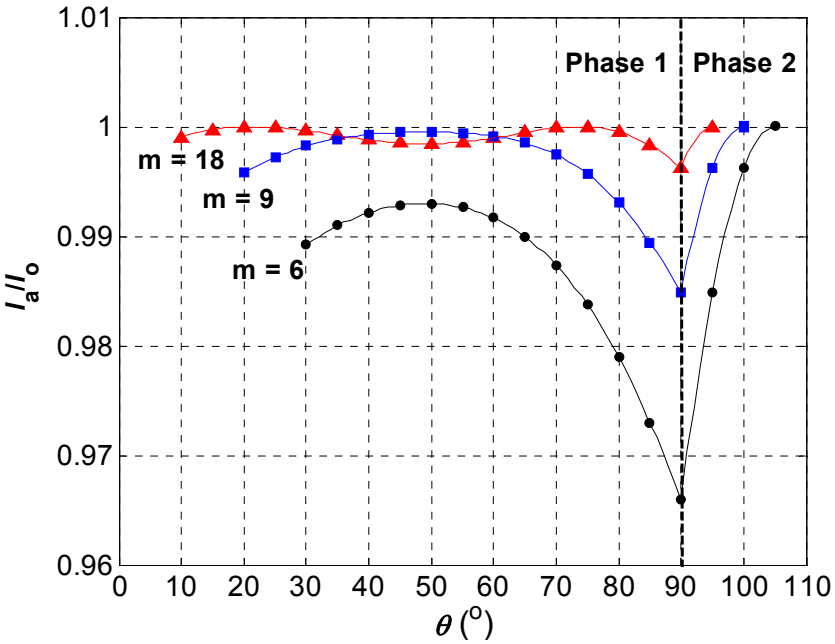

Figure 3.20 Plots of I_a/I_o vs. θ with various m for Model 2.

3.8 Variation of the folding patterns

In addition to folding patterns using the general elements, further variations are possible.

3.8.1 Centre folding

The pattern of folds described in the previous sections can be generalised further by the introduction of an extra valley fold between the intersections O and P (see Figure 3.21). Node B' can be below or above node B. The length OP affects the overall length when the structure is fully folded but has no effect on the radius during folding.

3.8.2 Double folding

The pattern of folds described so far involves a peak at the centre of an element when it is folded (see Figure 3.23a). As shown in Figure 3.22 additional folding lines can be added in the centre in order to level the peak. The element can be folded more compactly and therefore the overall radius can be further reduced (see models shown in Figure 3.23b).

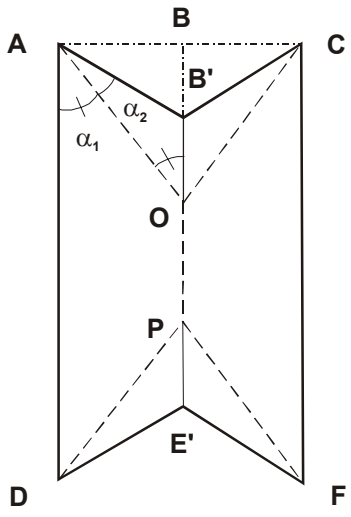

Figure 3.21 Element with an extra central valley between O and P.

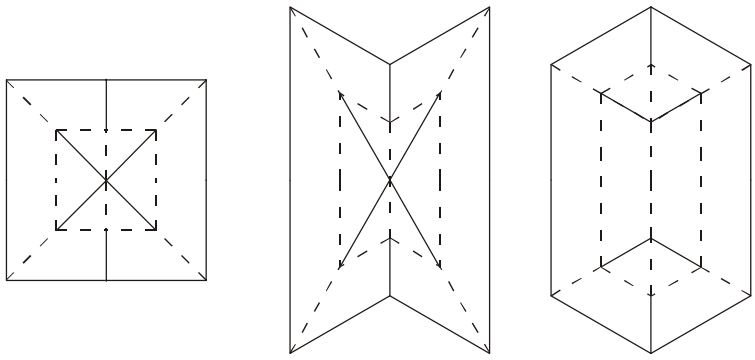

Figure 3.22 Elements with additional folds in the centre.

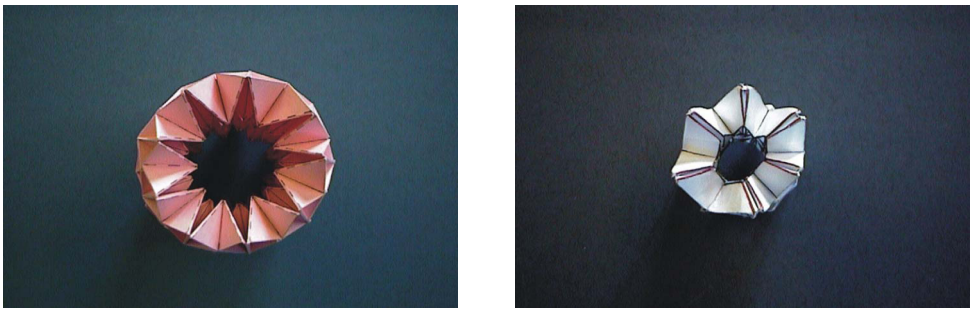

(a) **(b)**

Figure 3.23 The end views of the foldable tubes
(a) with and (b) without peaks at the centre.

3.8.3 Unsymmetrical folding

The patterns of folds discussed so far are symmetrical about both the central longitudinal fold and an imaginary circumferential line. However, this is not essential.

For example, Figures 3.24(a) shows diagrams of the elements which are symmetrical only about the central longitudinal fold. The upper and lower halves of the element are based on the rectangle element and the general element, respectively. The development of the foldable cylindrical tube with the elements is shown in Figure 3.24(b). The neighbouring rows are shifted by a half-unit. Accordingly, the

element of alternate rows is reversed in the longitudinal direction as illustrated in bold outline.

The diagram of the other possible element design is shown in Figures 3.25, which are symmetrical only about an imaginary line in circumferential direction. It is a combination of two halves of different elements, except that the central longitudinal fold extends at an angle to the longitudinal direction.

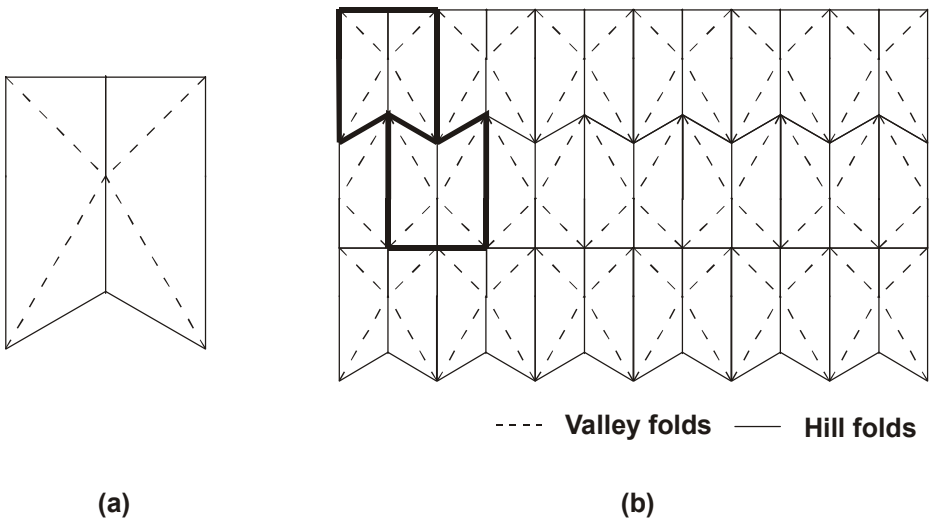

Figure 3.24 (a) Single element with a folding pattern and (b) the development of the foldable cylindrical tube with the unsymmetrical folding.

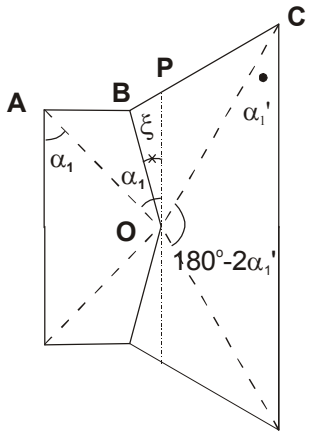

Figure 3.25 Element with the unsymmetrical folding.

As shown in Figure 3.25, the fold OB leans to angle ξ with respect to OP. Since the sum of alternation of the centre angles of node O is equal to 180^o to make an element foldable, see Equation (2.5)

$$2(\alpha_1 - \xi) + 180^o - 2\alpha_1' = 180^o \tag{3.70}$$

Consequently,

$$\xi = \alpha_1 - \alpha_1' \tag{3.71}$$

Unlike the previous models, this foldable cylindrical tube cannot be divided into such elements by simple repetition. A possible arrangement using the element is shown in Figure 3.26.

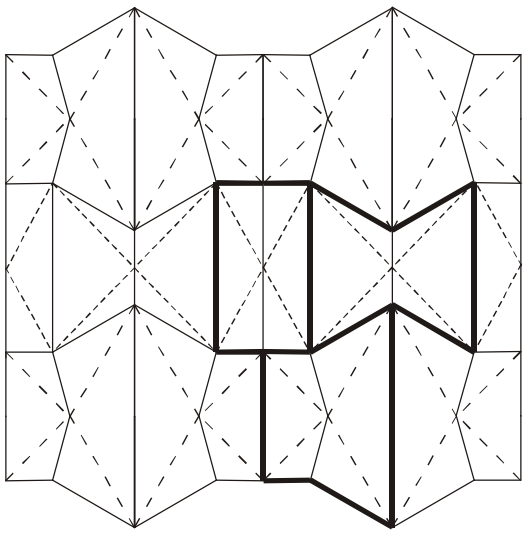

Figure 3.26 Pattern of a foldable cylindrical tube using three types of elements.

3.8.4 Folding pattern for conical tubes

The patterns of folds discussed previously are applicable to cylindrical tubes. They can be modified for conical tubes. Figure 3.27 shows the development of the foldable conical tube. The photographs of a cone in its fully folded and expanded configurations are shown in Figure 3.28.

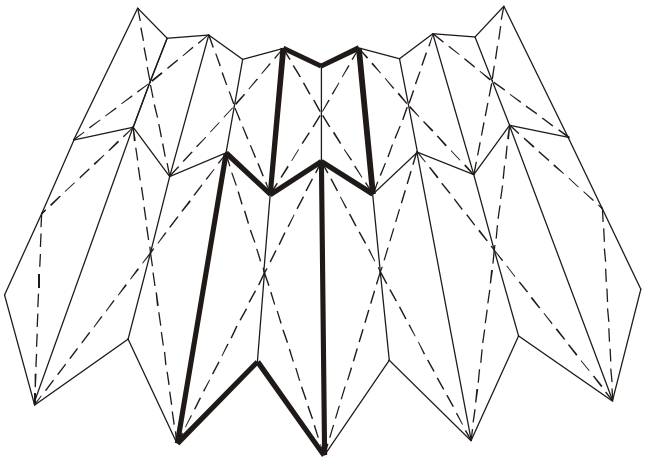

Figure 3.27 Elements for a foldable conical tube.

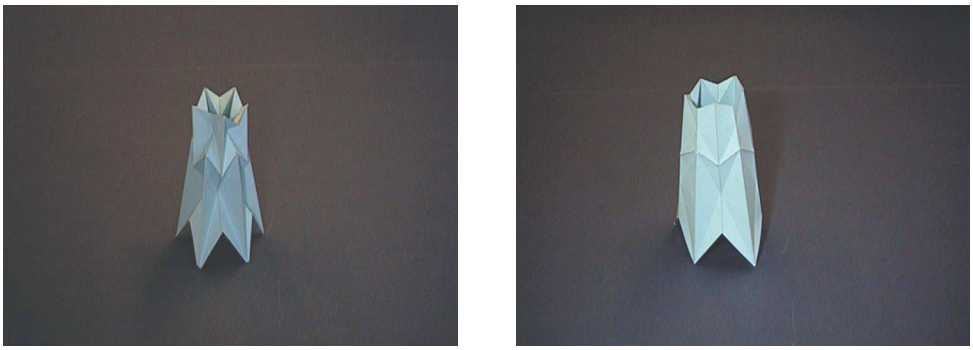

(a) **(b)**

Figure 3.28 Foldable cone in its (a) fully folded and (b) fully deployed configurations.

3.9 Conclusions

In this chapter a new type of a single piece stent graft has been developed. A detailed symmetric design of a foldable cylindrical tube for the stent graft has been presented. Folding is achieved by dividing the structure into a series of identical foldable elements. Particular attention has been paid to two types of elements: rectangular elements and general elements. Folding patterns for each type of element was obtained. Both patterns allow the stent graft to be folded and expanded both radially and longitudinally. The important geometric parameters of the elements and of the foldable cylindrical tube are defined and analysed.

The relationships among the design of the elements, the number of elements in the circumferential and longitudinal directions and the folded dimensions of the stent graft have been derived. It has been found that compact folding in the radial direction can be achieved by increasing the number of circumferential elements. However, a large number of elements may cause manufacturing difficulty. A compromise can be found to address both concerns. It has also been found that the stent graft can be folded compactly in the longitudinal direction as both the number of the circumferential and longitudinal elements increase, and that the ratio of its constriction depends on the design of the element.

A geometric mismatch during deployment has also been identified. The elements have to deform when the structure is expanded. Optimum designs which minimise the deformation have been found.

Variations to the general folding patterns of both cylindrical and conical tubes have also been discussed, though without detailed geometric calculation.

CHAPTER 4

FOLDABLE CYLINDRICAL TUBES WITH HELICAL FOLDS

The rotationally symmetric design of the origami stent graft described in Chapter 3 provides compact folding. But it has low radial stiffness because the longitudinal folds coincide with the collapse mechanism when the tube fails under radial pressure. A general approach to improve the radial stiffness is to replace longitudinal folds with helical ones.

Section 4.1 introduces basic concepts of the helical folds for cylindrical tubes. Advantages of the helical folds are discussed. In Section 4.2, the radius of the tube during deployment is defined and analysed. To understand the deployment process, the fold-shorting during deployment is calculated.

In order to obtain the optimum helical fold design, i.e. the optimum locations for the helical folds, the buckling of a thin-walled tube under torsion is considered. When a thin-walled tube buckles, a pattern of peaks and valleys forms on the structure. This buckling pattern is utilised to define the position of the helical folds so that the cylindrical tube can be easily folded and unfolded by twisting the tube. Section 4.3 finds the buckling pattern for a thin-walled tube using analytical solutions. The buckling pattern on a cardboard model under torsion is examined. In Section 4.4, the intentional helical folds of the foldable cylindrical tube are compared with the buckling patterns to establish a link between these parameters. Section 4.5 concludes this chapter.

4.1 Helical folds

Helical folds can be easily introduced by adjusting the joining positions of the left and right longitudinal edges of a developed tube surface. Figure 4.1(a) shows the surface of a foldable cylindrical tube with helical folds. It is based on rectangular elements where $\alpha_1 = \alpha_2 = 45^o$. To form a cylindrical tube with helical folds the horizontal opposite edges of the sheet, i.e., section a_2-a_3 and b_1-b_2, etc., are joined together. In this case there are 6.5 elements in one turn circle of a helix. Always a half element needs to be added at the end of each full circumference to allow connection of the left and right edges.

The major helical folds are denoted as H_A and H_B. They are orthogonal to one another as shown in Figure 4.1(a). Figures 4.1(b) and (c) show perspective views of the cylindrical tube in the unfolded and folded configurations. H_A is a single long fold which spirals around the circumference of the tube, while, H_B runs diagonally from one open end to the other.

The number of H_A and H_B type helices can vary. A foldable cylindrical tube with more than one H_A type helix can be made by adjusting the joining position of the left and right edges of the sheet shown in Figure 4.1(a). Figure 4.2 shows the development of the model with two helices, in which the opposite edges of the sheet a_3-a_4 and b_1-b_2, etc. are joined together. Photographs of the foldable cylinders with two and three helices in fully folded and expanded configurations are shown in Figures 4.3(a) and (b). The separate helices are shown in different colours. The number of H_B type of helices depends on the number of element *m*.

Helical folds bring a number of important advantages for the stent graft. Firstly, as shown in Figure 4.1(b), H_A type helices connect all of the elements like ribbons, enabling the folding and expansion processes to be synchronised among the elements. Secondly, the helical folds provide greater radial stiffness in the expanded configuration of the tube because H_B type folds no longer coincide with the collapsed hinge lines of the tube under external radial pressure. The stent graft will be permitted to collapse only

under torsion at both ends. Since torsional loadings are rare in the human body, i.e. oesophageal and aorta, the stent graft will not collapse easily.

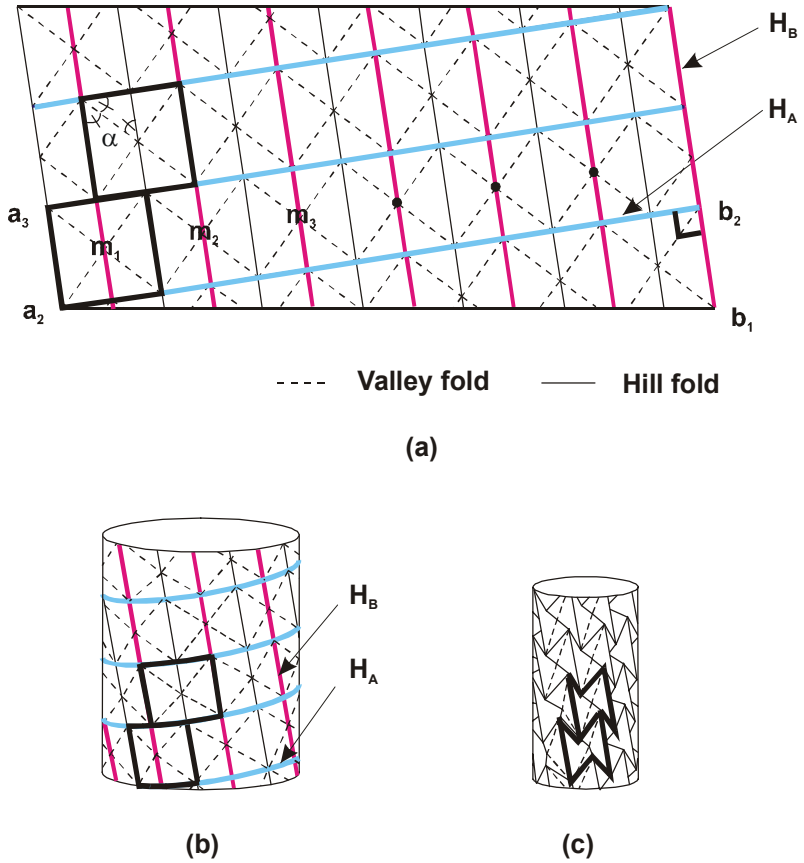

Figure 4.1 (a) Development of a helical foldable cylindrical tube.
(b) and (c) perspective view of the tube in its unfolded and folded configurations.

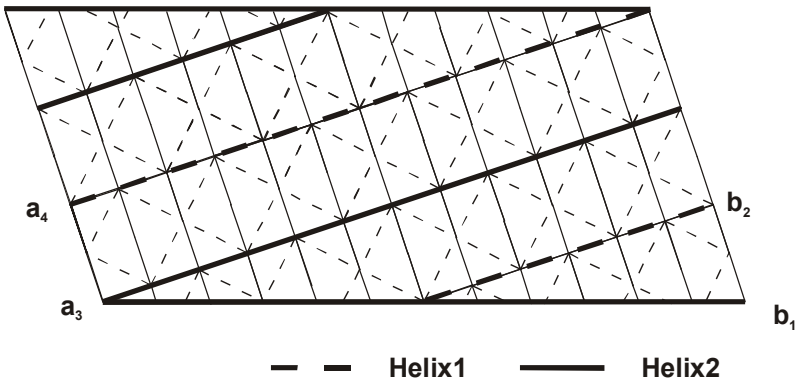

Figure 4.2 Development of a foldable tube with two H_A type helices. a_3-a_4 and b_1-b_2 are jointed together to form a tube.

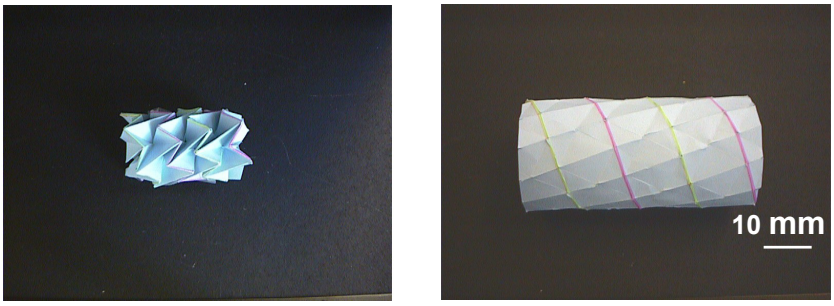

Fully folded Fully expanded

(a)

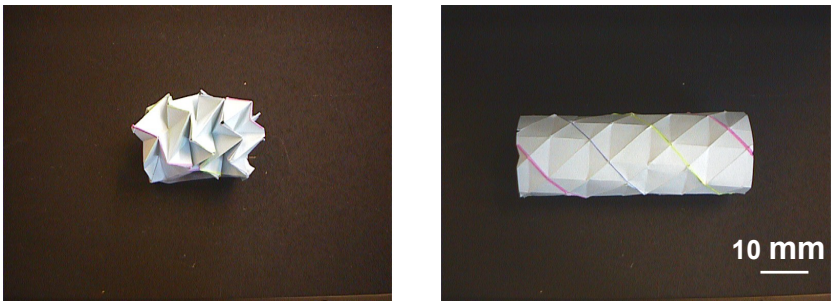

Fully folded Fully

(b)

Figure 4.3 Photographs of foldable cylindrical tubes with (a) two and (b) three helical folds.

4.2 Geometry of the helical-type foldable cylindrical tube

4.2.1 Helical angle

Figure 4.4 shows the configuration of a foldable cylindrical tube with helical folds during deployment. The typical element is identical to that described in Section 3.2. The angles of H_A and H_B folds with respect to the horizontal base line are denoted as β_A and β_B, respectively. Note that β_A and β_B vary during deployment because both the length and diameter of the tube alter. However, H_A and H_B folds remain orthogonal to one another, and $a_2b_2'$and b_1b_2 intersect at b_2'. Hence, β_A is:

$$\beta_A = \arctan\left(\frac{b_1b_2'}{a_2b_2'}\right) \tag{4.1}$$

$$\beta_B = \frac{\pi}{2} - \beta_A \tag{4.2}$$

in which

$$b_1b_2' = b_1b_2 - b_2b_2' \tag{4.3}$$

$$a_2b_2' = (2m+1) \times \frac{AC}{2} \tag{4.4}$$

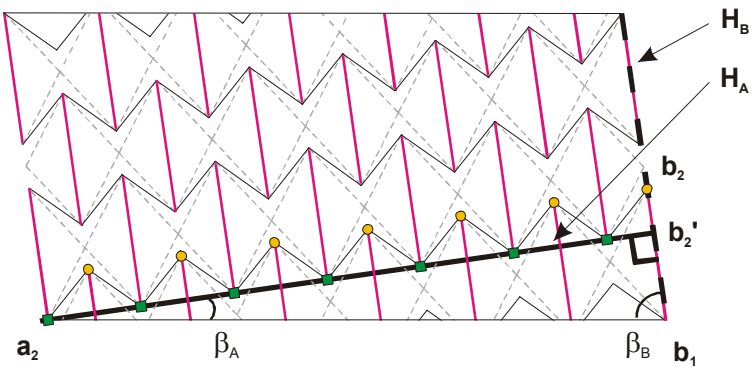

Figure 4.4 Configuration of the foldable cylindrical tube with helical folds during deployment.

where b_1b_2 has been calculated as AD in Equation (3.20) and b_2b_2' is as O'_2Q in Equation (3.65). m is the number of elements along a_2b_2'. AC has been calculated in Equation (3.14). Therefore, Equations (4.3) and (4.4) become

$$b_1b_2' = \frac{2l}{\tan\alpha_1} - \frac{l\sin 2\alpha_1\cos^2\theta}{1-\sin^2\alpha_1\sin^2\theta} - \frac{l}{\tan(\alpha_1+\alpha_2)}\frac{\cos^2\alpha_1-\sin^2\alpha_1\cos^2\theta}{1-\sin^2\theta\sin^2\alpha_1}$$

$$= l\left[\frac{2\tan(\alpha_1+\alpha_2)\cos^2\alpha_1-\sin\alpha_1\cos\alpha_1+\sin^2\alpha_1\tan\alpha_1\cos\theta}{\tan\alpha_1\tan(\alpha_1+\alpha_2)(1-\sin^2\theta\sin^2\alpha_1)}\right] \tag{4.5}$$

$$a_2b_2' = (2m+1)l\sin\theta \tag{4.6}$$

Substituting Equations (4.5) and (4.6) into Equation (4.1) gives

$$\beta_A = \arctan\left[\frac{2\tan(\alpha_1+\alpha_2)\cos^2\alpha_1-\sin\alpha_1\cos\alpha_1+\sin^2\alpha_1\tan\alpha_1\cos^2\theta}{(2m+1)\sin\theta\tan\alpha_1\tan(\alpha_1+\alpha_2)(1-\sin^2\alpha_1\sin^2\theta)}\right] \tag{4.7}$$

Figure 4.5 shows the results of the helical angle β_A versus deployable angle θ when $m = 4$, 6 and 12 and $\alpha_1 = \alpha_2 = 45^o$. In all cases, β_A decreases until θ reaches 55^o and then increases. β_A becomes smaller if m is large.

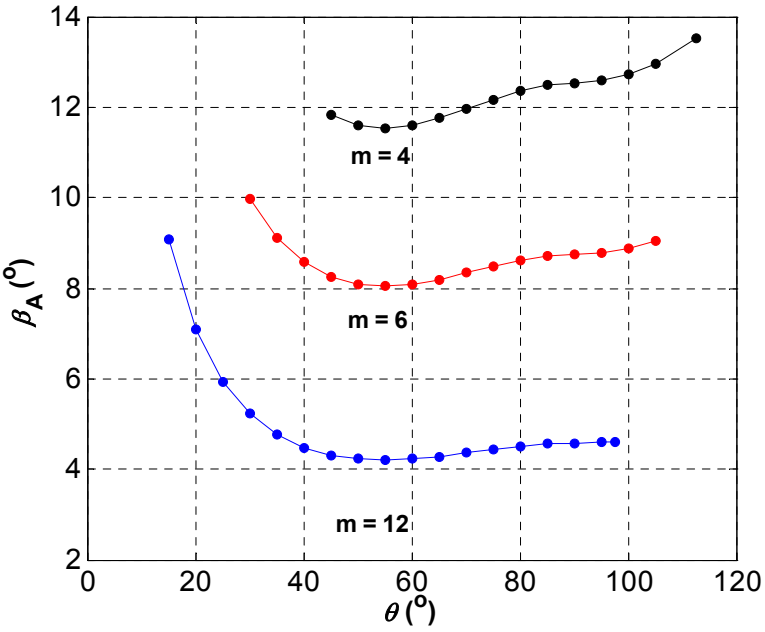

Figure 4.5 β_A with various θ for m = 4, 6 and 12 when $\alpha_1 = \alpha_2 = 45^\circ$.

4.2.2 Radius

For simplicity, consider the tube consisting of the rectangular elements, i.e., $\alpha_1 + \alpha_2 = 90^\circ$ as described in Section 3.2. Figure 4.6(a) shows the element of the tube in the local coordinate system of (x', y', z'). Because of the arrangement of the elements, two coordinate systems are introduced. Figures 4.6(b) and (c) show a 3-dimensional schematic and top-view of the cylindrical tube in (X, Y, Z) coordinates, respectively. The distance from the Z axis of the model to nodes B and A are denoted as R_{o1} and R_{o2}, respectively, and R_{o1} and R_{o2} are obtained as follows.

Firstly, nodes A and B are defined in the local coordinate system of (x', y', z'). From Figure 4.6(a), these are given as A (0, 0, 0) and B ($O'B$, $AC/2$, $O'Q$) where AC, $O'B$ and $O'Q$ have been calculated in Equations (3.14), (3.24) and (3.42).

Secondly, we transform A and B from (x', y', z') to (X, Y, Z) coordinate systems. Nodes A and B are rotated by β_A about the x' axis and then by ϕ about the z' axis. Then,

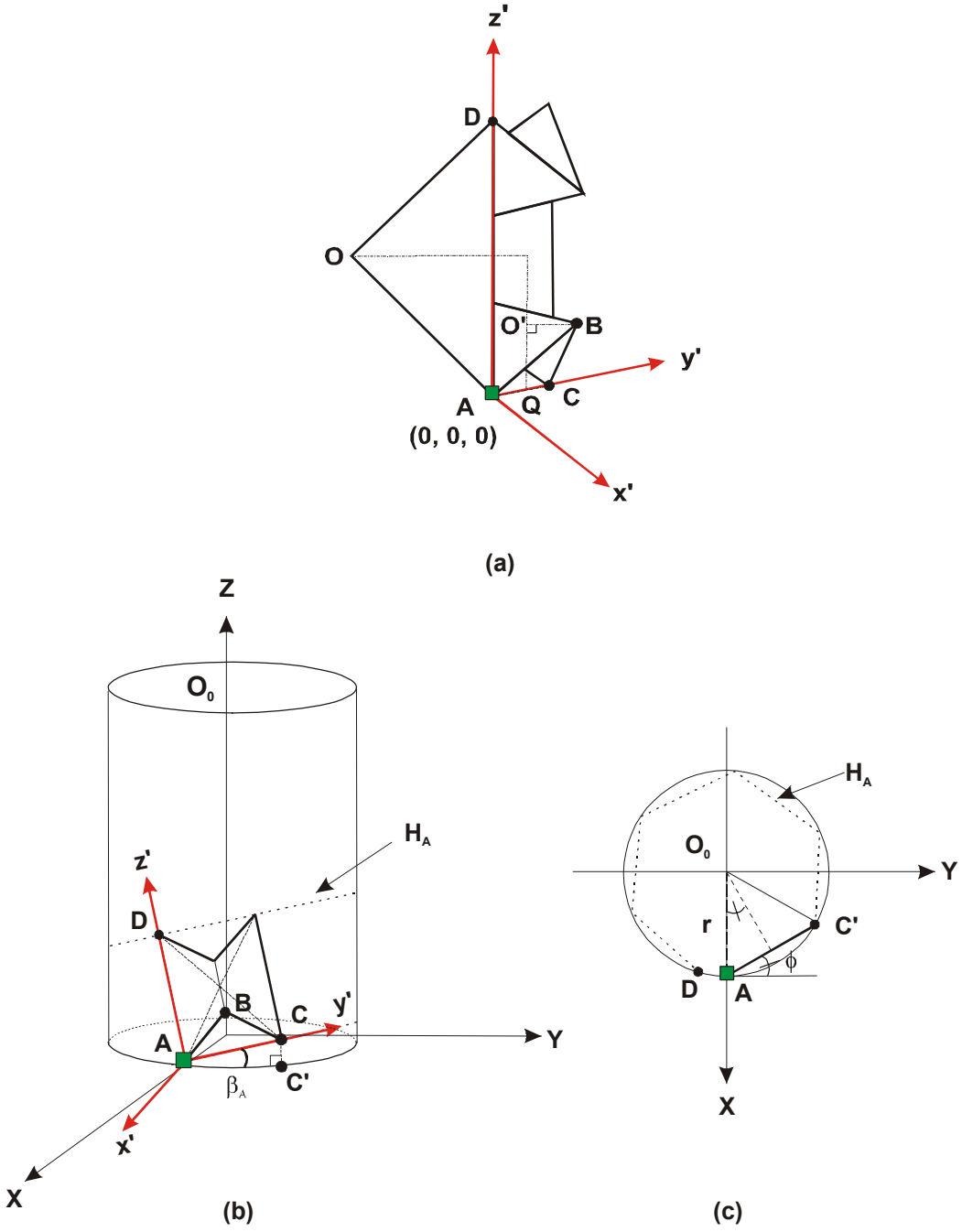

Figure 4.6 (a) Element (x', y', z') coordinates; (b) foldable cylindrical tube with helical folds and (c) its top's view in (X, Y, Z) coordinates.

they are translated by r in the X axis where r is the radius of the tube, also shown in Figure 4.6(c). The rotation matrix M is

$$[M]=\begin{bmatrix}\cos\phi & -\sin\phi & 0\\ \sin\phi & \cos\phi & 0\\ 0 & 0 & 1\end{bmatrix}\begin{bmatrix}1 & 0 & 0\\ 0 & \cos\beta_A & -\sin\beta_A\\ 0 & \sin\beta_A & \cos\beta_A\end{bmatrix}=\begin{bmatrix}\cos\phi & -\sin\phi\cos\beta_A & \sin\phi\sin\beta_A\\ \sin\phi & \cos\phi\cos\beta_A & -\cos\phi\sin\beta_A\\ 0 & \sin\beta_A & \cos\beta_A\end{bmatrix} \quad (4.8)$$

Therefore, the transformation is

$$\begin{bmatrix}X\\ Y\\ Z\end{bmatrix}=[M]\begin{bmatrix}x'\\ y'\\ z'\end{bmatrix}+\begin{bmatrix}r\\ 0\\ 0\end{bmatrix} \quad (4.9)$$

ϕ is equal to $\angle AO_oC'/2$, see Figure 4.6(c). There is

$$r\sin\phi=\frac{AC'}{2} \quad (4.10)$$

where

$$AC'=AC\cos\beta_A=2l\sin\theta\cos\beta_A \quad (4.11)$$

In Figure 4.4, because

$$2\pi r=a_2b_1 \quad (4.12)$$

where

$$a_2b_1=\frac{a_2b_2'}{\cos\beta_A}=\frac{(2m+1)l\sin\theta}{\cos\beta_A} \quad (4.13)$$

due to Equation (4.6). Therefore,

$$r=\frac{(2m+1)l\sin\theta}{2\pi\cos\beta_A} \quad (4.14)$$

Substituting Equations (4.14) and (4.11) into (4.10) gives

$$\phi = \arcsin\left(\frac{2\pi\cos^2\beta_A}{2m+1}\right) \tag{4.15}$$

Once r and ϕ are known, the positions of nodes A and B in (X, Y, Z) coordinate systems can be calculated using Equation (4.8) and (4.9), leading to R_{o1} and R_{o2}.

For general elements shown in Figure 3.11, node B' replaces B. Therefore, from Figure 3.13 $O'_2 B'$ and $O'_2 Q$ need to replace $O'B$ and $O'Q$, respectively. $O'_2 B'$ is derived as follows

$$O'_2 B' = O'B - HB \tag{4.16}$$

where $O'B$ has been calculated in Equation (3.24) and

$$HB = BB'\cos\varphi \tag{4.17}$$

in which BB' and $\cos\varphi$ have been calculated in Equations (3.55) and (3.54), therefore,

$$HB = \frac{l}{\tan(\alpha_1+\alpha_2)}\frac{\sin 2\alpha_1\cos\theta}{1-\sin^2\theta\sin^2\alpha_1} \tag{4.18}$$

and

$$O'_2 B' = l\cos\theta\frac{\cos^2\alpha_1-\sin^2\alpha_1\cos^2\theta}{1-\sin^2\theta\sin^2\alpha_1} - \frac{l}{\tan(\alpha_1+\alpha_2)}\frac{\sin 2\alpha_1\cos\theta}{1-\sin^2\theta\sin^2\alpha_1} \tag{4.19}$$

$O'_2 Q$ has been calculated in Equation (3.65). Again, the position of nodes A and B in the global coordinate system (X, Y, Z) can be obtained.

4.2.3 Deformation

In Section 3.3 (Figure 3.7), it is found that there is a mismatch between radii of the element when they are connected in the longitudinal direction. The same occurs in the deployment of the tubes with helical folds.

The length between the nodes E_2 or A_1 and F_2 or B_1 has been denoted as l_a

$$l_a = \left[\left(R_{E2A1}\cos\delta_{E2A1} - R_{F2B1}\cos\delta_{F2B1}\right)^2 + \left(R_{E2A1}\sin\delta_{E2A1} - R_{F2B1}\sin\delta_{F2B1}\right)^2 + \left(Z_{E2A1} - Z_{F2B1}\right)^2\right]^{\frac{1}{2}} \quad (4.20)$$

In the cylindrical coordinate system, the coordinate of nodes E_2 or A_1 are (R_{E2A1}, δ_{E2A1}, Z_{E2A1}) and those of nodes F_2 or B_1 are (R_{F2B1}, δ_{F2B1}, Z_{F2B1}) where R_{E2A1} and R_{F2B1} are $(R_{o1}+R_{o2})/2$; $\delta_{E2A1} = 0^o$; $\delta_{F2B1} = \arctan(Y/X)$ in which Y and X are the coordinates of node B calculated in Section 4.2.2. The difference between Z_{E2A1} and Z_{F2B1} is the value of the Z coordinate of node B as follows

$$Z_{E2A1} - Z_{F2B1} = Z = \frac{AC}{2}\sin\beta_A + O'_2 Q\cos\beta_A \quad (4.21)$$

Substituting Equations (3.14) and (3.65) into (4.21)gives

$$Z_{E2A1} - Z_{F2B1} = l\left\{\begin{array}{l}\sin\theta\sin\beta_A + \\ \dfrac{\cos\beta_A}{1-\sin^2\theta\sin^2\alpha_1}\left(\sin 2\alpha_1\cos^2\theta + \dfrac{\cos^2\alpha_1 - \sin^2\alpha_1\cos^2\theta}{\tan(\alpha_1+\alpha_2)}\right)\end{array}\right\} \quad (4.22)$$

The mismatch is considered when l is replaced to $l_a\sin(\alpha_1+\alpha_2)$ in Equation (4.22).

Consequently, Equation (4.20) becomes

$$l_a = \left\{\frac{1}{1-\sin^2(\alpha_1+\alpha_2)S^2}\times\frac{(R_{o1}+R_{o2})^2}{2}\left[1-\cos(\arctan(Y/X))\right]\right\}^{\frac{1}{2}} \quad (4.23)$$

in which

$$S = \sin\theta \sin\beta_A + \frac{\cos\beta_A}{1-\sin^2\theta\sin^2\alpha_1}\left(\sin 2\alpha_1 \cos^2\theta + \frac{\cos^2\alpha_1 - \sin^2\alpha_1\cos^2\theta}{\tan(\alpha_1+\alpha_2)}\right) \qquad (4.24)$$

4.2.4 Results and discussion

Similar to Chapter 3, two models are considered in which $\alpha_1 = \alpha_2 = 45^o$ and $\alpha_1 = \alpha_2 = 30^o$. For convenience, they are called Models 3 and 4.

- **Radii**

Figures 4.7(a) and (b) show the radii R_{o1} and R_{o2} of Models 3 and 4 normalised with respect to the length l versus the deployment angle, θ, when m is 6. In Model 3, R_{o1} is greater than R_{o2} until θ is 73^o. In Model 4, R_{o1} is almost always smaller than R_{o2}.

The ratio of R_{o1} in the fully folded configuration to R_{o1} in the fully expanded configuration is denoted as R^*, which is 51.5% and 53.2% for Models 3 and 4.

Figure 4.8 shows the relationship between R^* and m for Model 3. For comparison, the result for the foldable cylindrical tube without helical folds is also shown. Both curves are similar, and R^* decreases as m increases.

Figures 4.9(a) and (b) show the photographs of card models of Model 3 in its fully folded and expanded configurations when m is 4 and 6, respectively. It can be seen that the model with larger m can be folded more compactly because its radius in the fully expanded configuration is larger.

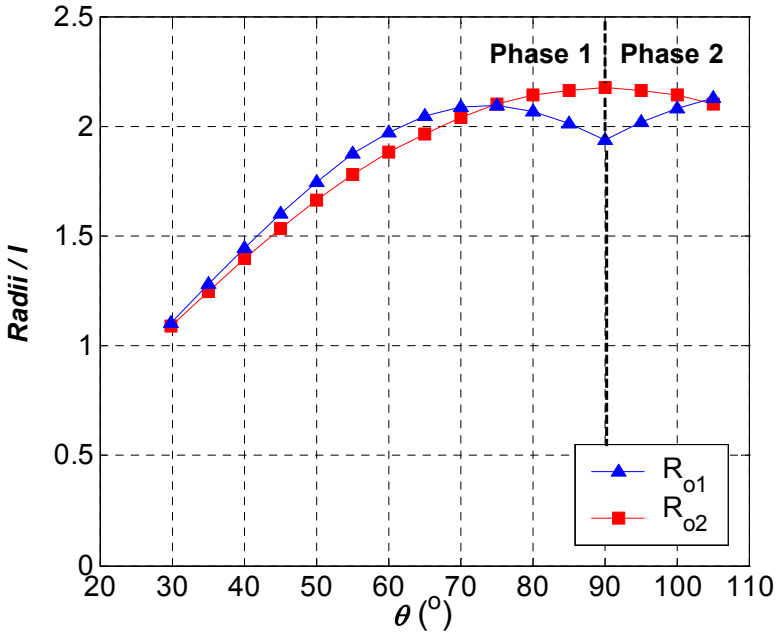

(a)

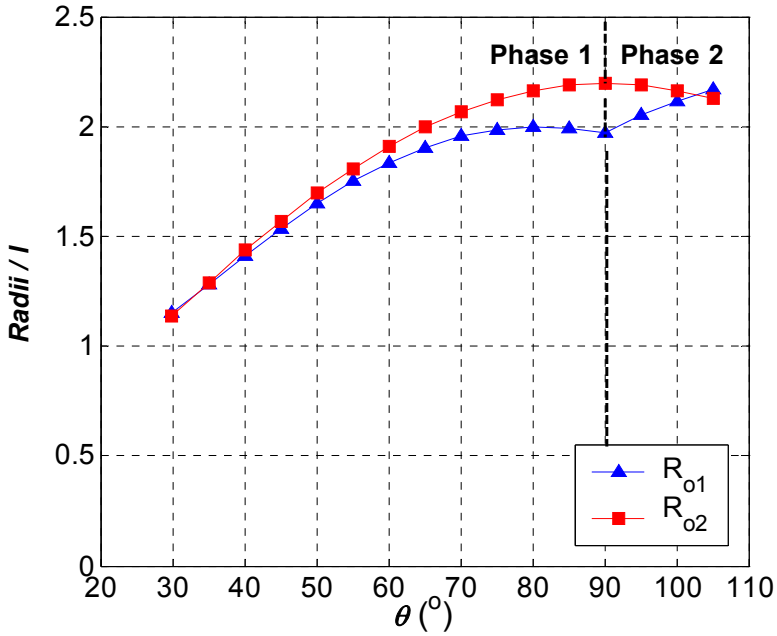

(b)

Figure 4.7 R_{o1} and R_{o2} vs. θ when m = 6. (a) Model 3 and (b) Model 4.

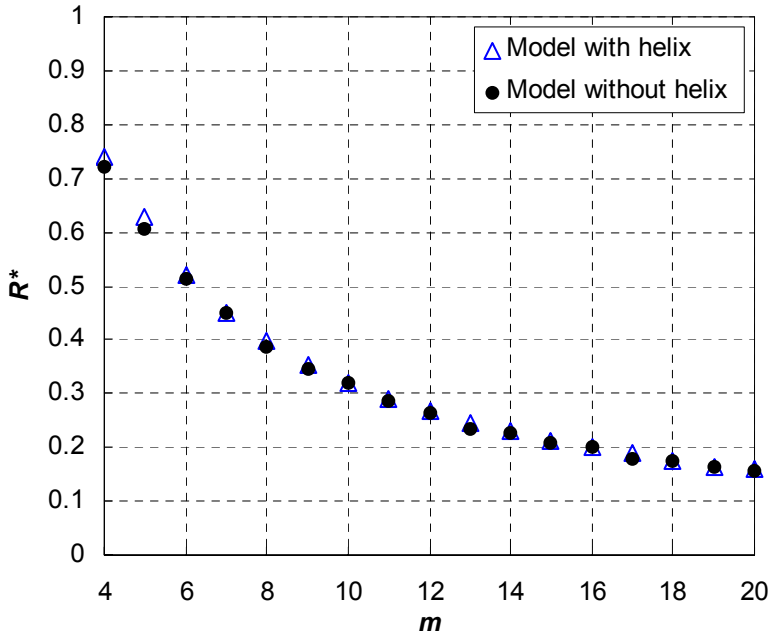

Figure 4.8 *R vs. *m* for Model 3.**

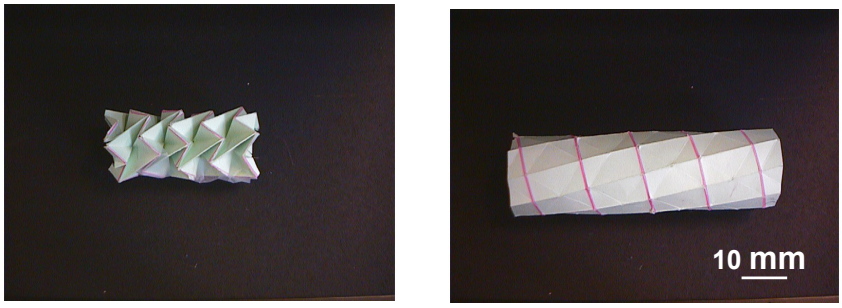

Fully folded **Fully expanded**

(a)

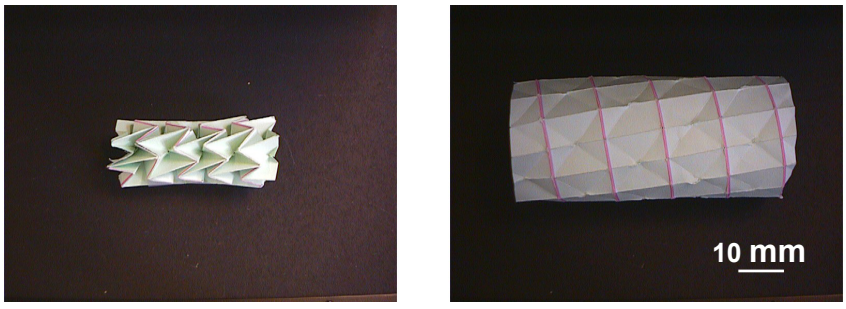

Fully folded **Fully expanded**

(b)

Figure 4.9 Photographs of Model 3 when (a) *m* = 4 and (b) *m* = 6.

- **Deformation**

Figures 4.10 shows a plot of l_a / l_o versus the deployment angle θ of Model 3 with helical folds for m of 6. For comparison, the results of the foldable cylindrical tube without helical folds are presented as well. It is noted that l_a becomes l_o and the structure becomes unstrained when $\theta = 73^o$ and $\theta = 103^o$. The deformations of the tube with helical folds are larger than those of the symmetric tube until $\theta = 73^o$ and then the difference between the foldable cylindrical tubes with and without helical folds become small.

Figures 4.11 (a) and (b) shows a plot of l_a / l_o versus the deployment angle θ with helical folds with m of 9 for Models 3 and 4, respectively. For Model 3, as m increases the deformations become smaller than the result shown in Figure 4.10. For Model 4, the deformation becomes very small until about $\theta = 55^o$ at the beginning of the first phase.

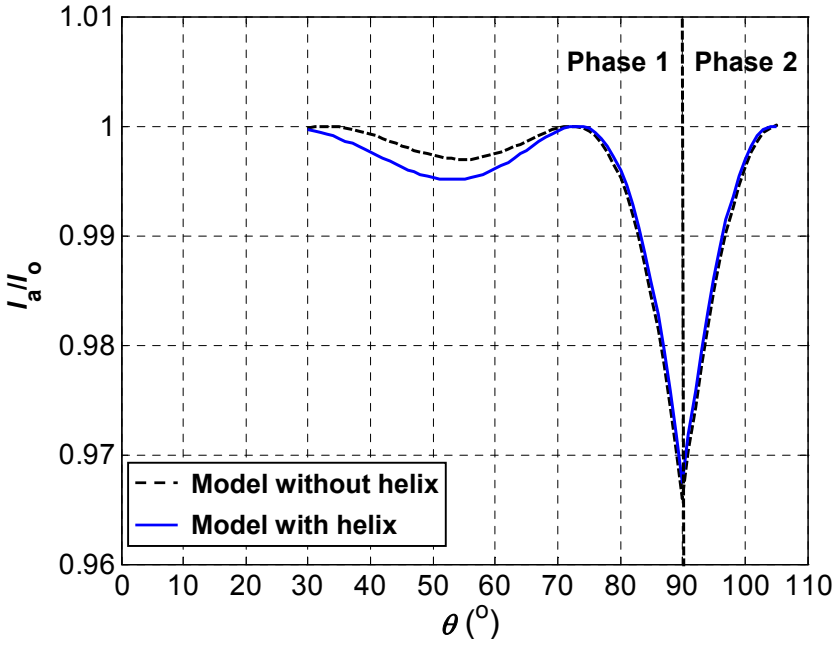

Figure 4.10 Plots of l_a/l_o vs. θ for Model 4 when m = 6. The data for similar models without helical folds are also included.

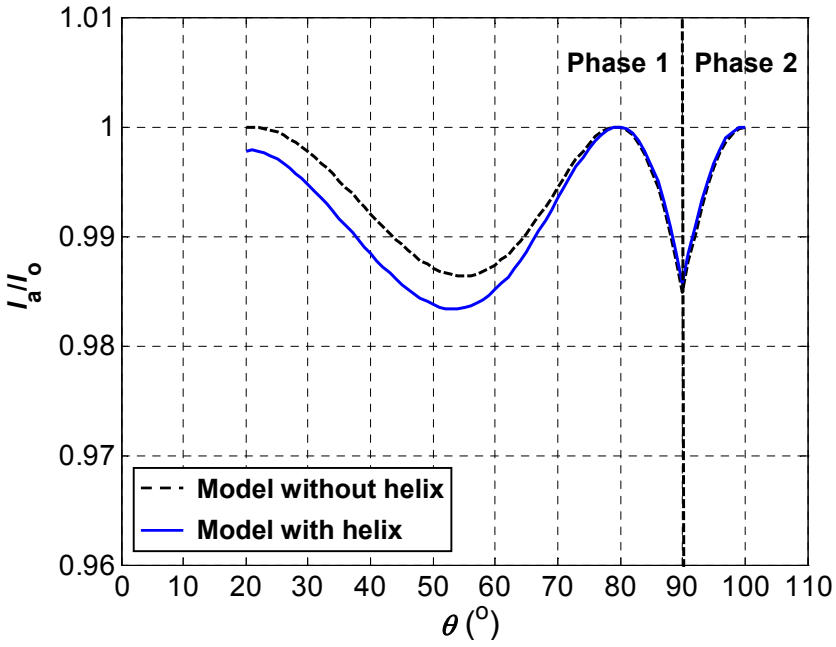

(a)

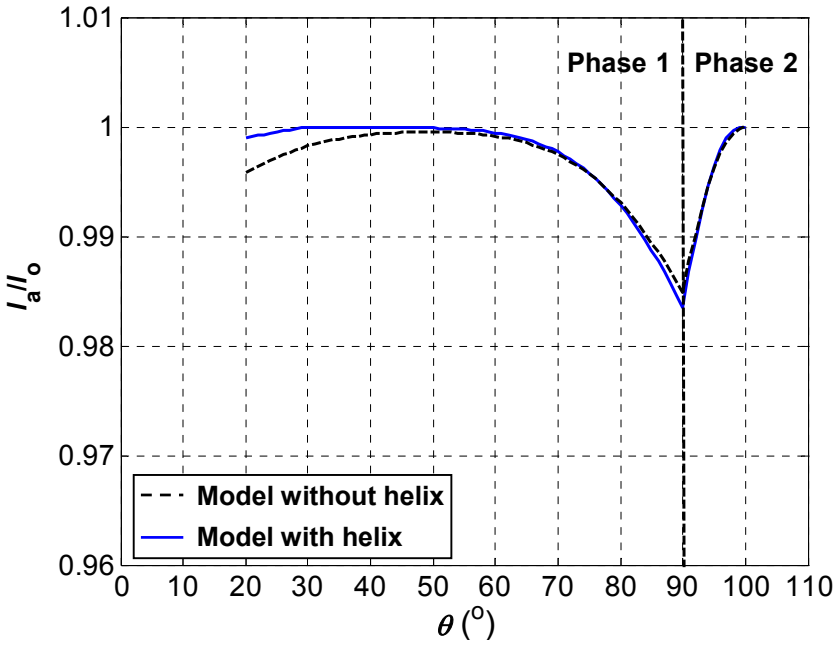

(b)

Figure 4.11 Plots of I_a/I vs. θ for foldable cylindrical tube with and without helical folds when m = 9, (a) Model 3 and (b) Model 4.
The data for similar models without helical folds are also included.

4.3 Buckling patterns

In Section 4.1, H_B type folds sustain an angle β_B to the horizontal line (see Figure 4.4). These are similar to the folds in the buckling failure pattern of a thin-walled tube under torsion. The forthcoming sections consider the buckling pattern to optimise the locations of the helical folds in order to make folding a naturally efficient process.

4.3.1 Analytical results

When a perfect thin-walled tube is under torsion, it reaches a threshold after which it loses stability and buckles. Figure 4.12(a) shows a schematic diagram of a buckled tube. The bucking patterns contains peak and valley folds around the surface of the tube, which represent a wave in the cross-sectional view of the buckled tube shown in Figure 4.12(b). The peak folds are called the buckling lines. The angle between the buckling line and the x axis, shown in Figure 4.12(c), is denoted as δ_b.

The torsional buckling of a cylindrical shell was first studied by Donnell (Donnell 1933; Donnell 1951; Timoshenko and Gere 1961; Calladine 1983). Assume that the tube has a finite length L whose ends are supported in such a way that the radial displacement w is equal to zero. The displacement w in the radial direction at y can be assumed as:

$$w = W \sin\left(m_b \theta - \frac{m_b n_b y}{r} \right) \sin\left(\frac{y\pi}{L} \right) \tag{4.25}$$

where r is radius of the tube. m_b is the total number of the buckling lines and $\frac{1}{n_b}$ represents the slope of the buckling lines. From Equation (4.25), it is noted that the radial displacement w is sinusoidal in a circumferential direction with the buckling wave

number m_b (b = 1, 2, 3, ⋯) at any cross-section positions where y is neither zero or L (see Figure 4.12b).

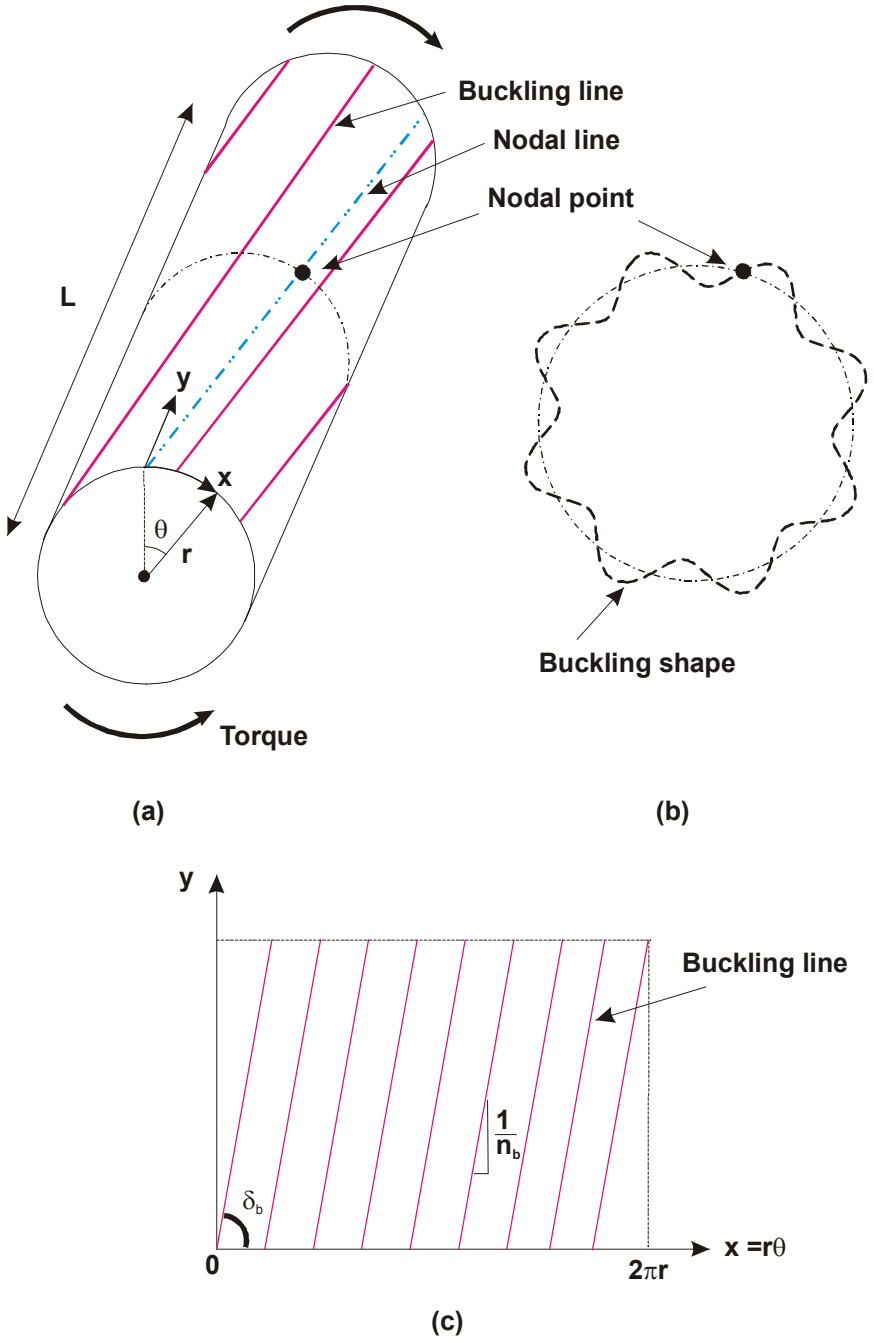

Figure 4.12 (a) Schematic diagram of a buckled tube, (b) cross-sectional view and (c) development of the tube with buckling lines.

From Equation (4.25), the nodal points where $w = 0$ (see Figure 4.12b) are formed when

$$m_b\theta - \frac{m_b n_b y}{r} = k\pi \qquad (k = 0, 1, 2, \cdots) \qquad (4.26)$$

Since $\theta = x/r$, Equation (4.26) can be rewritten

$$y = \frac{1}{n_b}x - \frac{rk\pi}{m_b n_b} \qquad (4.27)$$

which is the helical lines drawn on the cylindrical surface produced by connecting the nodal points in the longitudinal direction as shown in Figure 4.12(a). They are called nodal lines. From Equation (4.27) it is noted that $\frac{1}{n_b}$ represents the slope of the nodal lines.

Since the buckling lines are parallel to the nodal lines, the buckling angle δ_b is consequently obtained by

$$\delta_b = \tan^{-1}\frac{1}{n_b} \qquad (4.28)$$

Next, a buckling shear stress resultant N_{yx} is considered. Under pure torsion, the only non-zero stress resultant is N_{yx}. The total strain energy, which is involved in the distortion of the shell by both longitudinal stretching and circumferential bending, must be equal to the total energy supplied by the loading device. Thus, N_{yx} can be obtained using the energy method (Calladine 1983).

$$N_{yx} = \frac{r^2}{2n_b m_b^2}\left[\frac{m_b^4 Eth^2}{12r^4} + \left(\frac{n_b^4}{r^2} + \frac{6n^2\pi^2}{m_b^2 L^2} + \frac{\pi^4 r^2}{m_b^4 L^4}\right)Et\right] \tag{4.29}$$

where t is a thickness of the tube, and h is the effective thickness of the shell $h = t/\sqrt{1-\nu^2}$. E and ν are the Young's modulus and Poison's ratio, respectively. Equation (4.29) gives N_{yx} as a function of the two parameters n_b and m_b. Supposing that the value of m_b is fixed, N_{yx} can be minimised with respect to n_b, which is:

$$\frac{dN_{yx}}{dn_b} = \left[-\left(\frac{m_b^2 h^2}{24r^2} + \frac{r^4\pi^4}{2m_b^6 L^4}\right)\frac{1}{n_b^2} + \frac{3n_b^2}{2m_b^2} + \frac{3r^2\pi^2}{m_b^4 L^2}\right]Et = 0 \tag{4.30}$$

Using the following notations:

$$u = n_b^2,\ A = \frac{3}{2m_b^2},\ B = \frac{3r^2\pi^2}{m_b^4 L^2},\ C = -\left(\frac{m_b^2 h^2}{24r^2} + \frac{r^4\pi^4}{2m_b^6 L^4}\right) \tag{4.31}$$

Equation (4.30) becomes

$$Au^2 + Bu + C = 0 \tag{4.32}$$

from which n_b can be solved.

$$u = n_b^2 = \frac{-B \pm \sqrt{B^2 - 4AC}}{2A} \tag{4.33}$$

Table 4.2 shows the values of δ_b and N_{yx} for various m_b calculated using Equations (4.33), (4.28) and (4.29). The length L, radius r and thickness t of the tube are taken as 60 mm, 12.7 mm and 0.025 mm, respectively. The Young's modulus E and

Poison ratio ν are 72 GPa and 0.3. Obviously, the shear stress N_{yx} becomes the smallest when $m_b = 9$, which is the number of buckling lines presented when the tube loses stability under torsion.

Using this method, we are able to identify m_b and δ_b for tubes of various dimensions. When thickness and length of the tube change, the results are given in Table 4.3 in which r is always 12.7 mm. It has been found that as L increases, m_b decreases but δ_b increases. It is also found that as t increases, m_b decreases. Table 4.4 shows m_b and δ_b with respect to various values of r when L = 60 mm and t = 0.025 mm. It is found that as r increases, m_b increases but δ_b decreases. These results will be used to find the optimal folding pattern of the helical-type foldable cylinder in Section 4.7.

Table 4.2 Buckling angle and the shear stress for various m_b when L = 60 mm, r = 12.5 mm and t = 0.025 mm.

m_b	δ_b (°)	N_{yx} (N/m)
3	84.98	5800.54
4	86.05	1451.57
5	86.15	593.00
6	85.34	376.87
7	84.02	310.80
8	82.62	289.22
9	81.30	287.44
10	80.05	294.93
11	78.87	308.11

Table 4.3 m_b and δ_b for tubes of various length and thickness.

t = 0.025 (mm)			t = 0.08 (mm)		
L (mm)	m_b	δ_b (°)	L (mm)	m_b	δ_b (°)
60	9	81.30	60	7	77.93
90	7	83.33	90	5	81.75
120	6	84.30	120	5	81.29
160	5	85.33	160	4	83.20
200	5	85.22	200	4	82.95

Table 4.4 m_b and δ_b for tubes of various r when L = 60 mm and t = 0.025 mm.

r (mm)	m_b	δ_b (°)
6.4	5	83.46
9.5	7	82.43
12.7	9	81.30
15.9	10	81.73
19.1	12	80.79

4.3.2 Physical modelling

To verify the analytical results, a number of model tubes are prefabricated using cardboard. Figure 4.13 shows the schematic diagram of such a cylindrical tube. According to the results of Donnell's formula shown in Table 4.2, the buckling pattern consists of m_b = 8 folds at $\delta_b = 82.62^o$ when L = 60 mm, t = 0.025 mm. Three models are created in which folds are scored at $\delta_b = 82.62^o$, which is the same as the buckling angle, 60^o and 88^o. The length of the models is 60 mm and the number of the folds is 8. Wood

bars are placed at each end of the tube to support the cardboard, and then the tubes are twisted by applying torques at both ends using hand motions.

Figures 4.14(a)-(c) shows photographs the three models taken after the twisting tests. When δ_b is the same as the bucking pattern ($\delta_b = 82.62^o$), the tube buckles and is twisted easily. When δ is larger than the buckling pattern ($\delta_b = 88^o$), the tube does not buckled at all. But it is damaged at one point. When δ_b is smaller than the buckling pattern ($\delta_b = 60^o$), only one end of the tube buckles. Although the boundary conditions of the cardboard models may not fit exactly to the assumption of the analyses, these simple tests indicates that the tube where the folds are created along the same angles as the natural buckling pattern ($\delta_b = 82.62^o$) is more easily buckled than the other tubes. Therefore, the physical models confirm the results of the analysis.

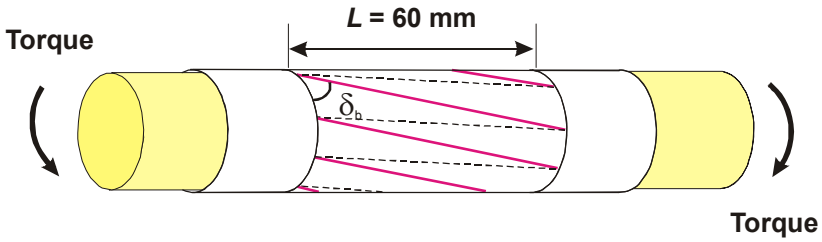

Figure 4.13 Schematic diagram of cylindrical tube with prefabricated folds.

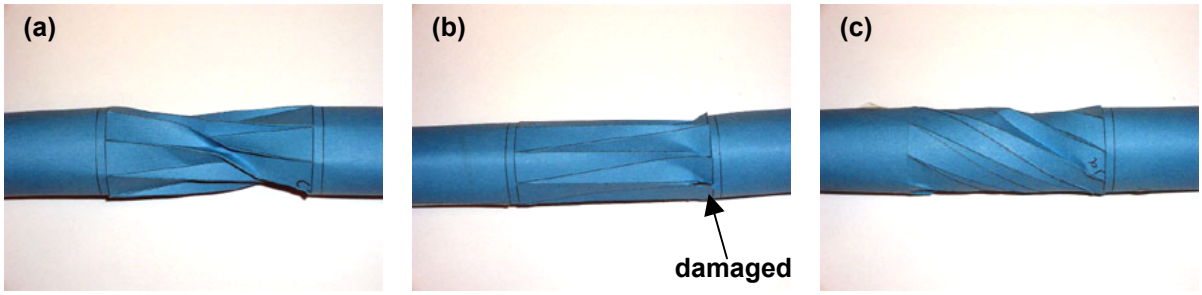

Figure 4.14 Twisted tubes with δ_b of (a) 82.62°, (b) 88° and (c) 60°.

4.4 Optimum folding patterns

In order to enable a helical-type cylindrical tube to be folded up easily, an optimum pattern of the helical folds needs to be found. Based on the previous sections, it is obvious that utilisation of the buckling patterns will provide a folding pattern which can be folded using the least energy consumption.

In the geometric analysis, the helical folds are determined by β_B, which is the angle between the H_B type helical folds and horizontal base line, and the element number m. The analysis does not consider the effect of the length, diameter and thickness of the tube. On the other hand, the buckling patterns are determined by the angle δ_b and m_b. They are related to the length and thickness of the tube. The values of δ_b and m_b are compared with the values of β_B in the fully expanded configuration of the tube and m, respectively. From the comparison, the suitable values of m and the design of the element, such as α_1 and α_2, for the helical origami stent graft are found.

Now consider a set of curves shown in Figure 4.15 for various α_1. They are obtained from the geometric analysis using Equation (4.2), in which it is assumed that $\alpha_2 = \alpha_1$. Each point along the curves represents a geometrically feasible design. If we also consider the length, radius and thickness of the tube, the buckling analysis indicates that δ_b = 81.3° and m_b = 9 when L = 60 mm, r = 12.7 mm and $t = 0.025$ mm, (see Table 4.3). The corresponding point is marked in Figure 4.15. It is obvious that the curve closest to the point is that of $\alpha_1 = \alpha_2 = 30°$. Therefore, for example, if a helical stent graft has $L = 60$ mm, $r = 12.7$ mm and $t = 0.025$ mm, the element with $\alpha_1 = 30^o$ and $m = 9$ should be used to achieve the optimal helical folding pattern. As shown in Figure 4.15, as L increases, the buckling pattern m_b decreases and δ increases. Therefore for a stent graft with larger values of L, m should also decrease. However, as shown in Figure 4.8 a smaller value for m led to a less complete compaction of the stent graft, which is less suitable for the stent design. Furthermore if L becomes longer than 160 mm, the calculated values of m and β_B, and also α_1 do not match the buckling pattern.

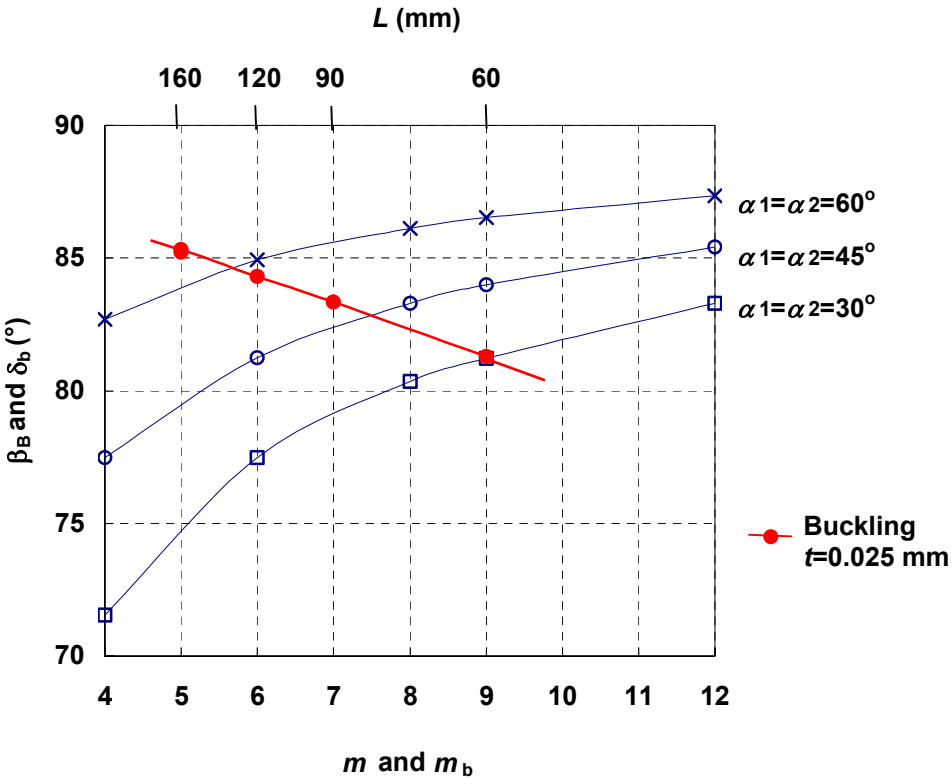

Figure 4.15 Geometric relationship of β_B vs. m of the helical-type foldable cylinders and the relationship of δ_b and m_b of buckling pattern for various L when r = 12.7 mm and t = 0.025 mm.

Figure 4.16 shows the buckling patterns δ and m_b for various radii when t = 0.025 mm and L = 60 mm which can be obtained from Table 4.4 and are shown as solid square symbols. The optimum helical folding pattern for the helical stent graft can be designed by matching those results. However, as shown in Figure 4.16 as radii decrease, the buckling pattern m_b decreases and δ increases, which will conflict results of m and β_B, and also α_1.

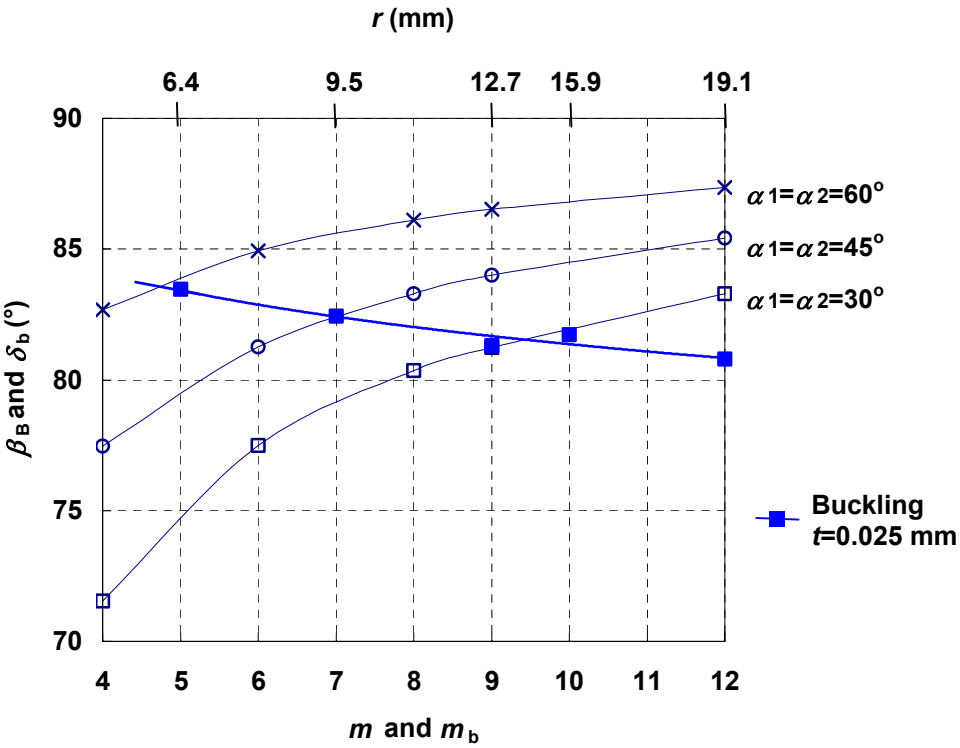

Figure 4.16 Geometric relationship of β_B vs. m of the helical-type foldable cylinders and the relationship of δ_b and m_b of buckling pattern for various L when L= 60 mm and t = 0.025 mm.

4.4 Conclusions

This chapter has presented a new origami stent graft with helical folds. The chapter started with discussions regarding geometric design. Helical folds have been introduced by adjusting the joining position of the two edges of a sheet that had been symmetrically jointed in Chapter 3. The main advantage of the helical folds over the symmetric ones is that they improve the radial strength of the stent graft and ease of the deployment process by synchronizing the deployment of each element.

Geometric properties such as the helical angle and the radius of the helical origami stent grafts during deployment have been calculated. It was found that a larger value for the element number m in one complete circumference of a helix led to a more compact folding of the stent graft with helical folds

The optimum locations for the helical folds are identified by considering both the geometric aspects of folding and the buckling patterns of a thin-walled tube under torsion, which have been found using analytical solutions. Physical models of the tube with prefabricated folds have been produced and then twisted by applying torques at both ends. The models confirm that the tube with the helical folds resembling buckling patterns could be folded more easily under torsion, and with less material damage to the cylinder. Recommendations about helical folds are given for the design of a stent graft.

CHAPTER 5

NUMERICAL ANALYSIS OF ORIGAMI STENT GRAFT

In Chapter 3, it is found that when the elements of the origami stent graft are connected in a longitudinal direction, there is a geometric mismatch between the elements. Therefore, the folds of the stent graft are deformed and the strain builds up during deployment. In this chapter further analysis is carried out in order to understand the strain level and overall deformation of the stent graft during deployment and to verify analytical formulation. The deformed shape of a thin cylindrical tube without any folds is also identified and is compared with the pattern of folds for the origami stent graft. Since the geometry of the stent graft is complicated, they can only be analysed numerically using the finite element method (FEM). We assume that the stent graft is made of shape memory alloy (SMA) because it is the material of which current stents and stent grafts are made. For the sake of simplicity, the material nonlinearity is not considered in this chapter, and only the geometrical nonlinearity is taken into account.

5.1 Strains within a fold

In this section, we examine how the strain within a fold varies with respect to the fold width when the stent graft is being folded. The data will be useful to make decisions regarding the groove width.

5.1.1 Origami stent FE model

The FE model of the origami stent graft is constructed as follows. The stent graft is a cylindrical tube and consists of units[3] with folds as shown in Figure 5.1(a). The diameter of the tube is 25.46 mm, which is similar to the actual size of the oesophageal and aortal stent grafts. The pattern of folds is the same one described in Chapter 3, where the angles of the unit: $\alpha_1 = \alpha_2 = 45^o$. Since the pattern of the folds is rotationally symmetric, in this section, to simplify the analysis, only a quarter of the model in the circumferential direction is created shown as a dark green colour in Figure 5.1(a). There are two square units and the size of the each unit is 10 mm x 10 mm.

In order to produce the designed grooves in the model, 3D solid elements are used instead of shell elements because the shell element is not able to simulate the required groove shape shown in Figure 5.1(b). The model can be divided into three layers in the radial direction and their thicknesses from the outer layer are 0.04 mm, 0.01 mm and 0.04 mm. As shown in Figure 5.1(c) and (e), the grooves for the diagonal and rectangle folds are produced in the inner and outer layers of the model. The width of the diagonal groove in the inner layer is 0.442 mm. The outer layer has grooves of 0.625 mm width, and the width of the mid groove varies to 0.3125, 1.25 and 2.5 mm. In the inner layer shown in Figure 5.3(c), 6 - node solid elements with dimensions of 0.3125 mm x 0.3125 mm x 0.04 mm in size are used. 8 - node solid elements are used for the middle and outside layers shown in Figures 5.3(d) and (e). The sizes of the elements in the middle and outer layer are 0.3125 mm x 0.3125 mm x 0.01 mm and 0.3125 mm x 0.3125 mm x 0.04 mm, respectively.

The mesh of the model is generated by codes written in MATLAB (version 6). The same mesh density is used for the entire model. Therefore, the total number of the elements is quite large, which is not ideal for the FEM model. A minimum number for the elements has been identified in the next section, which gives reduced element

[3] In the other chapters, a unit is termed as an element. To avoid confusion with elements of the FEM, we use term unit instead in this chapter.

numbers of 7632, 7440, 7056 and 6288 for the mid groove widths of 0.3125, 0.625, 1.25 and 2.5 mm, respectively.

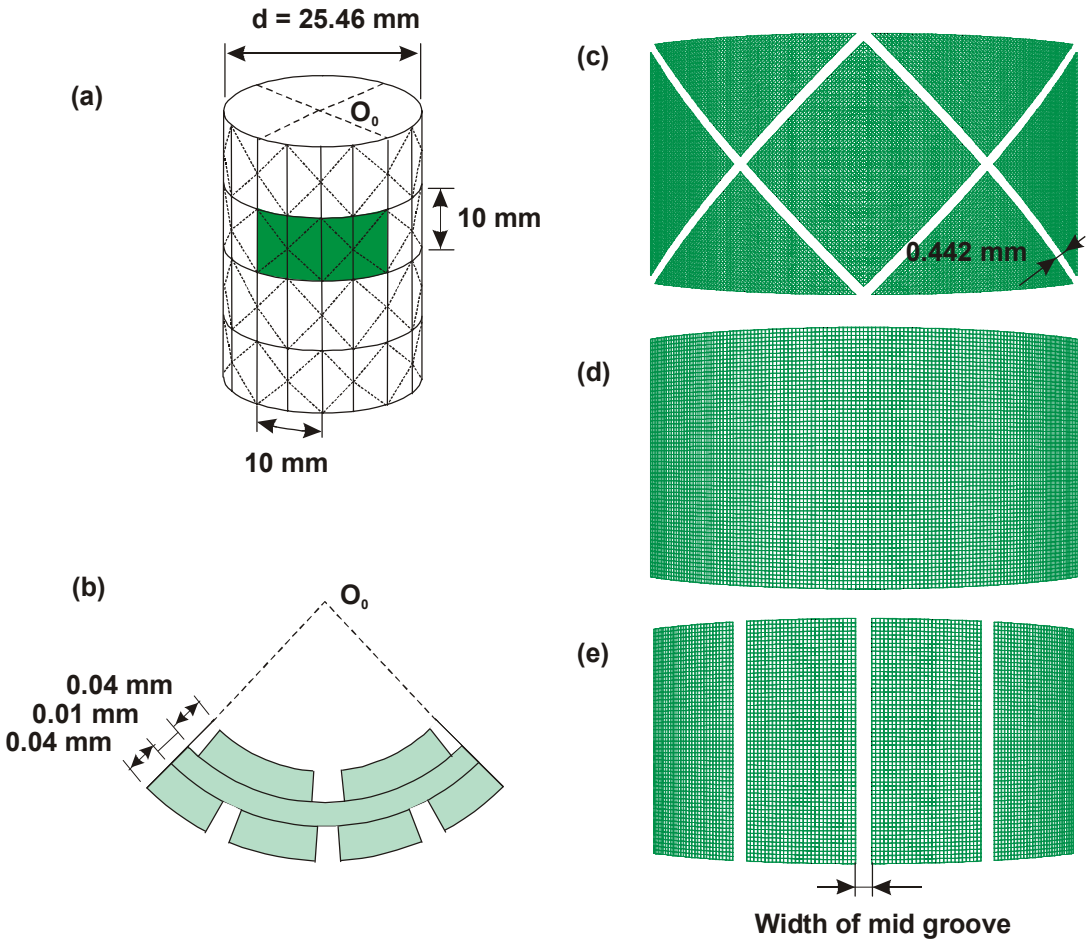

Figure 5.1 (a) Perspective view of a stent graft model; (b) cross section pair of adjustment units; (c) inner, (d) middle and (e) outer layers of the units.

The boundary conditions are shown in Figure 5.2. In a cylindrical coordinate system, both side edges of the units are fixed in the circumferential direction, and the upper edge is fixed vertically. To simulate the folding process, the 8 mm prescribed displacements are applied at the centre of the each unit pointing inwards in the radial direction, shown as red arrows in Figure 5.2(b). The use of prescribed displacements make it easy to achieve the desired deformed shape of the stent graft. Outwardly directed radial forces of 50 N are applied at the top and bottom of the units as shown by blue arrows in Figure 5.2(b). These simulate the forces during folding of the stent graft. When it is folded, the centre of the unit is pushed inwards and both edges at the top and bottom are pushed outwards.

An ABAQUS stabilisation algorithm has been applied to the FE analysis of the buckling model. It is assumed that the stent graft is made of SMA with the Young's modulus E = 60 GPa, and Poisson's ratio ν = 0.3.

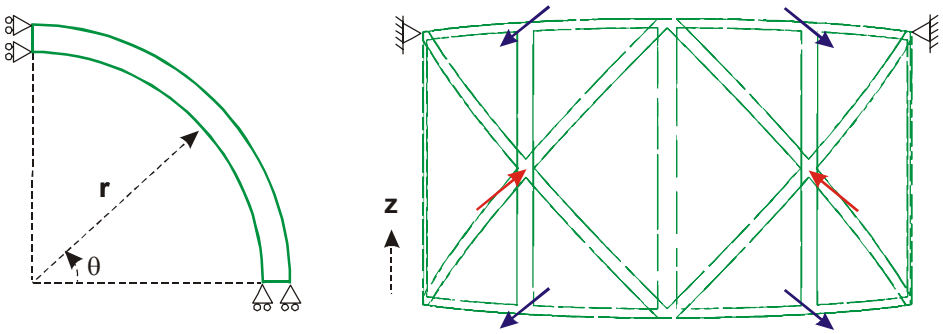

Figure 5.2 Boundary condition. (a) End and (b) perspective views

5.1.2 Performance of the element

Before carrying out FE analysis of the model, the suitability of the solid element for the stent model is examined. In reality the thickness of the stent graft is very small in comparison with its diameter and length. This results in a restriction on the sizes of the employed solid element. For numerical stability the ratio among the side length of the solid element cannot be too large or small. Hence, to achieve the same mesh density over the whole model, a huge number of elements have to be used. As a consequence, the computational cost will be very high. To reduce the computational cost, a higher ratio should be used for the stent model. Therefore, the minimum number of elements needed to simulate a groove must be found.

A simple model of a beam with a groove at the centre is created, and shown in Figure 5.3. The length and width of the beam are 33.6 mm and 2.40 mm. The depth of the groove is 0.096 mm but it is halved at the centre of the beam. The groove width is 1.2 mm.

The beam is modelled using 8 - node solid elements. The numbers of elements at the groove in the x, y and z directions are denoted as n_x, n_y and n_z, respectively. Because the dimensions of the groove are predetermined, higher numbers of elements lead to smaller elements. For example, when $n_x = 2$, $n_y = 8$ and $n_z = 4$, the side lengths of an element in the x, y and z directions are 0.6 mm, 0.3 mm and 0.012 mm with the corresponding ratio of 50:25:1. Table 5.1 summarises the various numbers examined.

The beam is simply supported at both ends and the loads are applied through prescribed displacements, -10 mm, in the z direction at the positions of 9.6 mm from each end.

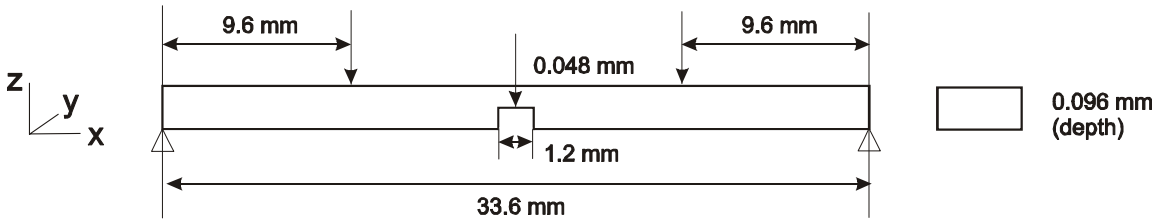

Figure 5.3 (a) A beam with a groove at the centre.

Table 5.1 The number and size of the elements of the models when groove width is 1.2 mm.

n_x	n_y	n_z	**x** x **y** x **z** (mm)
2	8	4	**0.6** x 0.3 x 0.012
4	8	**2**	0.3 x 0.3 x **0.024**
4	8	**4**	0.3 x 0.3 x **0.012**
4	8	**8**	0.3 x 0.3 x **0.006**
8	8	4	**0.15** x 0.3 x 0.012
10	8	4	**0.1** x 0.3 x 0.012

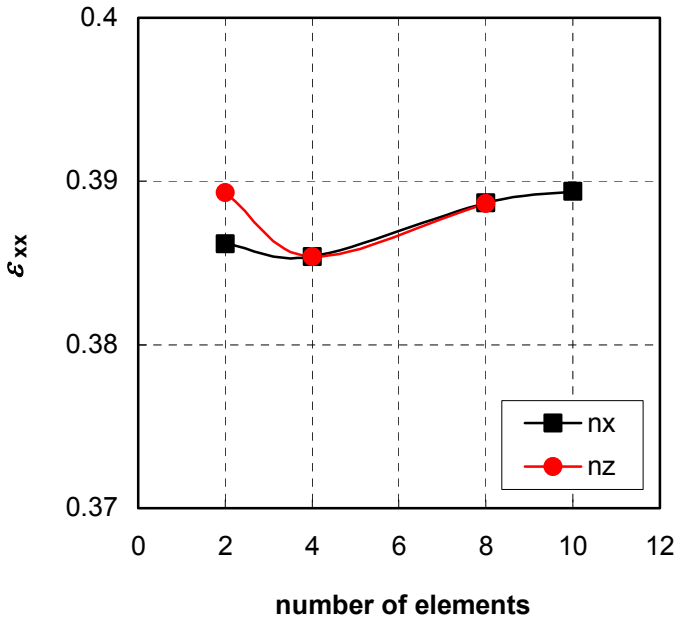

Figure 5.4 Number of elements of n_x or n_z vs. strain at the groove.

Figure 5.4 shows the results of strains ε_{xx} at the centre of the beam versus n_x or n_z. The maximum differences of ε_{xx} between the two analyses are 0.0040, corresponding to an error of 1%. It can be seen that the results are not sensitive with the change of the ratios between element side lengths. Therefore, it is possible to use fewer elements in the numerical simulation.

5.1.3 Results

Figure 5.4(a) shows the deformed shape of a pair of adjacent units when the stent graft is folded. Both valley and hill creases are visible. The position of the nodes between C_1 and C_2 is denoted as n_A (1, 2,⋯and 32), see Figure 5.4(b). The diagram of the circumferential strain $\varepsilon_{\theta\theta}$ is given in Figure 5.5. The strain becomes smaller as the width of the groove becomes wider. It is noted that the values of the strain become almost identical when the widths of the groove are 1.2 mm and 2.4 mm. Thus increasing groove width does not necessarily reduce strain.

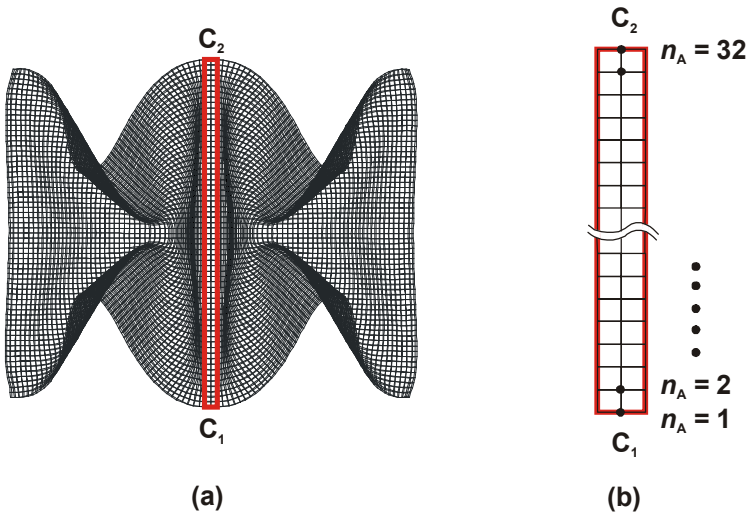

Figure 5.4 (a) Middle layer of the model in the folded configuration and (b) the position n_A of the centre fold between C_1 - C_2.

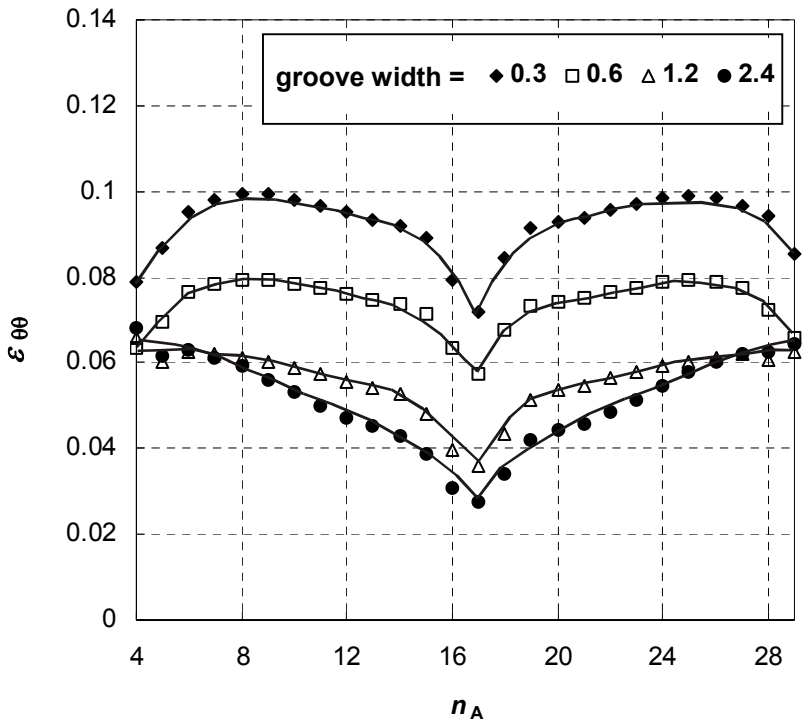

Figure 5.5 Circumferential strain $\varepsilon_{\theta\theta}$ vs. positions of nods n_A for different groove width.

5.2 Deformed shape of a thin cylindrical tube

In this section the deformed shape of a thin cylindrical tube without any folds is identified. The result will be compared with the pattern of folds for the origami stent graft.

Figure 5.6 shows a quarter section of the 0.01mm thick cylindrical tube model. The diameter of the tube is 25.46 mm. The boundary conditions in the cylindrical coordinate system are the same as those applied to the model presented previously. In the numerical analysis, a set of forces and displacement are applied, which simulate the folding process of the stent graft, see Figure 5.6(b). All of these forces are in radial directions. The prescribed displacements are applied at the centre of the each unit. These are 12 mm pointing inwards in the radial direction, and are shown by red arrows. The loads of 50 N outward the radial direction are given at the top and bottom of the unit, and are shown by blue arrows. The material is same as that used in the last section.

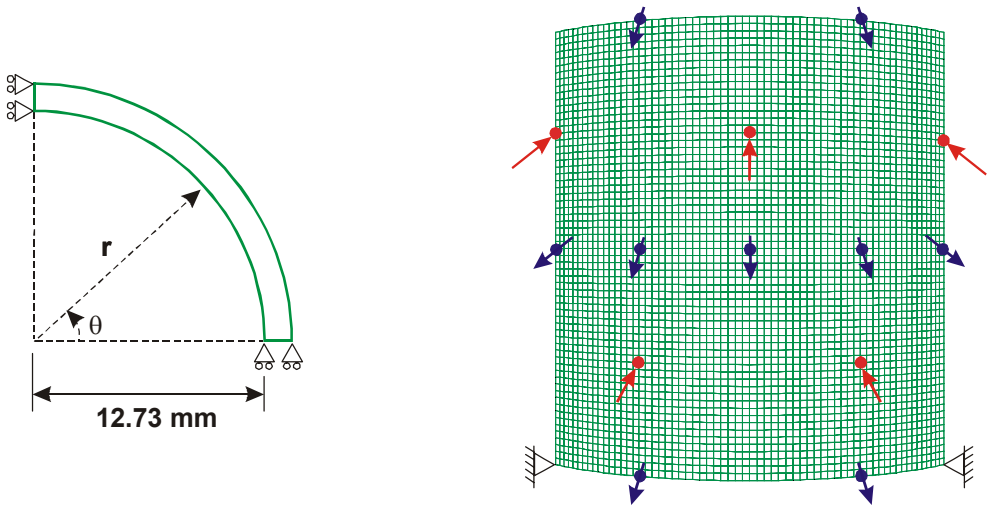

Figure 5.6 Boundary conditions of thin-tube model under a certain condition.
(a) End and (b) perspective views of the model.
Displacement of 12 mm into and 50 N outward the radial direction.

Figure 5.7(a) shows the deformed cylindrical tube. Hill and valley creases appeared on the surface of the tube and are represented by red and blue lines. The patterns of the folds are redrawn in a two-dimensional representation of the cylindrical surface as shown in Figure 5.7(b). It is found that the pattern of folds is the same as that of the foldable cylindrical tube described in Chapter 3. Therefore, if a cylindrical tube has prefabricated additional grooves for these natural folds, it will assist the folding process. Alternatively, this deformed shape can also be achieved if they are applied using mechanical methods, e.g., the application of a press. By this latter method, the cylindrical tube could be folded into the desired pattern without using folds.

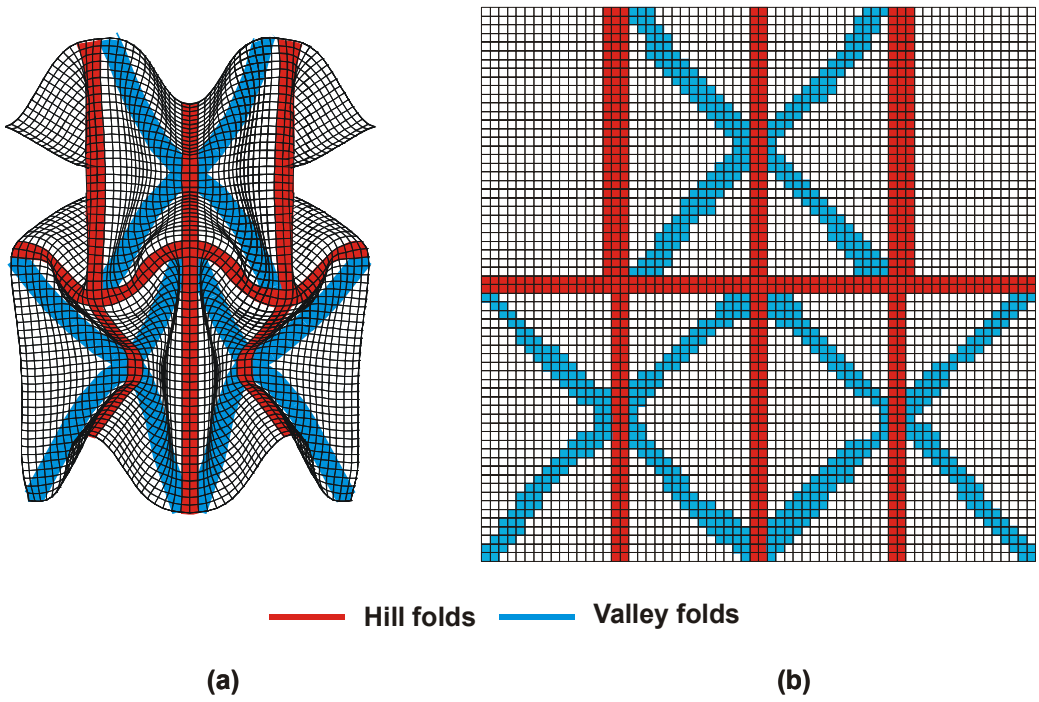

Figure 5.7 (a) Folding shape in 3D and (b) folding pattern in 2D.

5.3 Deformation of the fold

As described in Chapter 3, there is geometric mismatch among units. A simple geometric evaluation was accomplished. Now we employ the FEM to gain a more precise description of the length condition of folds. The results will be compared with the results calculated geometrically in Chapter 3.

The stent graft model is shown in Figure 5.8(a). The distance of the fold between nodes E_2A_1 and F_2B_1 is denoted l_a and calculated as follows. Firstly, the nodes E_2A_1 and F_2B_1 are defined in the cylindrical coordinates system as (R_{E2A1} , δ_{E2A1} , Z_{E2A1}) and (R_{F2B1} , δ_{F2B1} , Z_{F2B1}), respectively. Therefore, l_a is calculated by

$$l_a = \left[\left(R_{E2A1} \cos \delta_{E2A1} - R_{F2B1} \cos \delta_{F2B1} \right)^2 + \left(R_{E2A1} \sin \delta_{E2A1} - R_{F2B1} \sin \delta_{F2B1} \right)^2 + \left(Z_{E2A1} - Z_{F2B1} \right)^2 \right]^{\frac{1}{2}} \quad (5.1)$$

All variables in Equation (5.1) can be determined from the FE analysis. The FE model is similar to that in Section 5.1 except that the model has two rows of units instead of one (Figure 5.8). The widths of the grooves in the inside and outside layers are 0.442 mm and 0.625 mm, respectively. The total number of elements is 14752.

In the cylindrical coordinate system, the sides of the model are fixed in the circumferential direction and the upper edge is fixed vertically. The prescribed displacements of 12 mm inwards in the radial direction on the unfolded model are applied at the centre of the each unit, as shown in Figure 5.8(b), and the loads of 50 N outwards in the radial direction are applied at the top and bottom of the unit. The material used is, again, has the same properties as those previously used.

During the analysis, the inner radius R_i, which is the distance between node K and O_0 at the central axis, is also calculated.

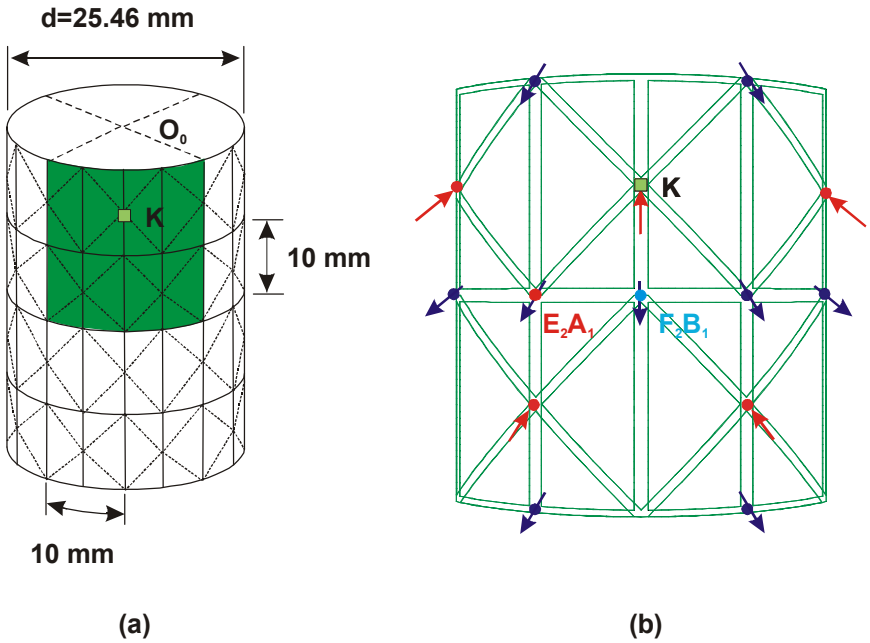

Figure 5.8 (a) The FE model with two rows of a total four units. (b) Loadings.

Figure 5.9 shows a series of images during the folding process starting with Figure 5.9(a) in its unfolded configuration. Valley and hill creases become visible from Figure 5.9(c) onwards. In Figure 5.9(h) the model is folded compactly where the control displacement of -12 mm at node K is achieved (i.e. -12 mm in the radial direction from the position of the node in the unfolded model). The inner radius R_i becomes 0.692 mm.

R_i is taken as the controlling parameter for the folding process. Figure 5.10 shows the radii of nodes E_2A_1 and F_2B_1 versus R_i. For comparison, $(R_{o1}+R_{o2})/2$ the radius of the nodes E_2A_1 and F_2B_1 calculated analytically in Chapter 3 is also shown. It is found that the results are almost identical. Figure 5.11 shows the difference between $Z_{E2A1} - Z_{F2B1}$ versus R_i. The FEM result is smaller than those achieved by the geometrical analysis. It is probably because the fold between the nodes E_2A_1 and F_2B_1 is curved during numerical analysis, while it kinks in the geometric analysis. Figure 5.12 shows a plot of l_a / l_o versus R_i. These results are clearly different from the result calculated by the

geometric analysis. The difference is around 18% when the tube is fully folded, to 1% when it is expanded.

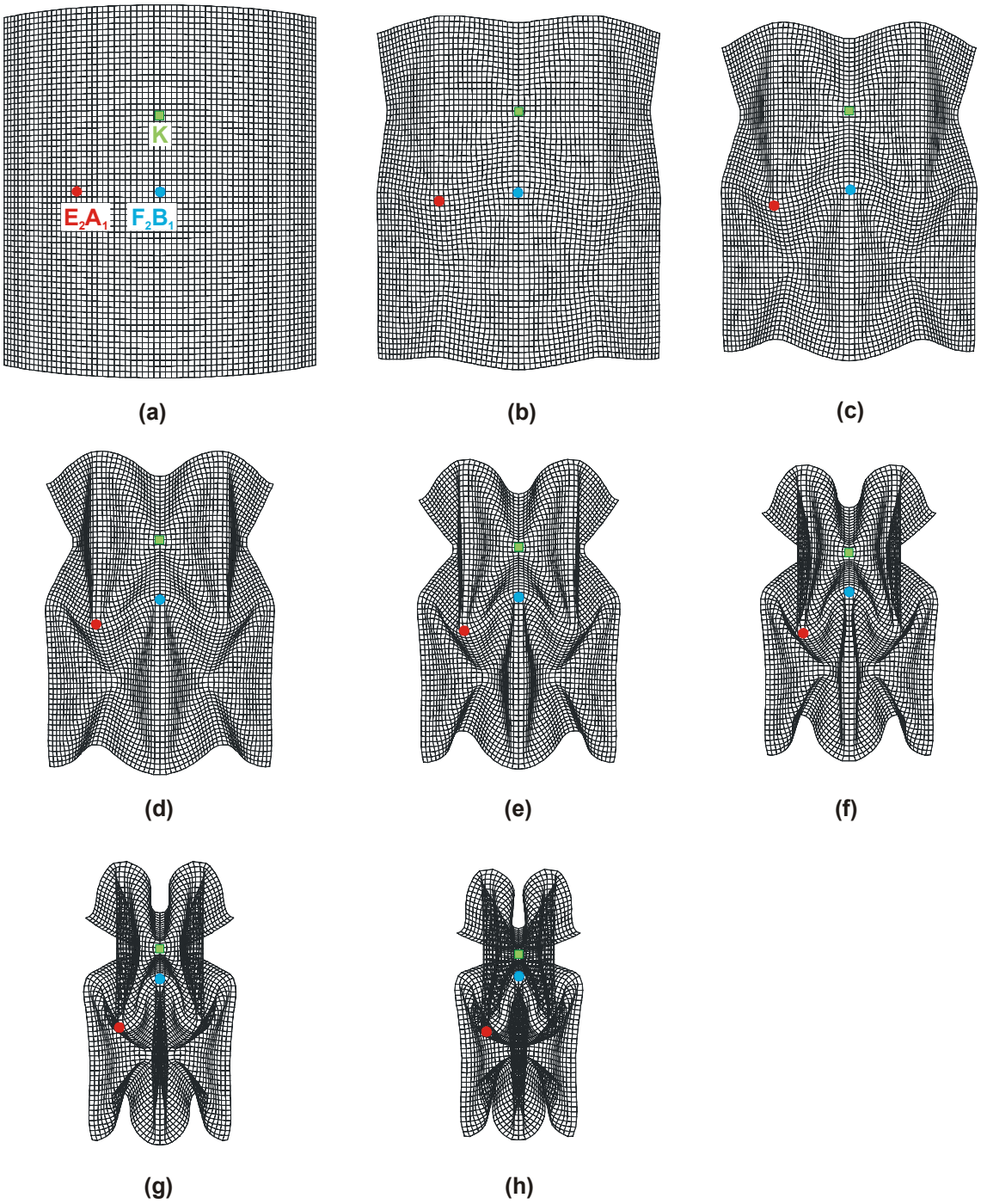

Figure 5.9 Series of photos showing the folding process. The controlling radius R_i = (a) 12.69, (b) 11.92, (c) 9.807, (d) 8.452, (e) 7.102, (f) 5.752, (g) 4.042 and (h) 0.692 mm.

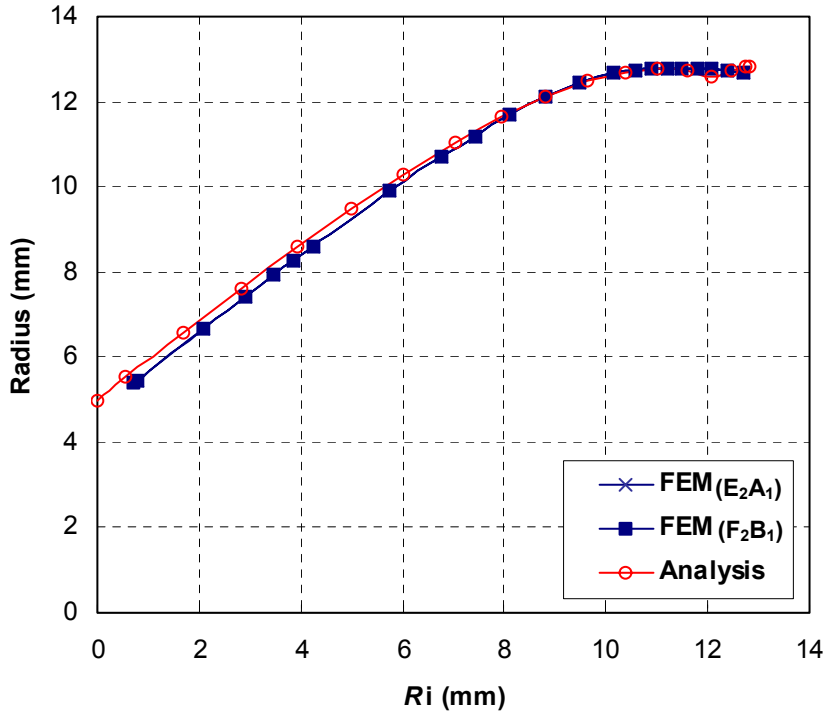

Figure 5.10 Radii vs. R_i.

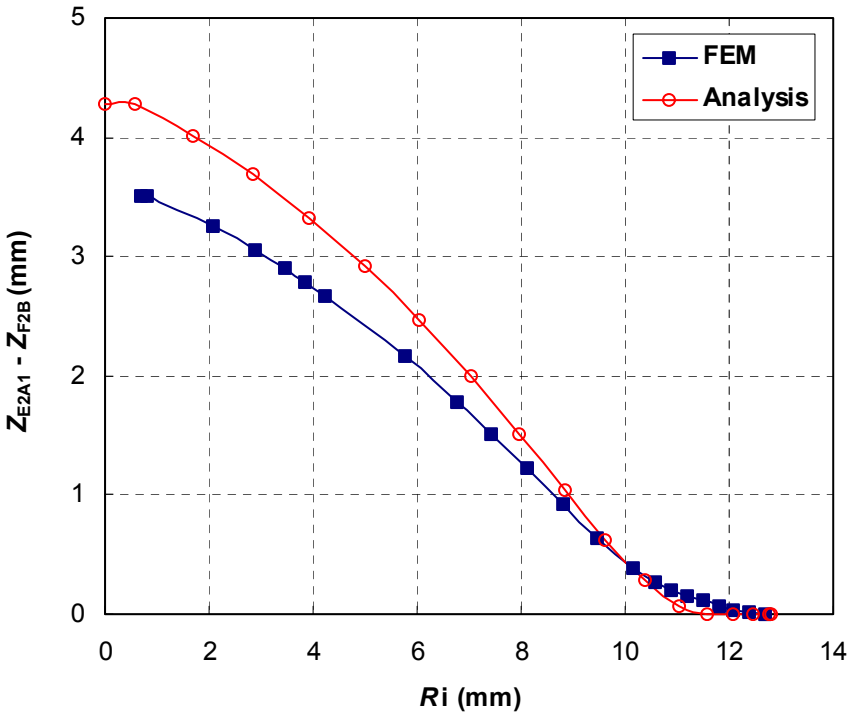

Figure 5.11 Z_{E2A1} - Z_{F2B} vs. R_i.

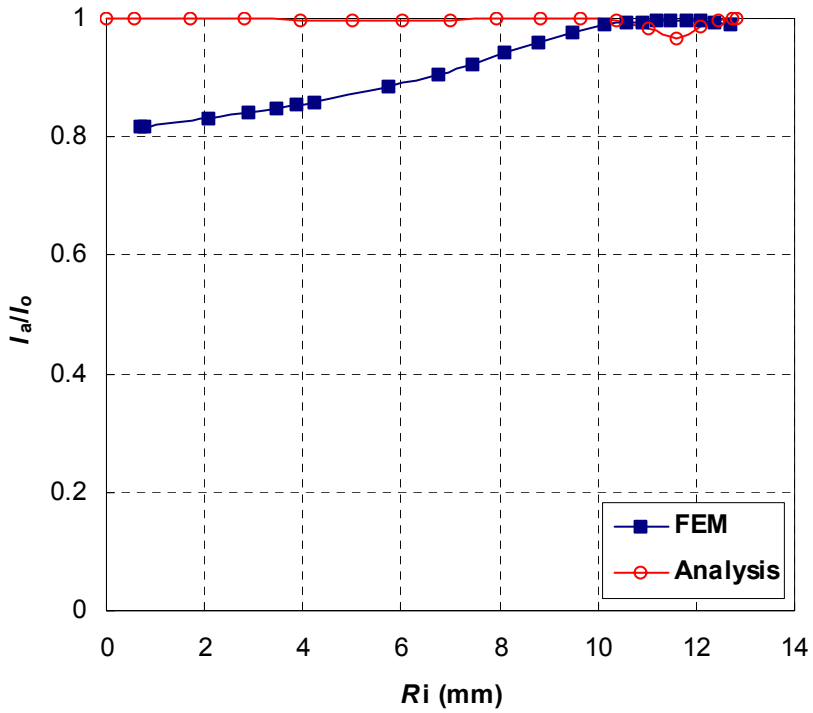

Figure 5.12 l_a/l_o vs. R_i.

5.4 Conclusions

In this chapter FE analysis has been carried out to understand the strain of the fold with respect to the different widths of the fold. Also, the pattern of the deformed thin cylindrical tube without any folds has been analysed. The main results are summarised as follows.

It is found that the circumferential strain becomes smaller as the width of the groove increases. However, the reduction of the strain becomes less obvious when the width is larger than 1.2 mm.

The geometry of the deformed pattern resembled the pattern of the folds that was found in the foldable cylindrical tube described in Chapter 3. The geometry of the deformed pattern resembles the pattern of the folds of the designed foldable cylindrical tube. Therefore, the stent graft can be folded into the desirable shape easily if the groove

is produced. By the press method, the cylindrical tube could be folded into the desired pattern without using folds.

FE analysis is also used to identify the accuracy of the geometric analysis in the presence of mismatch. It is found that the geometric analysis and FEM techniques strongly agree with one another with regard to deployment radius, but weakly agree in assessing overall length.

CHAPTER 6

MANUFACTURING ORIGAMI STENT GRAFT

This chapter deals with the manufacture of the novel origami stent graft based on geometric parameters derived earlier in this dissertation. At present most existing stents and stent grafts are made from stainless steel and TiNi shape memory alloy (SMA). The same materials will be used to produce the new stent graft here. Stents currently in production use these materials in a wire form. Rather than the wire form this chapter describes the use of these materials in sheet form, which can be easily manufactured into a tubular shape for the stent graft. A photochemical etching technique was used to engrave folds into the materials.

The main advantage of using SMA sheet is that it is possible to make a stent graft which can self-expand to the desired shape at body temperature without the use of an expansion tool. However, SMA sheet is a relatively new material and the applications are still limited. Therefore, processing techniques including photochemical etching and heat-treatment of SMA sheet need to be established.

Section 6.1 explains how a stainless steel sheet can be used to make the novel origami stent graft. Section 6.2 deals with the etching and heat-treatment processing of the TiNi SMA sheet. Sections 6.3 and 6.4 demonstrate models of the new stent grafts produced with Ti-rich and Ni-rich TiNi SMA sheets as well as illustrations of the self-expansion of the stent grafts.

The models produced here are the same size as standard oesophageal and aortal stent grafts.

6.1 Foldable cylindrical tubes using a stainless steel sheet

The stainless steel sheet 316L is used to make the stent graft. The desirable patterns of grooves for folds can be created on the sheet using a conventional negative etching technique (Allen 1986). The depth of the grooves can be controlled by the length of etching time. After etching the sheet is rolled into a tube. The etched grooves act as hinges when the tube is folded.

Figures 6.1(a) and (b) show part of the pattern of folds for the front and reverse sides of the sheet, which correspond to the outer and inner surfaces of the foldable cylindrical tube. This is the same pattern described in the stent graft of Chapter 3 where $\alpha_1 = \alpha_2 = 45^o$. The size of the sheet is 100 mm x 110 mm x 0.08 mm. The thickness of the sheet is the same as the thickness of the cover on currently produced stent grafts. The pattern of folds consists of square elements with sides of length 10 mm. The number of elements in both vertical and longitudinal directions are 8. The width of the grooves is 1.2 mm. These values are selected to produce a stent graft, as mentioned previously, that is useful for oesophageal and aortal conditions.

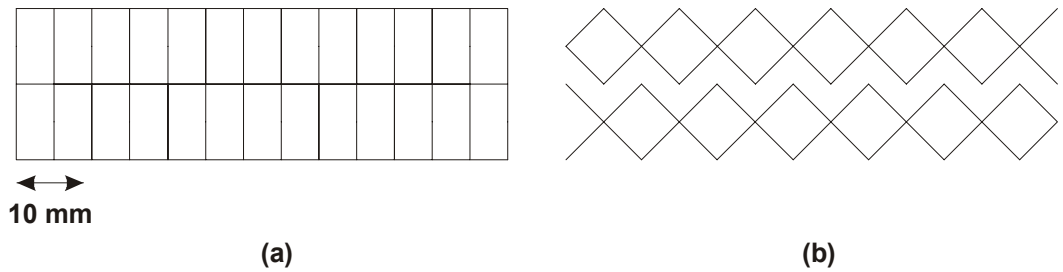

Figure 6.1 (a) Folding pattern of outer surface and (b) inner surface of the foldable cylindrical tube.

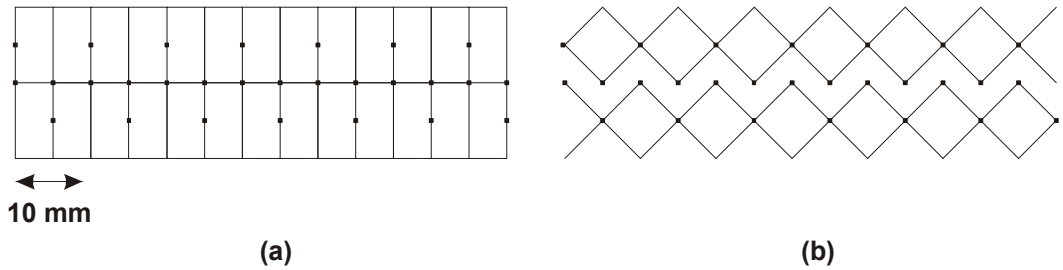

Figure 6.2 Folding pattern with squares hole on (a) outer surface and (b) inner surface of the foldable cylindrical tube.

Figure 6.2 shows a slightly different pattern of folds. In this pattern, holes are placed at each line intersection. These holes have a square shape. The positions of holes on the front and reverse sides of the sheet coincided, so they become through-holes. The holes help to alleviate high concentrations of stress when the sheet is folded. The length of the sides of the elements is again 10 mm. The width of folding lines is 0.5 mm, and the size of each hole is 0.5 mm x 0.5 mm. It is also possible to use circular holes.

These patterns were first stenciled on, and then both sides of the sheet were etched at the same time. The etching depth was half of the thickness of the sheet, which was 0.04 mm. After etching, the sheet was rolled and joined together by glue to form a cylindrical tube. The tube was folded manually.

Photographs of the foldable cylindrical tubes for the origami stent graft without and with holes in both its fully folded and expanded configurations are shown in Figures 6.3 - 6.5. The grooves created by etching outside and inside of the tubes became peak and trough creases, respectively. The foldable cylindrical tube with helical folds has also been produced successfully as shown in Figure 6.5.

Figure 6.3(b) shows a close-up photograph of the folds without holes and the folds width was 1.2 mm. As indicated in the photograph, some of the folds were distorted or improperly folded. Therefore, it seems that it might not be suitable to use a wider groove.

For the model shown in Figure 6.4 the radius and length of the foldable cylindrical tube before folding are 12.5 mm and 80 mm, respectively. The radius and length of the tube in its fully folded configuration are 5 mm and 45 mm, respectively. Thus, the tube is folded radially and longitudinally to about 40% and 56% of the original dimensions of the tube. These numbers could be smaller if the foldable cylindrical tube was designed with a large number of the elements as described in Chapter3.

Folding of the cylindrical tubes shown in Figures 6.3 - 6.5 is easily accomplished by first applying a small pressure to the intersections of the grooves as shown in Figure 6.6. This sets up the preferred direction of deformation. Then the tube is compressed in the longitudinal direction, and the stent graft is compressed to its fully folded configuration. For the tubes with helical lines the structure is twisted as well as compressed. This process causes all parts of the tube to collapse together instantly so that we do not need to fold each of the folds individually.

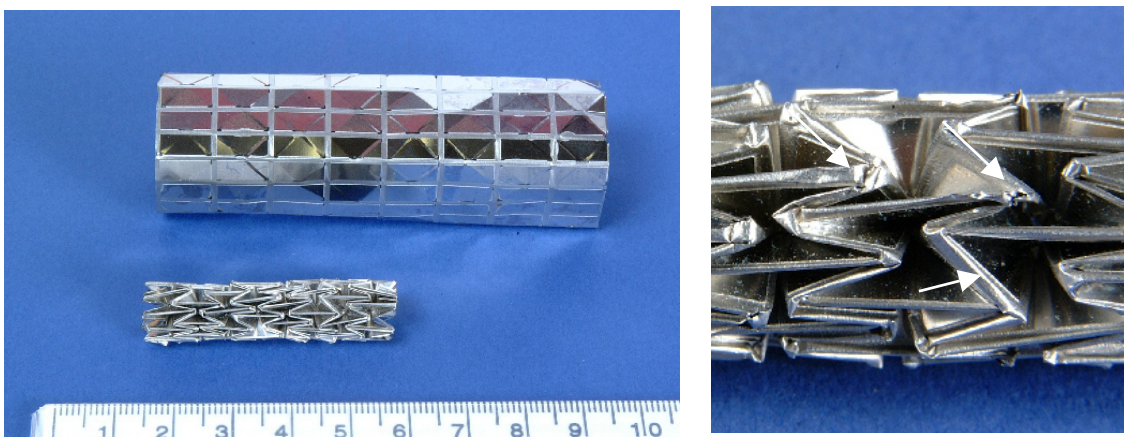

(a) **(b)**

Figure 6.3 (a) Cylindrical tube with 1.2 mm width folds in its fully folded and expanded configurations and (b) close up view of the folds.

(a)

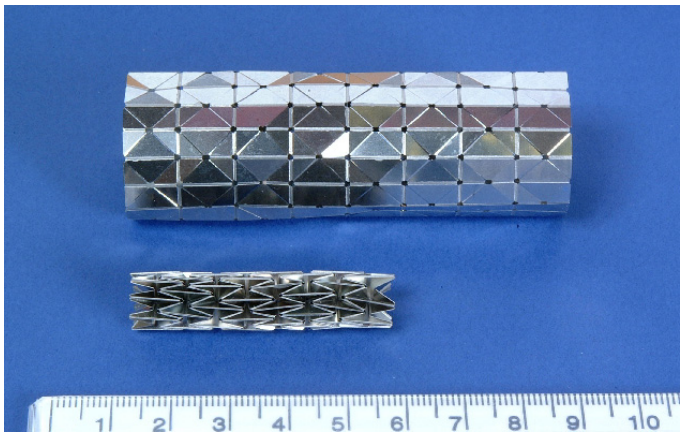

(b)

Figure 6.4 Cylindrical tube with 0.5 mm width folds in its fully folded and expanded configurations at (a) end and (b) perspective views.
The folding pattern contains holes at the intersections of folds.

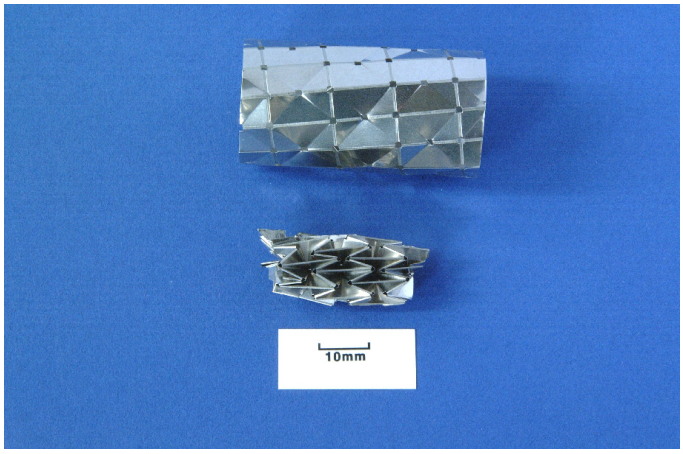

Figure 6.5 Stent graft with helical folds in its fully folded and deployed configurations.
Again holes exist in the folding pattern.

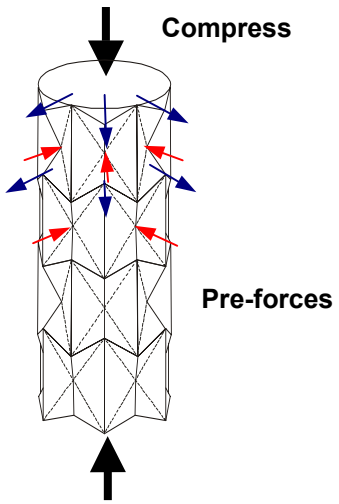

Figure 6.6 Forces in radial and longitudinal directions are applied to aid the folding of the stent graft.

The results above prove that the novel origami stent grafts can be produced using metals, and presumably any similar biocompatible materials. However the stainless steel stent graft was fairly rigid when deployed. Using different biocompatible materials such as polyester, PTFE or stainless steel of reduced density would improve flexibility.

In these prototypes, glue is used to connect the ends of the sheet to form a cylindrical tube. Spot welding may also be used. In the future it may be more appropriate to produce the stent graft using a tube instead of a sheet. However, to produce the grooves inside of a tube may be complicated.

The folding process required to fold the stent graft could be initiated using a mechanical method such as a press. The use of a press to create an uneven pattern on the surface of a drinking can has been experimented with and used successfully by Miura (2002). This same method would conceivably work well in the automatic folding of the metallic stent.

6.2 Processing techniques of shape memory alloy sheet

As mentioned in Chapter 2, there are many potential advantages given by the use of SMA for the stent graft. The biggest advantage is that a stent graft can self-expand to a pre-determined shape by body heat. The main difference between existing SMA stent grafts and the stent graft presented here is that the latter is made using a sheet rather than a wire. This is the first time that a stent has been manufactured using SMA in sheet form.

In this section, processing techniques of a SMA sheet including photochemical etching and heat-treatment are investigated to produce an origami stent graft.

6.2.1 Method of etching

The etching technique applied here is based on photochemical etching for the microstructures of thin SMA film described in Chapter 2. SMA is one of the most difficult materials to etch so that a key challenge here is to determine a useable combination of photoresist, etchant materials and processes.

TiNi SMA sheet can be etched using either positive or negative photochemical etching processes. Positive etching is a reliable technique, although the advantage of negative etching is that the etching process is easier and cheaper than positive etching (Allen 1986). Table 6.1 gives a summary of the positive and negative photochemical etching processes.

We adopted both processes for a 0.08 mm thick Ti-rich (Ti-49.8 at%Ni) TiNi sheet. Firstly, three types of artwork (etching patterns) were prepared. Figures 6.7(a) and (b) show the designs for the trial positive and negative etching techniques. The white lines on a black background in Figure 6.7(a) and black lines on a white background in Figure 6.7(b) are the stencils which were etched. Five different line widths between 0.1 and 1.4 mm were etched. The lengths of the lines were 10 mm, and the space between them is 3 mm.

Figure 6.7(c) shows the folding pattern of the stent graft on the front and reverse sides of the sheet, which is the same pattern for the stainless steel stent graft shown in Figure 6.2. These are the artworks used for positive etching. The size of the sheet is 100 mm x 50 mm. 50 mm width is the widest SMA sheet which is commercially available. The pattern of the folds consists of square elements of sides 10 mm with central holes of 0.8 mm. The width of the grooves is 0.3 mm. The number of elements in the vertical and longitudinal directions are 8 and 4, respectively. The holes are matched up on the front and back sides of the sheet so that they become through holes.

Table 6.1 Photochemical etching process of the shape memory alloy sheet with positive and negative photoresists.

Positive etching with a liquid photoresist	Negative etching with a dry photoresist
Artwork	
1. Design patterns of grooves	
2. Print out with photo prism printer (2400 pix)	
Photoresist	
3. Clean specimen with pumice powder	3. Clean specimen with pumice powder
3. Dip coat with a positive photoresist of HRP 506 with 30 mm/min – 0.06 mm in thickness	4. Laminate a negative photoresist of Riston 205 with 0.035 or 0.07 mm in thickness
4. Soft bake at 348K for 30 min	–
5. 2kW UV expose for 60 sec	5. 2kW UV expose for 15 sec
6. Develop using PLSI	6. Develop using potassium carbonate
7. Water rinse	7. Water rinse
8. Hard bake at 393K for 60 min	8. Hard bake at 363K for 30 min
Etching	
9. Etch with solution of HF: HNO_3: H_2O =1:1:2, 1:1:4 and 1:4:5	9. Etch with solution of HF: HNO_3: H_2O =1:1:4
10. Remove photoresist	10. Remove photoresist

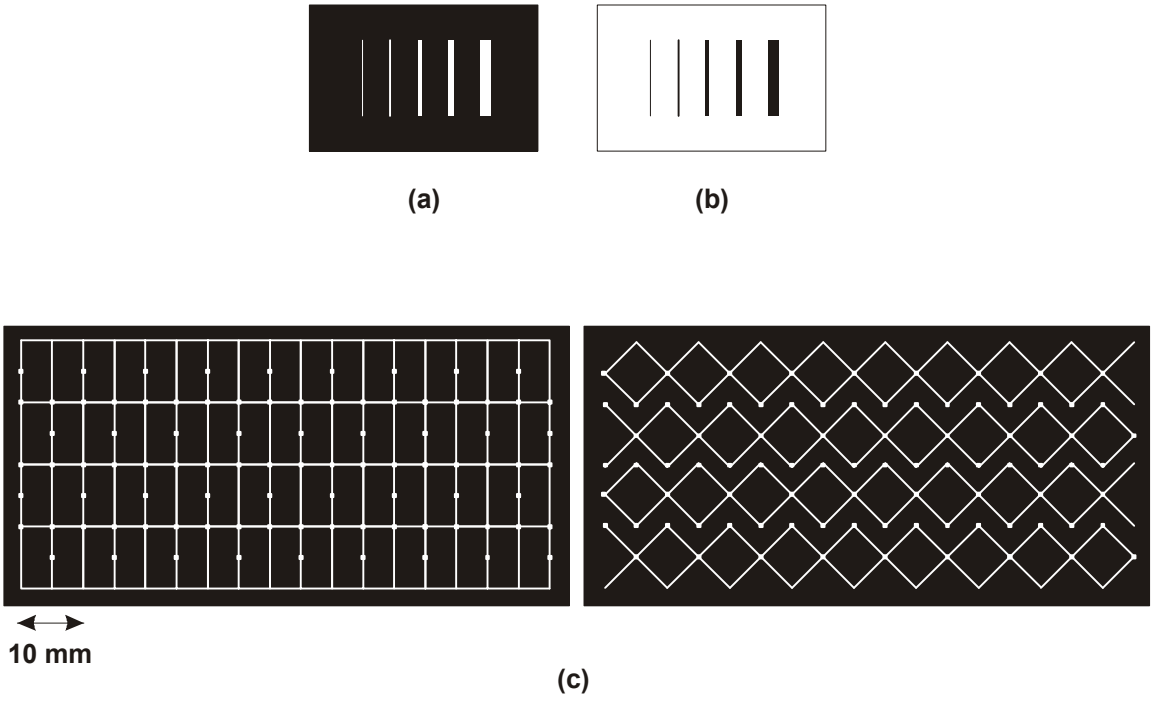

Figure 6.7 Artworks for the etching pattern with different line widths (0.1, 0.25, 0.5, 0.75 and 1.4 mm) for (a) a positive etching and (b) a negative etching. (c) Positive etching pattern of folds of the origami stent graft on the front and back sides of the sheet.

After the artwork has been created, the sheet is masked against the chemical etchant by a photoresist. The etchant reacts only on the sheet surface where no photoresist is present, leaving the desired pattern of grooves on the sheet. The photoresist coating must not break down chemically or physically during etching. In order to obtain good adhesion between the sheet surface and the photoresist, the sheet has to be scrubbed clean and abraded using a pumice powder.

For positive etching, a positive-working photoresist (506 Arch Co., USA) was used. It was applied by dip coating, and its thickness could be controlled by the speed of the removal from the dip coater. In this case, the speed was 30 mm/min, which led to a photoresist thickness of 0.006 mm. It is important to make a uniform coating in order to

obtain uniform exposure characteristics. Then, the specimen was soft baked at 348K for 30 minutes to drive off the photoresist solvent from the coating. The pattern was then exposed on the sheet with a 2 kW ultraviolet (UV) light for 60 seconds. It was then developed in a developer with a mixture of 5% trisodium phosphate and 0.75% sodium metasilicate (PLSI Arch, USA) to form a stencil of the pattern on the surface. After that, it was baked at 393 K for 60 minutes to ensure complete drying and to enable the photoresist stencil to toughen.

For negative etching, the specimen was coated with either single or double layers (0.035 mm or 0.070 mm in thickness) by a negative dry photoresist (Riston 205, Dupont Co.). For a negative photoresist, soft baking is not required before the exposure of the UV. The specimen was exposed to a 2 kW UV source for 15 seconds. Then it was developed in a 1% solution of potassium carbonate, and baked at 363 K for 30 minutes.

Finally, the sheet was etched. The etchant is also chosen according to the sheet material. In this experiment the etchant contains mixed solutions of $HF/HNO_3/H_2O$ for both the positive and negative etching processes. To check the effect of the ratio of HF/HNO_3 in the solution, an etchant of $HF:HNO_3:H_2O$ in different proportions 1:4:5, 1:1:2 and 1:1:4 by volume were applied. The etchant was carefully mixed in a plastic container in the following order:

1. Prepare the correct quantity of H_2O;
2. Prepare the correct quantity of HF;
3. Combine HF to H_2O gently;
4. Prepare the correct quantity of HNO_3;
5. Combine HNO_3 to H_2O + HF gently.

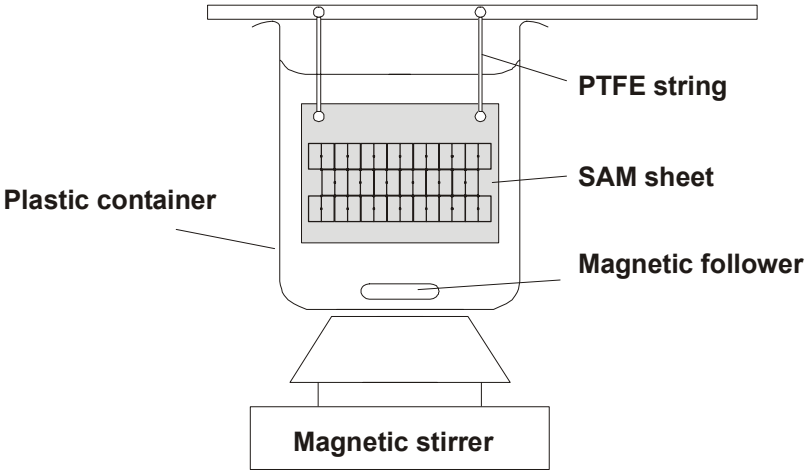

Figure 6.8 Layout of the etching apparatus.

The layout of the etching apparatus is illustrated in Figure 6.8. The etchant was kept at 291K and was stirred slowly to create uniform etching. The sheet was held by strings composed of PTFE.

The sheets to test different lines widths shown in Figure 6.7(a) and (b) were etched until of a sheet thickness of 0.08 mm reduced to half, which was between 3 and 25 minutes. The sheet with the patterns of folds for the origami stent graft shown in Figure 6.7(c) was etched until all central through-holes appeared.

After etching, photographs of the etched SMA sheets were taken using a microscope (Olympus, Japan) to observe the quality and properties of the etched patterns. More detailed information of the etched surface was gained using a Scanning Electron Microscopy (SEM) (JSM-6300, JEPL Co., Japan).

When etching a metal using a liquid etchant, it is etched not only in the depth direction, as desired, but also to the side, which results in the formation of a sidewall under the photoresist known as undercut, *U*, shown in Figure 6.9. As a quantitative description of the shape of the etched recess, the etch factor is defined as follows,

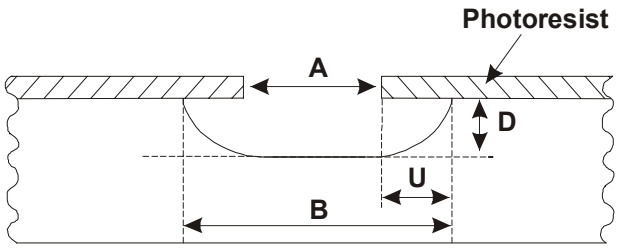

Figure 6.9 Etch factor = *D*/*U*.

$$\text{etch factor} = \frac{\text{depth of etch } (D)}{\text{undercut } (U)} \tag{6.1}$$

where undercut U is equal to $1/2(B-A)$. A is the width of the gap in the developed photoresist, and B is the width of the gap that is actually etched. To calculate etch factor and the speed of the etching, the etched depth and width were measured using a surface profiler (Surfometer, Ransducer Technology, UK) and also under the microscope.

The experimental methods described above revealed useful information about the etching process for SMA sheets. This information includes:

- Correct photoresist process, e.g. photoresist type, thickness, UV exposure (intensity and time), and baking temperatures;
- Correct proportion of $HF/HNO_3/H_2O$ of the etchant;
- Etch speed;
- Etch factor.

The results of the experiments are given in Section 6.3.

6.2.2 Bending test

The Ti-rich TiNi SMA sheet has a 'rolling' direction which is a result of the cold work that is used to form a flat sheet. The shape memory effect was examined by a bending test to check the effects of bending direction of etched grooves with respect to the rolling direction of the SMA sheet, and the effect of the different groove widths. The bending test was carried out as shown in Figure 6.10. The original shape of the SMA was a flat sheet. A specimen was rolled in a radius R_0, and then heated at 393K. The radius of the specimen after heating was denoted as R. Photographs were taken before and after bending, and also after heating. R was measured from the photograph. Equations for strain of a bent surface, ε, strain recovery, $\varepsilon_{\text{recovery}}$, and recovery ratio are

$$\varepsilon = \frac{t}{2R_0} \tag{6.2}$$

$$\varepsilon_{\text{recovery}} = \frac{t}{2}\left(\frac{1}{R_0} - \frac{1}{R}\right) \tag{6.3}$$

and

$$\text{Recovery ratio}(\%) = \frac{\varepsilon_{\text{recovery}}}{\varepsilon} \times 100 \tag{6.4}$$

where t is the thickness of the specimen.

Specimens used for this bending test are illustrated in Figure 6.11. The size of the specimens is 5 mm x 30 mm x 0.08 mm. The specimens are cut at 0^o, 90^o and 45^o with respect to the rolling direction. The three different groove widths, w_g, are 0.3, 0.5 and 0.7 mm. The etching depth, d is 0.04 mm. A negative photochemical etching process was used. The results of these tests are given in Section 6.3.

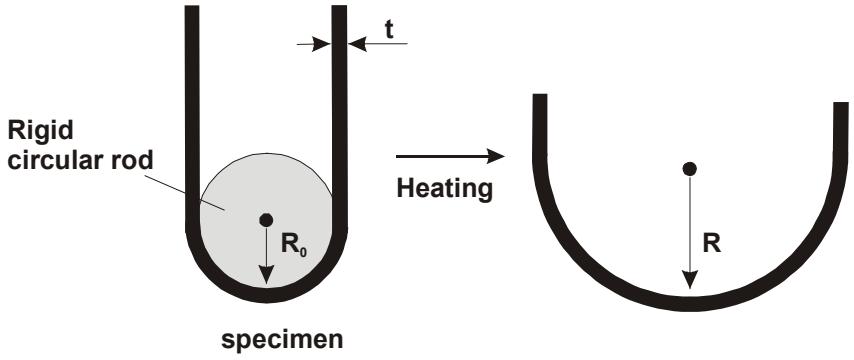

Figure 6.10 Schematic illustration of the SMA bending test

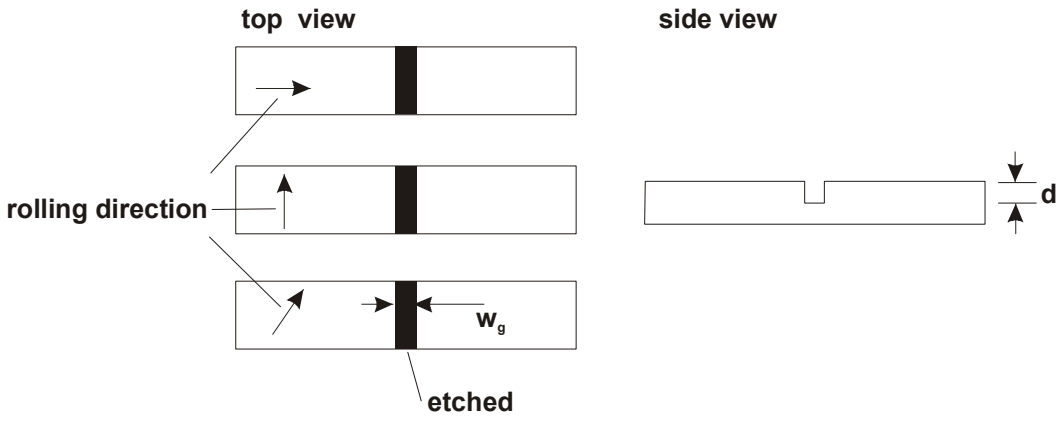

Figure 6.11 Illustrations of the specimens of Ti-rich SMA sheet with various angles between cuts and the rolling direction, and widths for the bending test.

6.2.3 Heat treatment

In general, the Ti-rich TiNi SMA sheet as supplied cracked when folded due to lack of ductility, making it unsuitable for the production of stent grafts. The SMA sheet was heat-treated to improve its ductility. The 0.08 mm thick Ti-rich TiNi SMA sheet is annealed at 773K for 10 minutes or at 1073K for 1 hour. Annealing at temperature between 773K and 1073K leads to the annihilation of the defects of crystal lattices (dislocations) (Otsuka and Wayman 1998), which are the features giving rise to the resistance to the plastic deformation and therefore cracking. The heat treatment was applied in a vacuum tube (VPC-250F, ULVAC Co) to avoid surface oxidation.

The transformation temperatures before and after treatment are measured by Differential Scanning Calorimetry (DSC) (DSC-8230L, Rigaku Co.) under a flow of argon gas in the temperature range from 473 to 546K with a heating/cooling rate of 0.17 Ks^{-1} to examine the effect of the heat treatment. Then the same bending test described in Section 6.2.2 is carried out to check the characteristic of the shape memory effect after the heat treatment. Again the results of these tests are given in section 6.3.

6.3 Results and discussion of the processing technique for SMA

6.3.1 Positive etching

The widths of the UV exposed lines of the pattern on the SMA sheets coated with the positive liquid photoresist were measured under a microscope before etching. If the photoresist was over exposed, it was difficult to maintain correct line widths, and if under exposed, there was difficulty developing the image. In this experiment, the error from the original width in the artwork was below 0.03%, implying that the exposure time was correct. Cracking of the photoresist did not occur, which indicated that the baking temperature and time were also correct.

The photoresist peeled off immediately after etching was started with the etchant ratio of $HF:HNO_3:H_2O = 1:4:5$, but it did not peel off when the etchant ratio was either $HF:HNO_3:H_2O = 1:1:4$ or $1:1:2$. Figures 6.12(a) and (b) show photographs taken under a microscope at x5 magnification and cross-sectional profiles of the etched line of 0.5 mm width with different etching times in etchant ratio of $HF:HNO_3:H_2O = 1:1:4$ and $1:1:2$. It took 20 and 10 minutes to etch the pattern of 0.04 mm in depth into the sheets, for the respective $HF:HNO_3:H_2O$ ratios. The dark shadows in the photographs are a consequence of sloping side walls, or undercuts as previously described (see Figure 6.9). As shown in Figure 6.12 in both etchant ratios the undercut of etching increased as the etching time increased. The final size of the etched line and the width of the undercut U are also shown in Figure 6.12. In the case of $HF:HNO_3:H_2O = 1:1:2$, the undercut is about one third smaller than the results in the etchant ratio of $HF:HNO_3:H_2O = 1:1:4$, that is, the etched slope of the side wall of the etched line is steeper and the edge is sharper. However as shown in both the photographs and by the slope of the surface above the undercut in the profiles of Figure 6.12(b), the surface immediately above the undercut is adversely affected by etching and becomes worse as etching progressed.

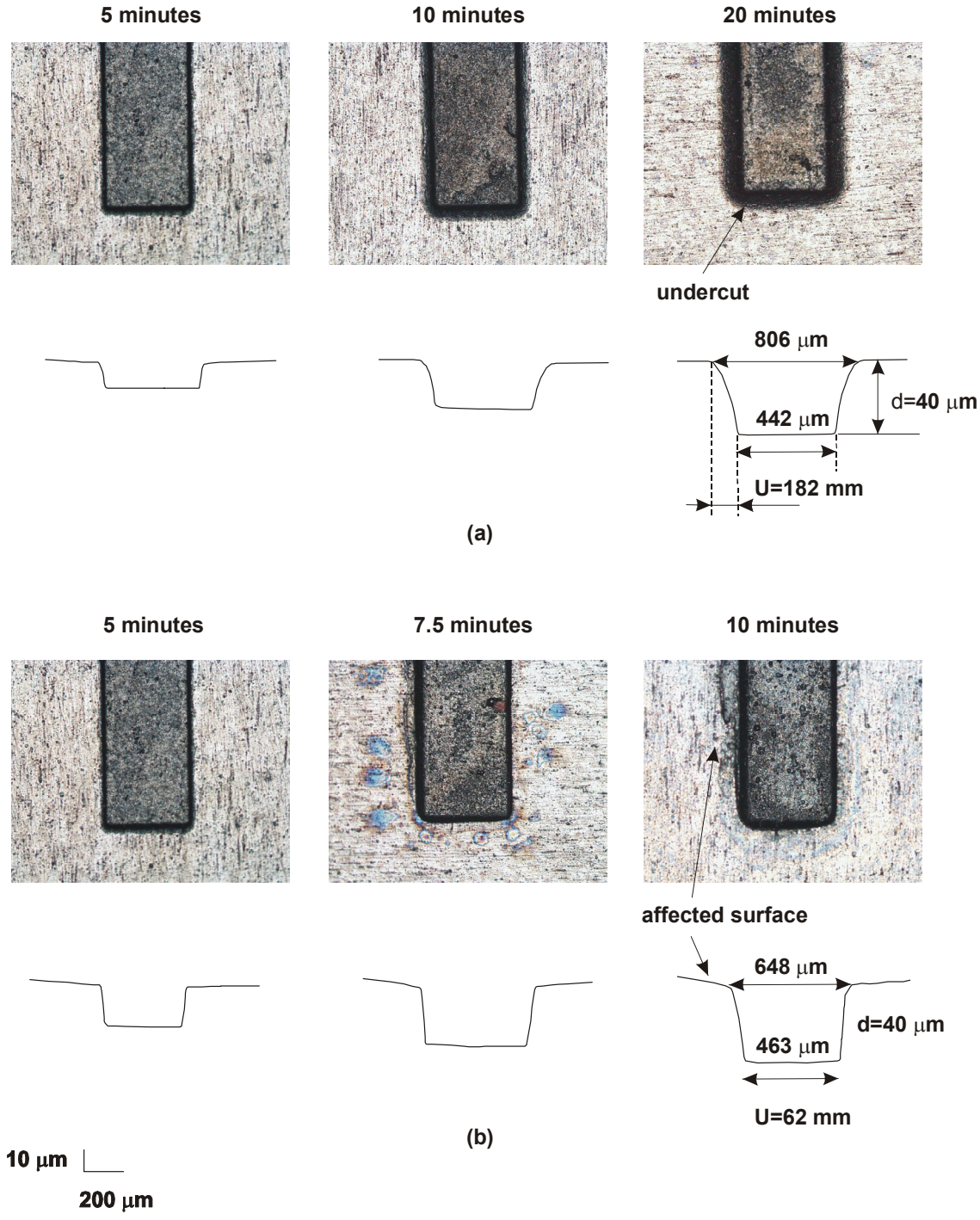

Figure 6.12 Optical microphotographs and profiles of the etched SMA sheet with a line of 0.5 mm width using the etchant ratio of HF:HNO_3:H_2O = (a) 1:1:4 and (b) 1:1:2.

Further results of the undercut of each of the line widths subjected to etching time in etchant ratio of $HF:HNO_3:H_2O = 1:1:4$ and 1:1:2 are shown in Figure 6.13(a) and (b), respectively. The solid and dashed lines represent an average undercut with the etchant ratio of $HF:HNO_3:H_2O = 1:1:4$ and 1:2:2, respectively. In the case of $HF:HNO_3:H_2O = 1:1:4$, the etching speed of the undercut of wide lines (≥ 0.75 mm) is 9.02 μm/min. It is slightly faster than that of narrow lines (≤ 0.5 mm) which is 7.79 μm/min. For $HF:HNO_3:H_2O = 1:1:2$, the speed is roughly 4.46 μm/min. The size of the undercut for $HF:HNO_3:H_2O = 1:1:2$ is about two or three times larger than the one for $HF:HNO_3:H_2O = 1:1:4$.

Figure 6.14 shows the results of the etched depth of five different line widths subjected to different etching times. The solid and dashed lines represent an average etching speed with the etchant ratio of $HF:HNO_3:H_2O = 1:1:4$ and 1:2:2, respectively. In the case of $HF:HNO_3:H_2O = 1:1:4$, the etching speed for wide lines (≥ 0.75 mm) is 1.7 μm/min, which is slightly faster than the etching speed of narrow lines (≤ 0.5 mm) of 1.53 μm/min. Using $HF:HNO_3:H_2O = 1:1:2$, the speed is 3.22 μm/min and there is no difference between different line widths. The depth rate achieved by etching using $HF:HNO_3:H_2O = 1:1:2$ is about twice as fast as the rate for $HF:HNO_3:H_2O = 1:1:4$.

The etch factors of both etchant ratios are calculated using Equation (6.1). Figure 6.15 shows that the etch factors are consistently between 0.2 and 0.3 for $HF:HNO_3:H_2O = 1:1:4$ and range between 0.3 and 0.65 for $HF:HNO_3:H_2O = 1:1:2$.

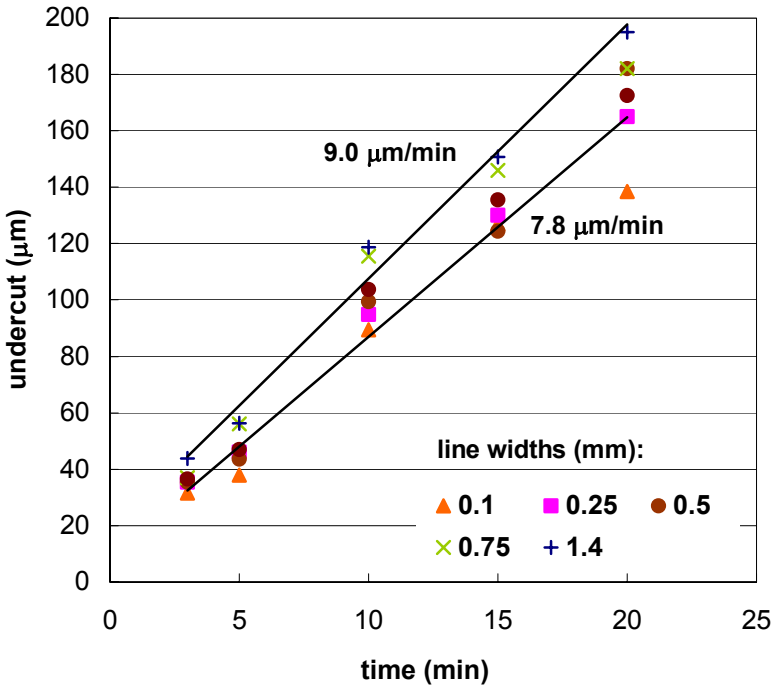

(a)

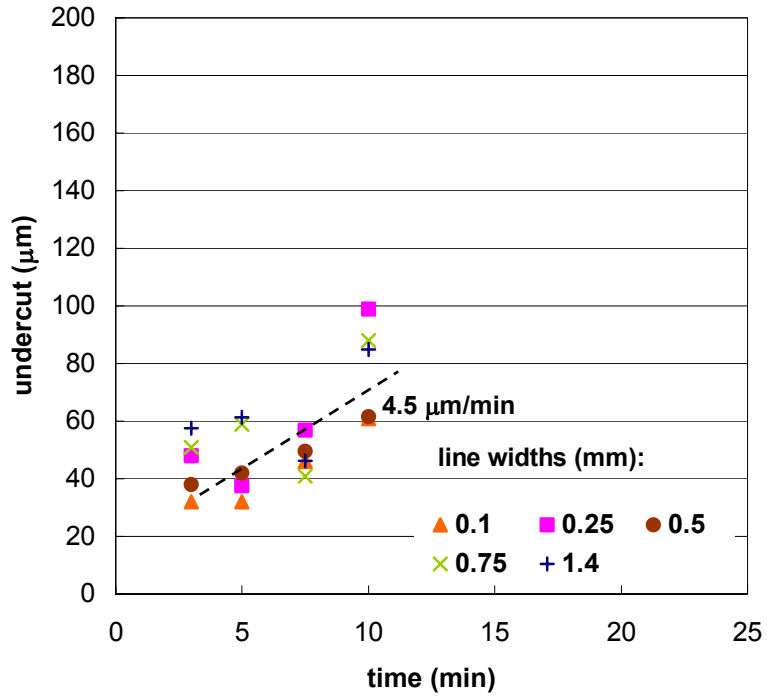

(b)

Figure 6.13 Change of undercut with time for $HF:HNO_3:H_2O$ = (a) 1:1:4 and (b) 1:1:2.

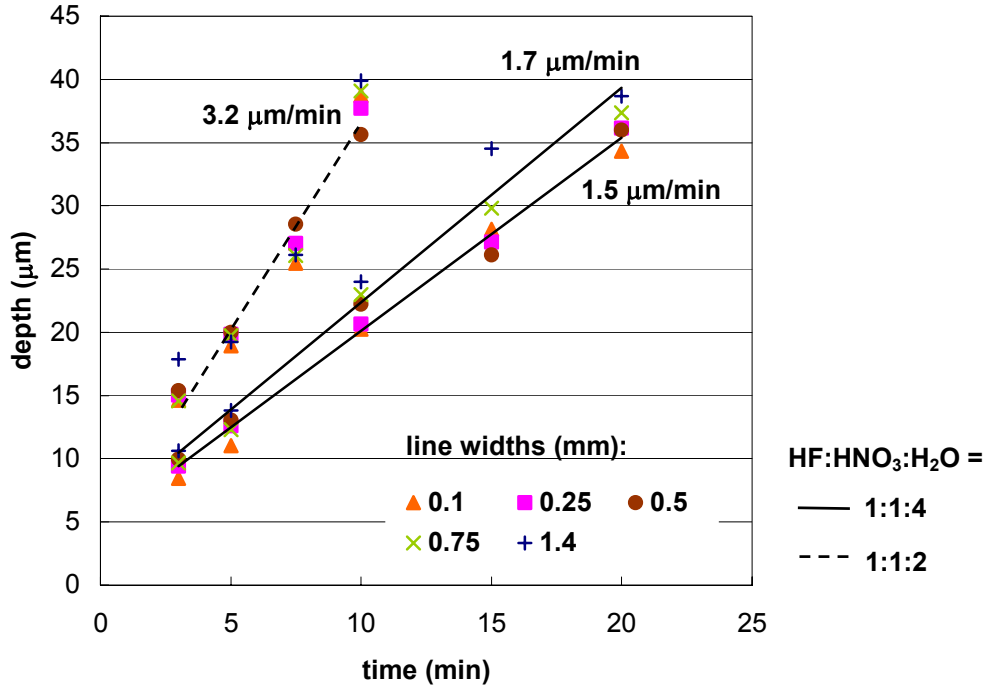

Figure 6.14 Change of etch depth with time.

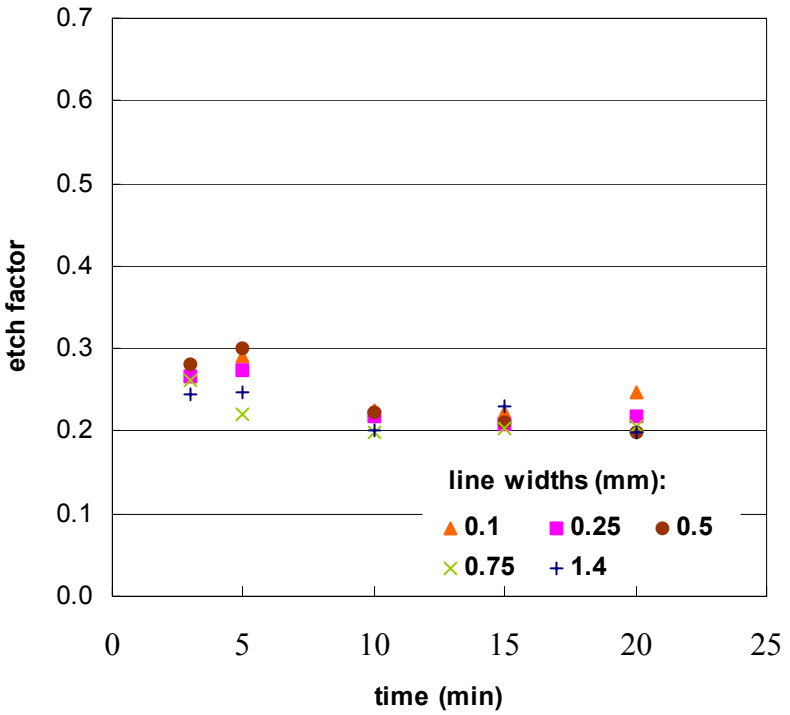

(a)

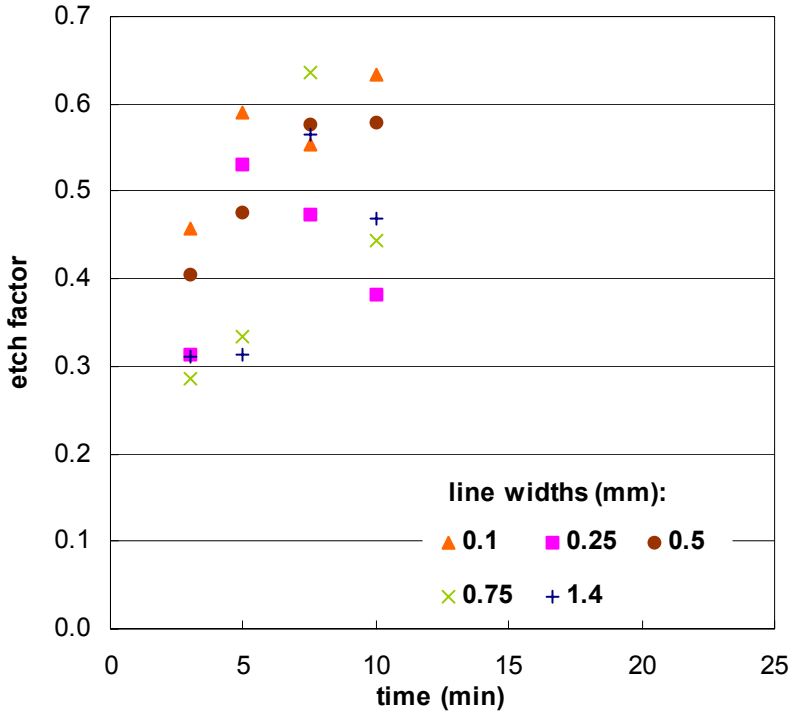

(b)

Figure 6.15 Etching factor with time when the etchant of $HF:HNO_3:H_2O$ = (a) 1:1:4 and (b) 1:1:2.

6.3.2 Double sided etching using a positive photoresist

The stent pattern shown in Figure 6.7(c) was successfully etched and a good folding pattern was created on a SMA sheet. The total times for all central holes to etch through the sheet are 23 and 10 minutes, for the ratios $HF:HNO_3:H_2O$ = 1:1:4 and 1:1:2 respectively.

Figure 6.16 shows the photographs of the etched Ti-rich TiNi SMA sheets taken under a microscope at x5 magnification just after etching. The photo stencil is still on these sheets. When the etchant ratio $HF:HNO_3:H_2O$=1:1:4 was used the photoresist adhered very well (Figure 6.16a), and the undercut could be seen through the photo stencil. On the other hand, as shown in Figure 6.16(b), using the etchant with higher ratio of HF/HNO_3, the photoresist stencil unfortunately came off and the surface above the undercut was affected by etching.

Figure 6.17 shows the photograph of the etched Ti-rich TiNi SMA sheets in $HF:HNO_3:H_2O$=1:1:4 taken under a microscope at x5 magnification after removal of the photoresist. The undercuts of both lines and hole were the same, approximately 0.13 mm. Therefore the etched lines and the size of the hole became 0.56 mm and 1.06 mm, which were 1.87 and 1.34 times their original intended size, respectively.

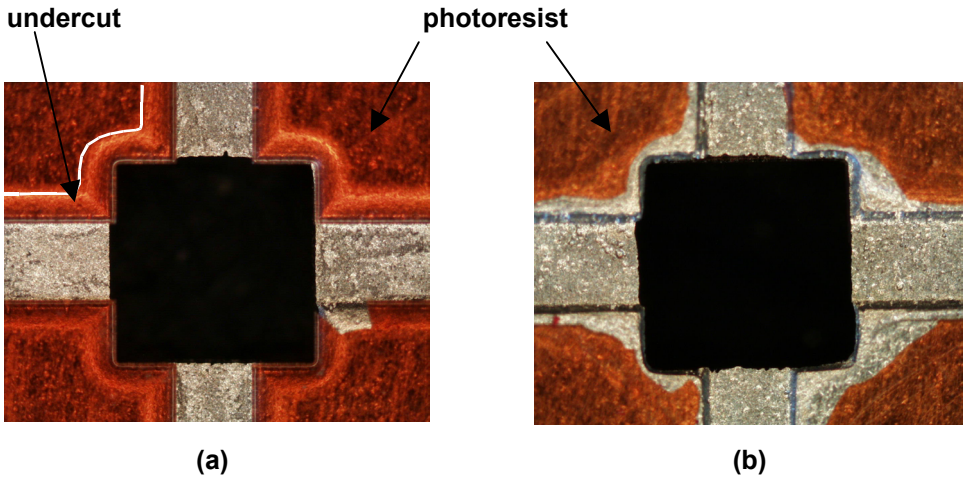

Figure 6.16 Optical microphotographs of the Ti-rich TiNi SMA sheet etched using the etchant ratio of (a) $HF:HNO_3:H_2O$=1:1:4 and (b) 1:1:2.

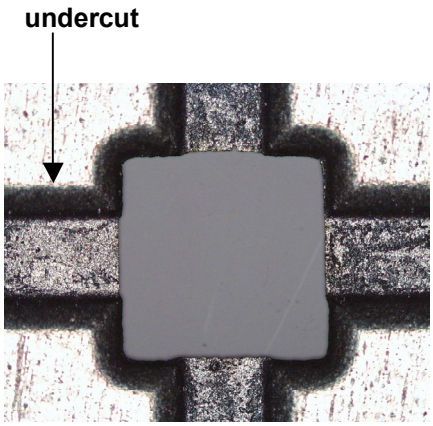

Figure 6.17 Optical microphotographs of the Ti-rich TiNi SMA sheet etched with the etchant ratio of $HF:HNO_3:H_2O$=1:1:4.

Figures 6.18(a) and (b) show the photographs of the entire back and front of the Ti-rich TiNi SMA sheet etched using the ratio of $HF:HNO_3:H_2O$ = 1:1:4. Good folding patterns were produced uniformly across the entire area of the sheet. Figures 6.19(a) and (b) show close-up photographs of the same sheet. Interestingly, the square holes made by double sided etching are clear through the sheet, a distance of 0.08 mm or 0.04 mm on each side, even though the average etched depth of the single-sided lines was a slightly shallower 0.0365 mm.

An SEM examination focused on the area of the sheet that is specified in Figure 6.20(a). Figures 6.20(b) and (c) show photomicrographs of the top (location A) and side (location B) views of the etched surface of the Ti-rich TiNi SMA sheet magnified at x130 and x150 times, respectively. The etched surface is smooth (relatively unpitted), which is a successful result, indicating that etching does not adversely affect the surface of the SMA sheet.

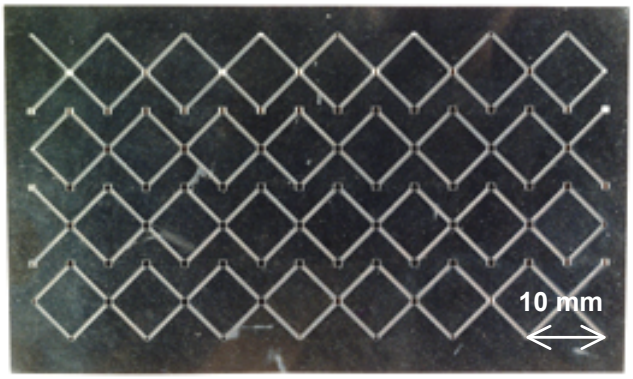

(a)

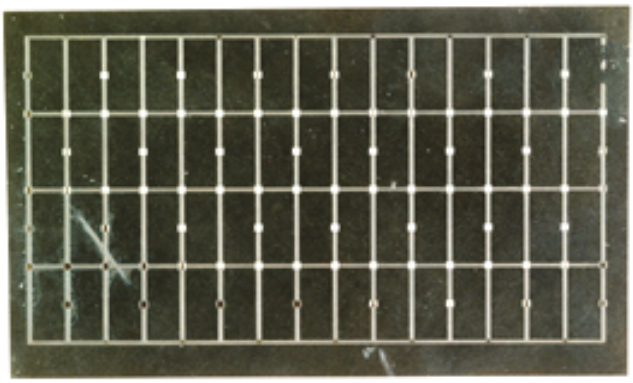

(b)

Figure 6.18 Photographs of the etched pattern into (a) back and (b) font side of the Ti-rich TiNi SMA sheet.

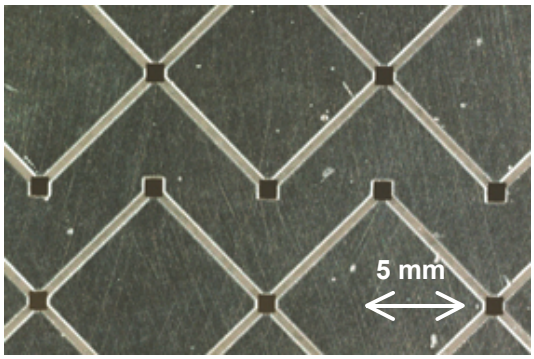

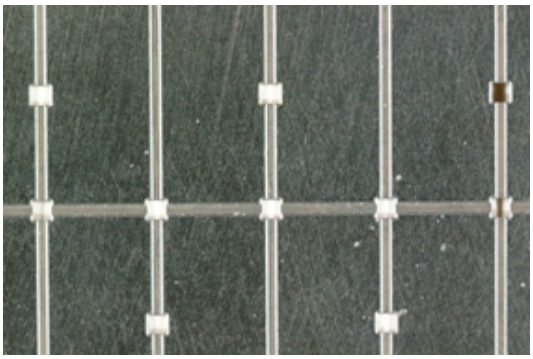

(a) **(b)**

Figure 6.19 Close up photographs of the etched pattern into (a) back and (b) front side of the Ti-rich TiNi SMA sheet.

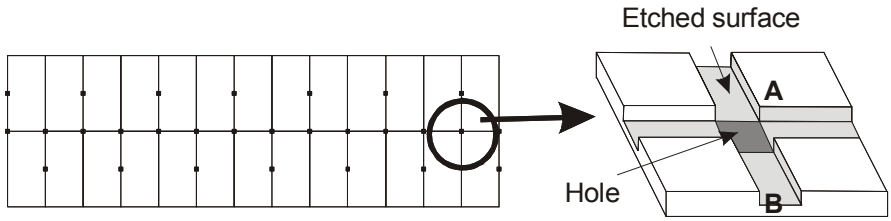

(a)

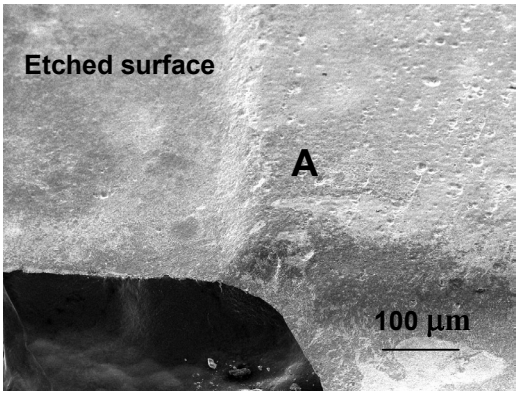

(b)

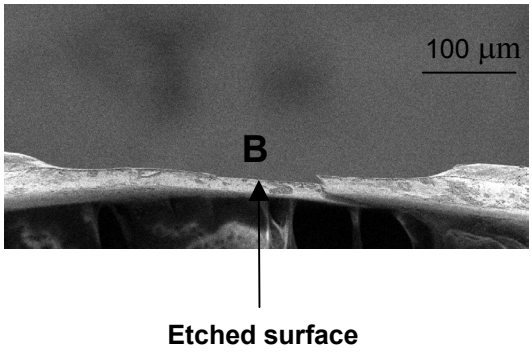

(c)

Figure 6.20 (a) Illustration showing the locations of the SEM observation (b) Projection and (c) side view of photomicrographs of the etched Ti-rich TiNi SMA sheet.

6.3.3 Negative etching

During the negative etching process a single dry photoresist of 0.035 mm in thickness peeled off immediately after etching started. It was not resistant enough to adhere to the SMA sheet. However, the etching pattern was successfully transferred onto the sheet when a double layer of photoresist totaling 0.070 mm in thickness was used. The error from the original width in the artwork was below 0.05%, implying that the exposure time was correct. Cracking of the photoresist did not occur, indicating that the baking temperature and time were also correct.

A sheet with the dry photoresist was etched with the etchant ratio of $HF:HNO_3:H_2O = 1:1:4$. Figures 6.21, 6.22 and 6.23 show the results of etched depth, undercut and etch factor with respect to the etch time. In these figures, filled symbols are the results of negative etching, and for comparison, the results of positive etching using the same etchant are also shown. Etch speed is almost the same as that with the positive liquid photoresist. However, the undercut is smaller. Therefore, the etch factor is larger for negative etching (between 0.3 and 0.5) than for positive etching.

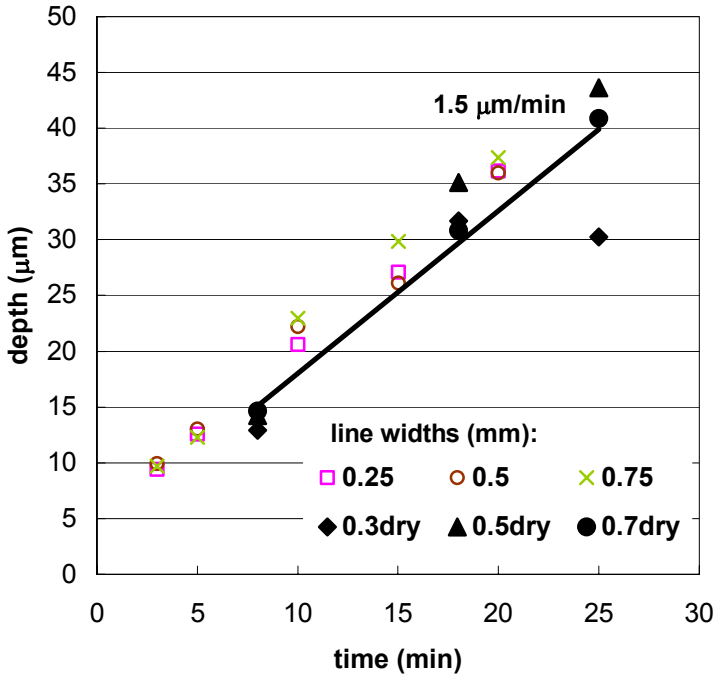

Figure 6.21 Change of etch depth with time for negative etching of SMA sheet.

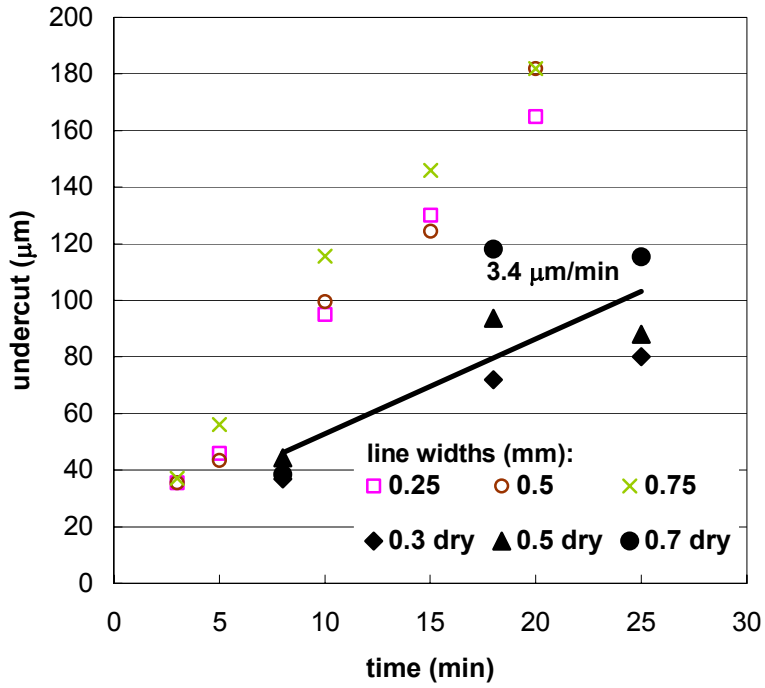

Figure 6.22 Change of undercut with time for negative etching of SMA sheet.

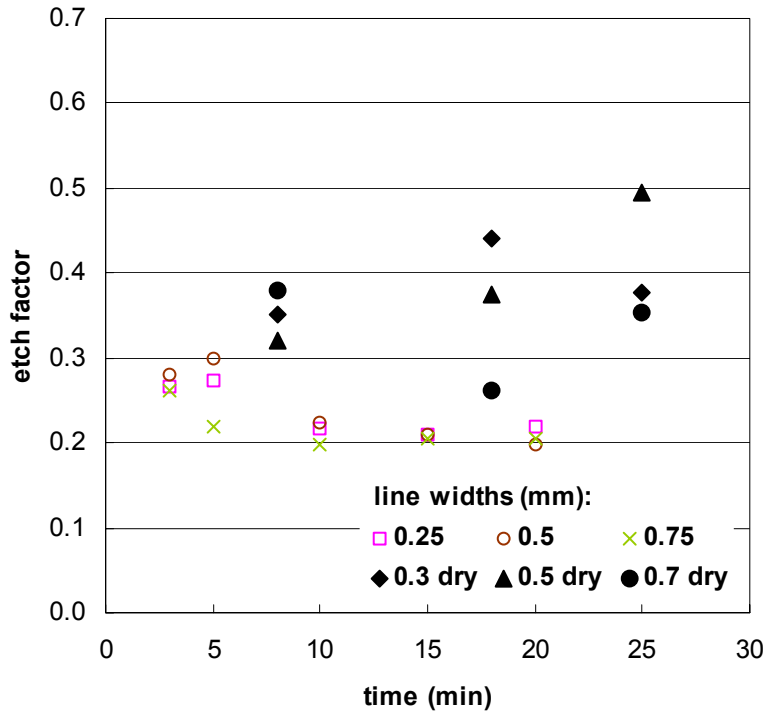

Figure 6.23 Etching factor with time for negative etching of SMA sheet.

6.3.4 Factors influencing etching process

- **Etchant ratio of HF/HNO_3**

The positive etching experiment revealed that a ratio of $HF:HNO_3:H_2O = 1:4:5$ is not suitable to etch SMA sheet. The ratio of HF and HNO_3 was too high, causing the photoresist to peel off during etching.

When the etchant ratio of $HF:HNO_3:H_2O = 1:1:2$ was used, the etch speed was 3.2 μm/min, which is twice as fast as the etch speed when the etchant ratio of $HF:HNO_3:H_2O = 1:1:4$ was used. However, as shown in Figures 6.12(b) and 6.16(b), the etchant of $HF:HNO_3:H_2O = 1:1:2$ had adverse affects on the sheet. Therefore a conclusion of this test is that an etchant ratio of 1:1:4 is the most suitable for a clean, undamaged etched surface. It may be possible however to improve etching speed (and production costs) by using a higher ratio of HF/HNO_3 etchant at the beginning of the etching process, and then switching to a more diluted mixture.

- **Photoresists**

Both positive and negative photoresists can be used for etching of SMA sheets. The experiments showed that the positive photoresist is tougher and adheres to the sheet better. A positive photoresist with a thickness of only 0.006 mm gave reliable results, whereas a negative photoresist with a much higher thickness of 0.035 mm peeled off during etching. A double-coated negative photoresist was able to withstand the etching process. The advantage of the thin photoresist is that it can allow a much finer etching resolution. Therefore, a positive photoresist would be a more useful technique when focus is directed towards the miniaturisation of the stent or stent graft for coronary use. The advantages of negative etching are that the etching process is easier and cheaper. Furthermore, uniform coating can be applied over a large area, which would become particularly important in the large scale manufacture of stents and stent grafts.

From the results of the negative etching given in Figure 6.21, it is found that etching speed was the same as that of the positive etching. However, from Figure 6.23, the undercut for the negative etching is smaller than that of the positive etching, which is because of thicker photoresist. Using the negative photoresist, etch factors were improved from 0.25 to between 0.3 and 0.5 when the etchant of $HF:HNO_3:H_2O$ was diluted to 1:1:4. However, this is still a very small etch factor compared with that for the other materials, such as, stainless steel or copper (1.5–2.0), because SMA has poor etching characteristics (Allen 1986). The small etch factor indicates that the etched slope is not sharp, which might be a rather good property for the stent design because it can alleviate concentrations of stress when the sheet is folded.

- **Etched width and the double sided etching**

In the case of $HF:HNO_3:H_2O$ = 1:1:4, as shown in Figures 6.14, the etching speed become faster when the width is larger than 0.75 mm. As shown in Figure 6.13(a), the undercut also increases when the etched groove width is greater than 0.75 mm. These are the results of the one sided etching. When double side etching is carried out, the values of the undercut of lines and the square holes of 0.3 and 0.8 mm in width were the same, as shown in Figure 6.20. Because in general, the undercut with double sided etching is smaller than that with one sided etching (also shown by Allen 1986), the undercut of square holes is not excessive. In order to get the desired depth and widths for the stent folding patterns, the etched depth and size of undercut for single or double sided etching should be taken into account during the design stage.

6.3.5 Bending test

Figure 6.24 shows the results of the bending test. The specimens have an etched groove width w_g of 0.7 mm and have cuts in different directions with respect to the rolling direction. For 0^o, the specimen fails through cracking. For 45^o, ε is 2.4% and the recovery rate is 95.8%, i.e., the specimen recovers almost to the original flat shape. However, the specimen is cracked when ε is larger than 2.4%. For 90^o, ε is 2.4% and the recovery rate is 92.5%, i.e., the specimen also recovered almost to the original flat shape. At this angle to the rolling direction the specimen could be bent until ε is 8.9%.

Table 6.2 shows the recovery ratios with different w_g and angle. When w_g was 0.3 mm, all of the specimens cracked. For 0^o, all specimens also cracked. For 45^o or 90^o, the specimen with w_g equal to 0.5 or 0.7 mm and ε is less than 3%, the specimens recovered almost completely to their original flat shapes when heated.

These results show that the direction of the cut with respect to the rolling direction of the Ti-rich TiNi SMA sheet is important. It is best to make cuts at 90^o, and acceptable to make cuts at 45^o, but it is not recommended to make the cuts at 0^o to the rolling direction. Furthermore, the width of the cut is important, and gives a better result if it is greater than 0.5 mm.

Table 6.2 Recovery ratio (%) of effects of etched grooves width and direction.

	Recovery ratio (%)								
w_g	0.3 (mm)			0.5 (mm)			0.7 (mm)		
strain (%) / (deg)	less than 3	3-6	more than 6	less than 3	3-6	more than 6	less than 3	3-6	more than 6
0	C	C	C	C	C	C	C	C	C
45	C	C	C	96.10	C	C	95.77	C	C
90	C	C	C	92.12	87.69	C	92.50	82.27	71.83

C:crack when the specimen was bent

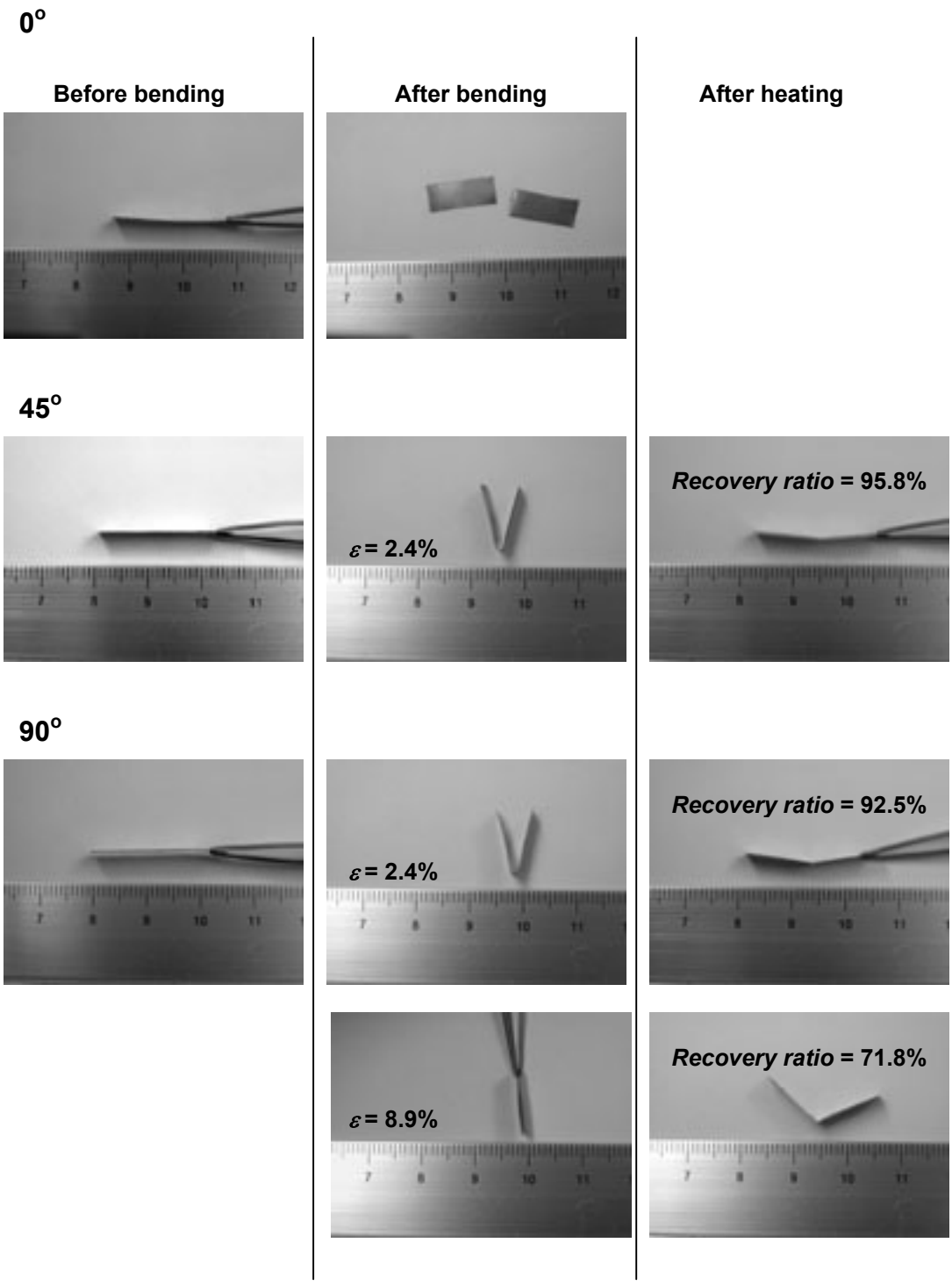

Figure 6.24 Photographs of the specimen of w_g = 0.7 mm with angles between cuts and the rolling direction being 0°, 45° and 90°.

6.3.6 Heat treatment

Figure 6.25(a) shows the DSC profile of the Ti-rich TiNi SMA before annealing. The SMA exhibited an R phase[4] transformation peak only when the SMA was cooling. The starting and finishing temperatures of R phase martensite crystal structure R_s and R_f were 334.9K and 315.7K, respectively. Then, when the SMA was heated, the starting and finishing temperatures of austenite crystal structure A_s and A_f were 318K and 344.8K, respectively. Figure 6.25(b) and (c) show the DSC profile of the SMA sheet annealed at 773K, and 1073K, respectively. In both cases, the transformation temperatures were similar. The temperatures of starting and finishing of martensite M_s and M_f were about 342K and 330K, respectively during cooling. A_s and A_f were 363K and 377K, respectively, during heating. It is found that the annealing process causes the transformation temperatures to rise by 10 to 20K, but they do not depend on the annealing temperature or the annealing time.

Figure 6.26 shows the results of recovery ratios with respect to the strain for the SMA sheet with and without annealing. Two things are found here. Firstly, the ductility of the SMA sheet is improved by annealing. The maximum surface strain of the specimen before annealing is 4.49%. After annealing at 773K and 1073K, it becomes 6.85% and 5.76%, respectively. Secondly, the shape memory effect is decreased by annealing. The recovery ratio of the specimen without annealing is 100%. The recovery ratio becomes less than 80% and 60% when the specimens are annealed at 773K and 1073K, respectively. Annealing at 1073K eliminated most of the dislocations in the materials, thus a permanent plastic deformation was introduced by the bending tests, leading to a poor shape recovery. Annealing at 773K resulted in an only partial elimination of dislocations, which gave an adequate deformability to the materials. As a result, the specimen annealed at 773K showed better shape recovery than that in the

[4] R phase represents a trigonal crystal structure of martensite phase (Otsuka, et. al 1998) .

specimen annealed at 1073K. Therefore it is a better to anneal the SMA sheet at 773K for 10 minutes.

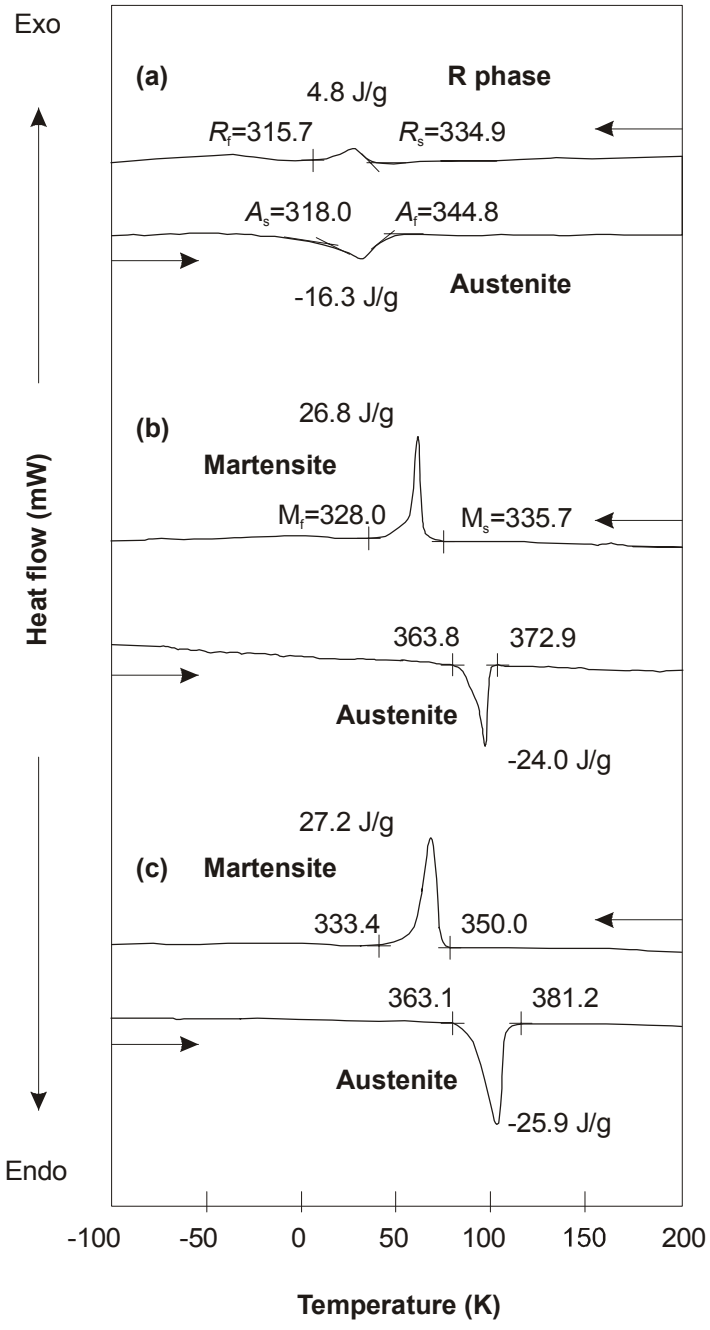

Figure 6.25 DSC profiles of Ti-rich TiNi SMA (a) before annealing, (b) annealed at 773K and (c) annealed at 1073K.

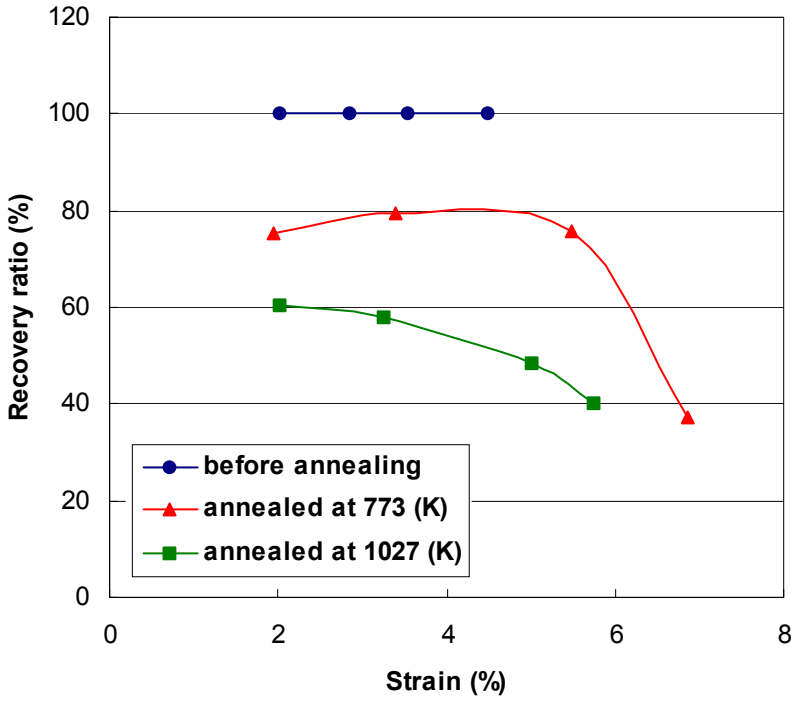

Figure 6.26 Recovery ratio vs. strain of the Ti-rich TiNi SMA with and without annealing.

6.4 Ti-rich TiNi shape memory alloy origami stent graft

In the previous sections, the pattern of the folds for the novel origami stent graft has been successfully etched into the Ti-rich TiNi SMA sheet, see Figures 6.18 and 6.19. Using the same sheet, the stent graft is produced. We now is examine whether it can be self-deployed when heated.

Consider the shape the Ti-rich SMA sheet. Its initial shape is flat. Therefore, it always reverts back to a flat shape when heated. However, to produce the stent graft it must be a cylindrical shape in its fully expanded configuration. The SMA sheet was therefore annealed to store the memory of the cylindrical shape. This annealing process was carried out at the same time as doing heat treatment for improving ductility of the SMA described in the previous section. The etched SMA sheet was constrained to a cylindrical shape by an aluminum tube and heat-treated at 773K for 10 minutes. After the annealing process the stent graft was then folded at room temperature. It was heated at 383K and its self-deployment was recorded using a digital video camera.

The result of the shape of Ti-rich TiNi SMA sheet after heat treatment is shown in Figure 6.27. The sheet becomes a cylindrical tube, as expected and designed. The opposite edges of the sheet were then connected by adhesive. The radius and length of the origami stent graft is 12.7 and 40 mm, respectively. The radius is the same size as the existing oesophageal and aortal stent grafts.

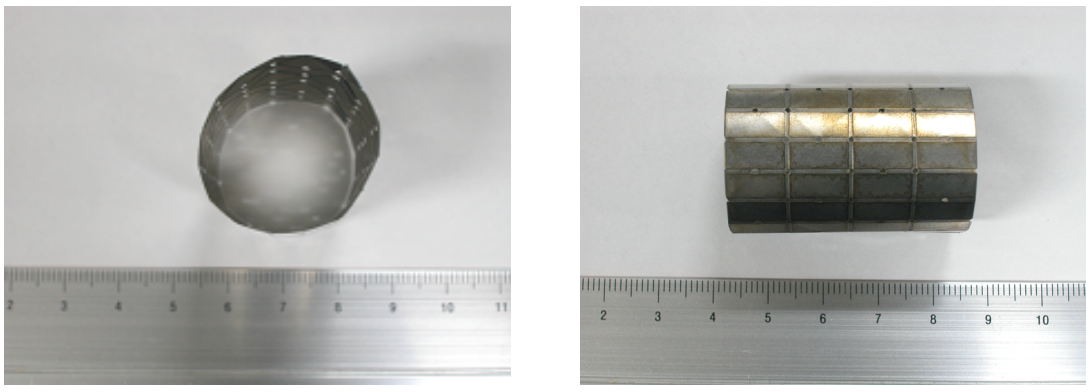

Figure 6.27 Ti-rich TiNi SMA tube produced by annealed at 737K.

As shown Figure 6.28(a) and (b), the origami stent graft has been folded successfully without forming any cracks. The radius and length of the stent graft is 6.25 and 25 mm, respectively, in the fully folded configuration. Figures 6.28(c)-(f) show a series of frames from a video recording, demonstrating the deployment process of the Ti-rich SMA stent. The folded origami stent graft was heated at 393K from the bottom, and it deployed gradually and recovered almost to the original cylindrical tube shape. It took about 14 seconds to expand to its fully expanded configuration. This demonstrates that it is possible to make a self-deployable stent graft using a Ti-rich TiNi SMA sheet. However, as shown in Figure 6.28(f) the origami stent graft could not recover completely to the original cylindrical tubular size. Several reasons can be considered.

Firstly, from the result shown in Figure 6.26, the recovery ratio of Ti-rich TiNi SMA reduces after annealing at 773K. Therefore, it is expected that the origami stent graft produced by the annealed SMA sheet could not recover completely when heated. Secondly, Figure 6.29(a) shows the photograph of the cross section of the folds of a stent. The surface strain of the fold is 13%, which is calculated by $(t/2R)\times 100$, where t is a thickness of the folds of 0.04 mm and R is a radius of 0.154 mm. The value is beyond the maximum value of the strain for which SMA is able to go back to its original shape. Thirdly, from the results of the bending test in Section 6.3.5, the etching line width is preferably more than 0.5 mm and in a direction either perpendicular or 45^{o} to the rolling direction. However, in this model the line width was 0.3 mm and it could not be etched in the ideal directions due to the design of the pattern of the folds of the origami stent graft. Furthermore, we now draw attention back to the value of the shortening of folds during deployment calculated in Chapter 3 and use the result in Figure 3.29. Going from one unstrained configuration to the other during deployment requires larger deformation and needs to have a force to jump from one to the other. Therefore, it could be assumed that the SMA stent graft did not have enough force to

expand it completely. Further investigation will be needed to understand behavior of folds during deployment.

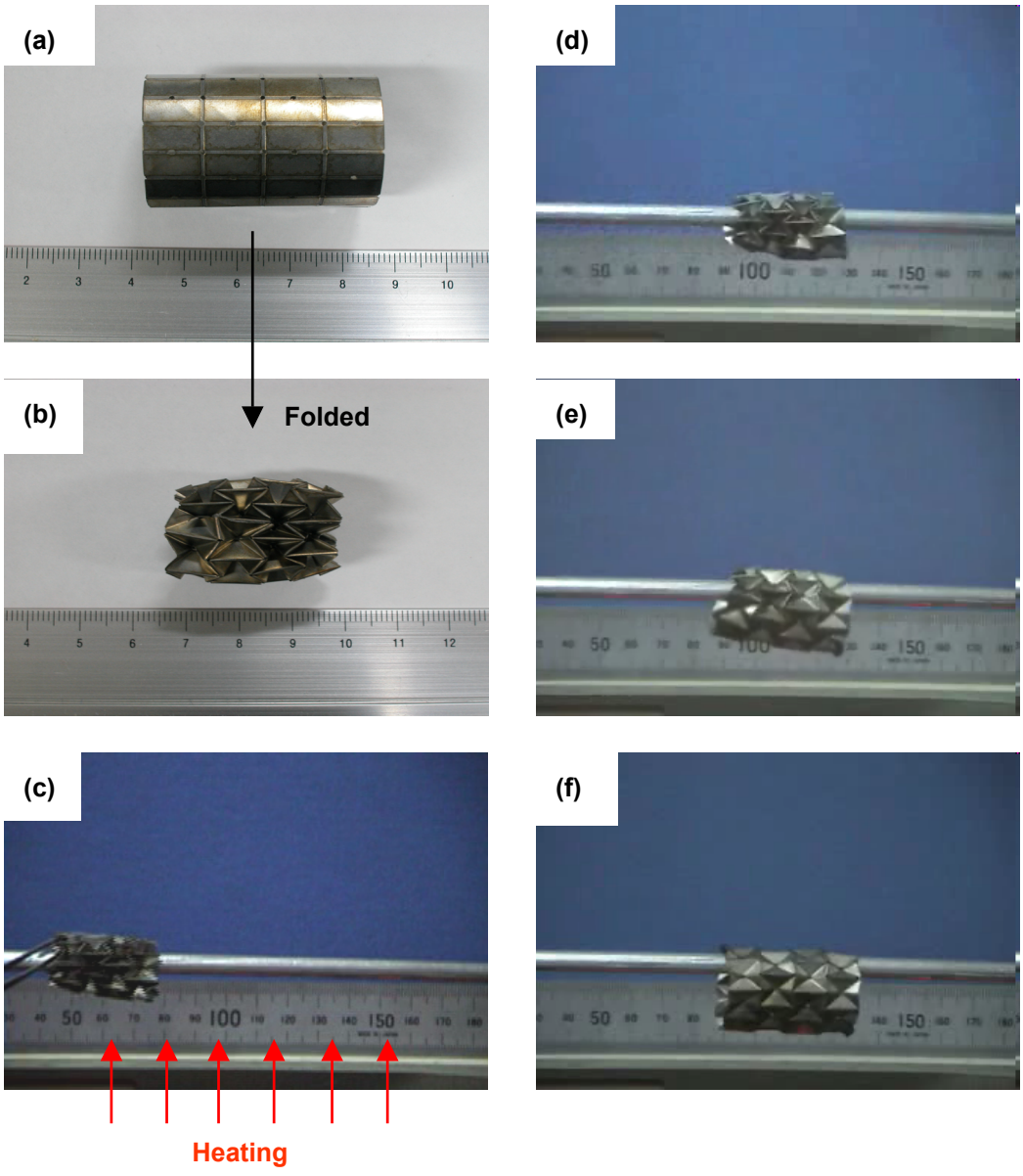

Figure 6.28 Shape change of the model stent. (a) The stent prior to being folded up; (b) folded at room temperature; and (c)–(f) development by heating at 393K.

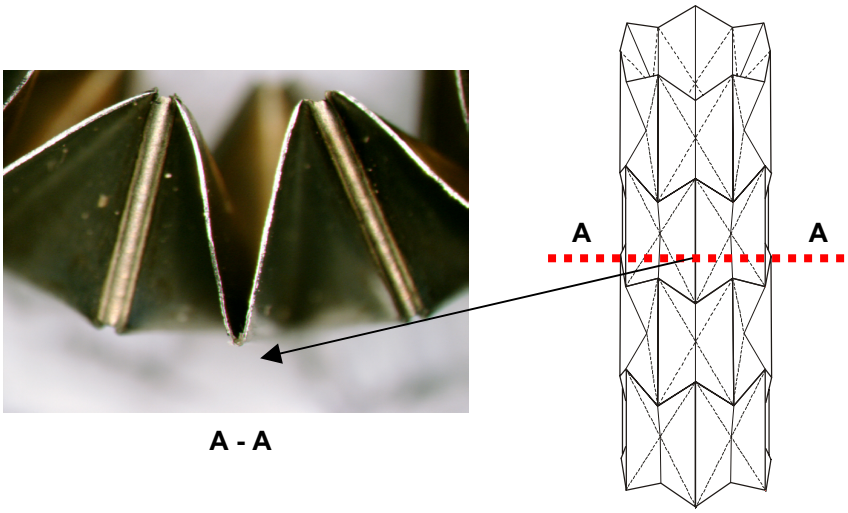

Figure 6.29 (a) Magnification of cross-section A-A.

6.5 Ni-rich TiNi shape memory alloy stent graft

Self-expansion of the stent graft using a commercially available Ti-rich TiNi SMA sheet has been demonstrated successfully, though with restrictions, in the previous section. However, the reverse transformation temperature, A_f of 383K is much too high. In medical applications, it should be near body temperature (about 309K). The use of TiNi SMA sheet with a Ni-rich composition solves this problem because the transformation temperature of Ni-rich SMA is adjustable to the temperature near that of a human body as described in Section 2.2.6, Chapter 2.

A sheet of Ni-rich (Ti-50.7at%Ni) TiNi alloy was supplied by Dr. Tsuchiya at Toyohashi University of Technology, Japan. The size of the sheet was 40 mm x 100 mm x 0.05 mm. It was produced by a new method of diffusion treatment (at 1073K for 72 hours) of ultrafine laminate sheet composed of 179 alternative layers of pure Ti (of 0.2 mm thickness) and pure Ni (of 0.12 mm thickness). A further advantage of this Ni-rich TiNi shape memory alloy sheet is that the sheet does not have a rolling direction

because the new process does not require rolling, which also reduces manufacturing cost. Details of this process and properties of the material are given by Tomus, et al (2003).

Using the negative etching method descried in Section 6.2.1, the pattern of the folds for the stent graft was etched into the Ni-rich TiNi SMA sheet. The folding patterns are the same as in Figure 6.7 except for the number of elements. The number of elements in vertical and longitudinal directions are 6 and 4, respectively. The size of the element was 10 mm x 10 mm and the central holes were 0.5 mm x 0.5 mm. The width of the folds was 0.3 mm. The etchant was the same mixture of $HF:HNO_3:H_2O$ as the etchant used to etch Ti-rich TiNi SMA sheet, but in the different proportion of 1:1:6 by volume because the etching process seemed to act more aggressively on the Ni-rich than it did on the Ti-rich TiNi SMA sheet. The thickness of the sheet of 0.05 mm was halved at the folds by the etching process.

After the etching, aging treatment was given at 773K for 40 hours to bring the transformation temperatures close to the body temperature. The transformation temperatures were measured by DSC with a cooling/heating rate of $0.17Ks^{-1}$. During the aging process, the sheet was constrained by an aluminum tube to store the memory of a cylindrical shape, so that the stent graft would return back to the cylindrical tube when heated.

The opposite edges of the sheet were connected by adhesive. The stent graft was cooled below M_f, then was folded and inserted into an acrylic tube of 13 mm diameter imitating a catheter. The folded stent was heated by warm air and its deployment was recorded using a digital video camera.

Figure 6.30 shows the results of the DSC profile of the Ni-rich TiNi SMA sheet after diffusion and aging treatments. There are transformation peaks on cooling and one on heating. The first peak, R^*_m at 290K, and the second one, M^* at 278K, on cooling can

be assigned for R phase and B19'[5] martensitic transformation temperature, respectively. Transformation temperatures are found to be determined as $R_s = 291$K, $M_f = 261$K, $A_s = 304$K and $A_f = 319$K. Therefore, the shape recovery will occur near body temperature.

The total etching time to reduce the thickness to half of its initial value was 16 minutes. Good folding patterns were produced by the negative etching technique. After etching, the sheet formed the cylindrical tubular shape subjected to the aging treatment. When the stent graft was folded, it had to be in martensite phase which is under M_f. As shown in Figure 6.30, M_f is 261K. Nitrogen was used to cool the stent graft to this temperature. Then folding of the origami stent was easily accomplished with no cracking. Before folding, the radius of the stent was 9.55 mm, which again, is suitable for use as an oesophageal or aorta stent graft.

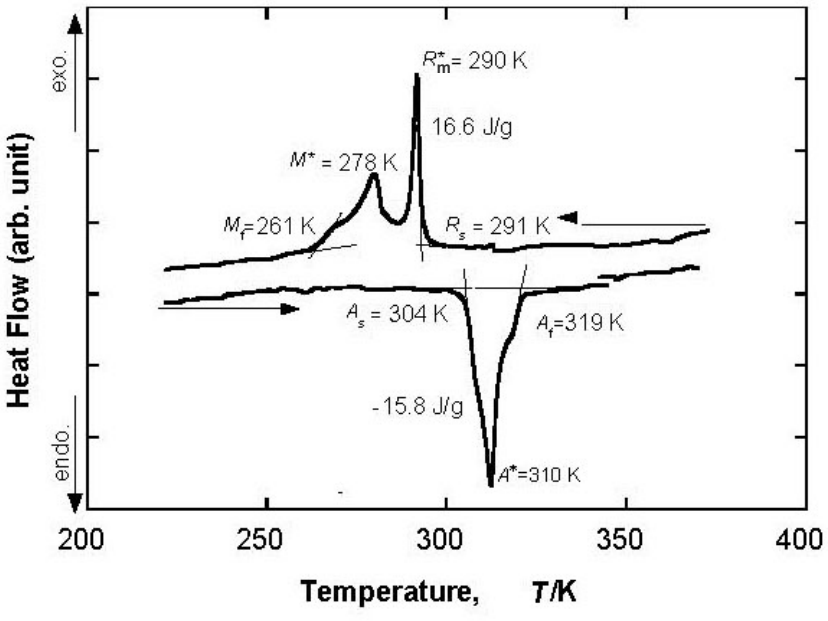

Figure 6.30 DSC profile of Ni-rich TiNi SMA after diffusion treatment at 1073K for 72 hours and aging process at 773K for 40 hours.

[5] B19' represents monoclinic crystal structures of martensite phase.

Figures 6.31 and 6.32 show two series of frames from the video recording, demonstrating the deployment process of the Ni-rich TiNi SMA stent. The folded origami stent graft was pushed into the acrylic tube of a larger radius (12.5 mm) imitating the oesophageal or aorta lumen. The inside of the larger radius tube was heated by warm air above A_f before the stent graft was inserted and it was heated from top and bottom as shown in Figure 6.31(b) during the deployment of the stent graft. As can be seen in Figure 6.31, both radius and length of the origami stent graft increase gradually. The end view of the deployment of the stent is shown in Figure 6.32. It took 32 seconds for it to expand to its fully expanded configuration after the small acrylic tube (i.e. catheter) was removed completely (Figure 6.32c). Again, it can be seen that the radius increase gradually and the expansion is roughly uniform. However, in the middle stage of the deployment, it becomes slightly distorted (Figure 6.32d and e). It may be a temporary distortion caused by uneven heating of the stent. In living tissue, a stent would be heated relatively evenly, thus uneven heating would be less of a concern.

This demonstrates that it is possible to make a self-expanding stent graft which can expand at near body temperature using a Ni-rich TiNi SMA sheet. However, as shown in Figures 6.31(i) and 6.32(i) the origami stent graft could not recover to the original cylindrical tubular shape completely. The maximum value of the strain of Ni-rich TiNi SMA where it is able to go back to the original shape is 3% (Tomus, et al. 2003). Therefore, it is assumed that the value of the strain of the stent graft is beyond the maximum recoverable strain.

All of the existing self-expanding stents are made from TiNi tubes and the mesh patterns are machined by laser cutting (Duerig, et al. 1999) and processing of TiNi tubes and laser cutting are both complex and expensive processes (Reynaerts, et al. 1996). However, in this study, the stent graft has been produced from TiNi sheet made by the ultrafine laminate method, and the folds have been patterned by a photochemical etching method, which are both simpler and cheaper.

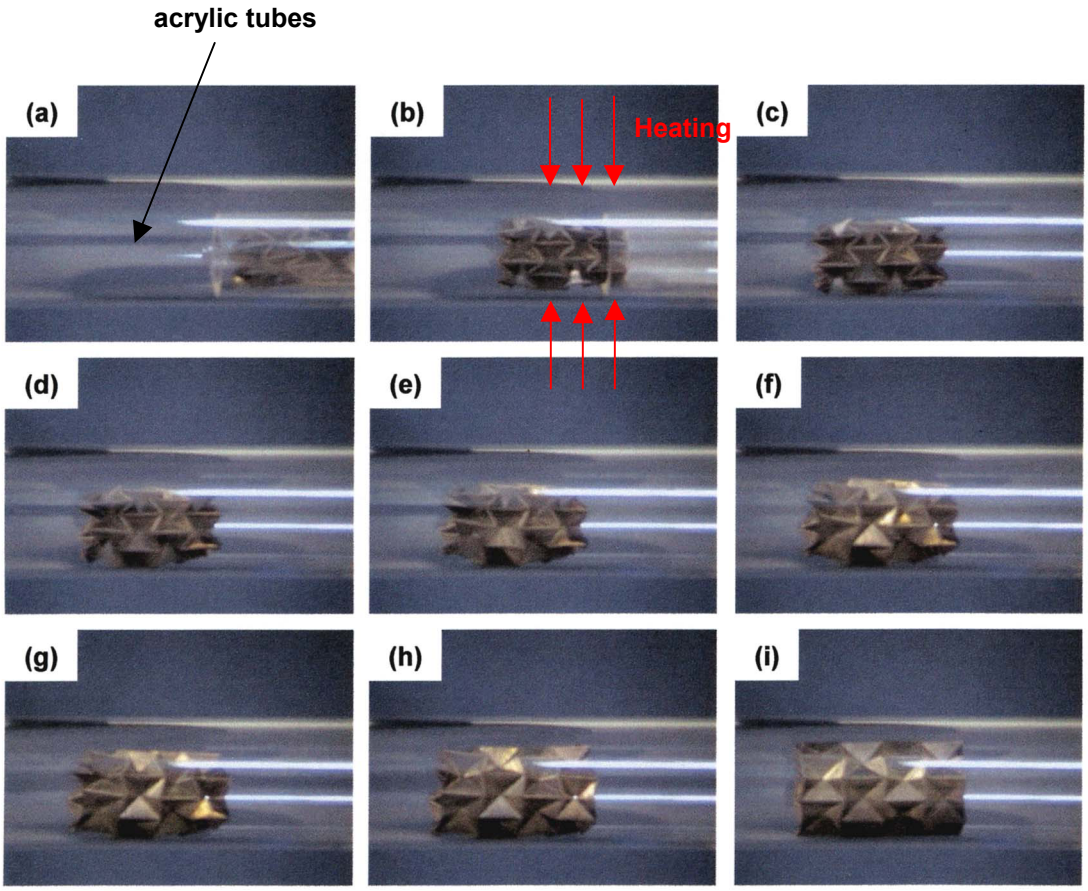

Figure 6.31 Series of video image showing: (a) Stent graft which is folded and backed into a small acrylic tube of 7.5 mm radius was inserted into another acrylic tube of 12.5 mm radius, (b) the small acrylic tube was removed and (c)-(i) the stent graft was self-expanding at above A_f (319K).

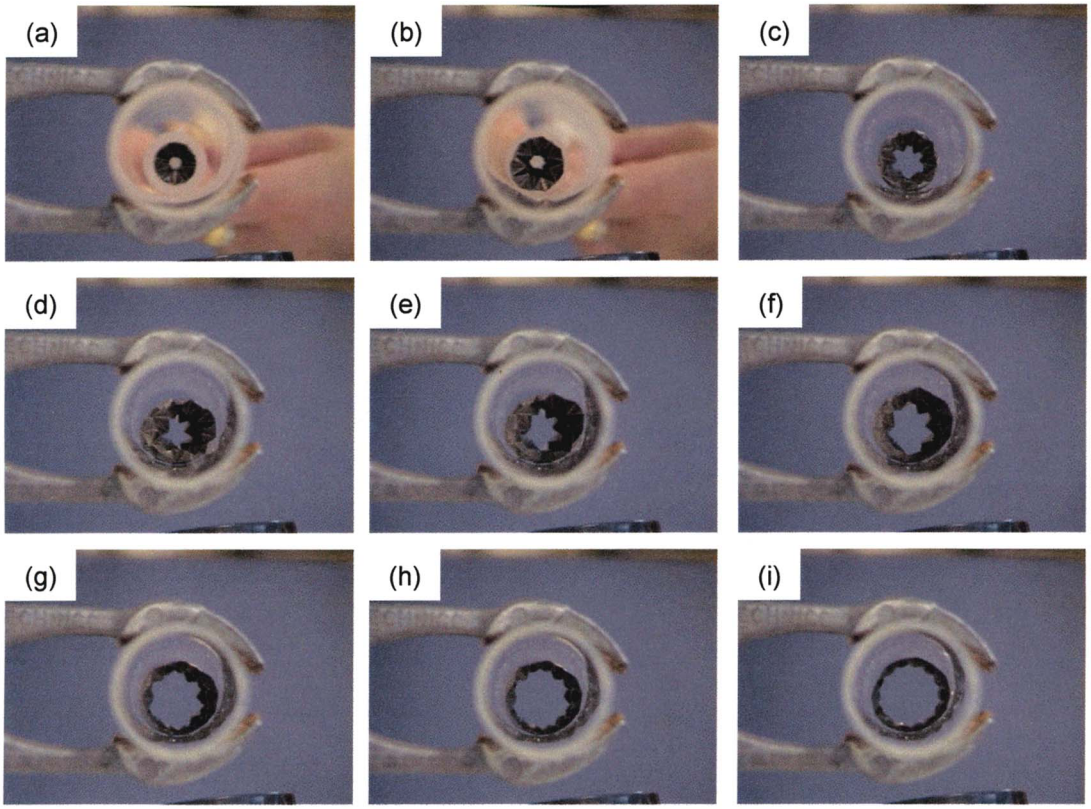

Figure 6.32 Self-deployment of the origami stent graft at end view. (a) Stent graft which is folded and backed into a small acrylic tube of 7.5 mm radius was inserted into another acrylic tube of 12.5 mm radius, (b) the small acrylic tube was removed and (c)-(i) the stent graft was self-expanding at above A_f (319K).

6.6 Conclusions

In this chapter methods to produce models of the origami stent graft using both stainless steel and SMA sheets have been established. The models have been produced successfully. Details of the results are as follows.

The chapter started by using stainless steel sheets, and testing methods to make folds in the metal. It has been found that grooves for the folds can be produced easily using photochemical etching which is a cost effective technique. It was also found using these stainless steel models that folding of the stents to its fully folded configuration could be easily accomplished by using a combination of well-directed radial forces, as well as a longitudinal compression. Such forces have been achieved (for other applications) using a press.

The second part of this chapter has been investigated using techniques such as etching and heat treatment on the development of stents from TiNi SMA sheets. It has been found that the both positive and negative photoresists with the chemical solution of $HF/HNO_3/H_2O$ can be applied. More dilute ratios of this solution (i.e. 1:1:4 or 1:1:6 by volume) are preferred, as the stronger solution (1:1:2) can cause lifting of the photoresist and undercutting of the grooves. From the results of heat-treatment, it has been found that ductility of the SMA sheet can be improved, although this has effects on the ability of the SMA to recover completely to its remembered shape

It has been demonstrated that both Ti-rich and Ni-rich TiNi SMA stent grafts will smoothly self-expand by heating. This is particularly relevant for the Ni-rich TiNi SMA sheet, since it will expand at near body temperature. However, both models could not recover to their original cylindrical tubular shapes completely, which was mainly because the folded stent graft is strained beyond the maximum recoverable strain of TiNi SMA sheets. Some improvement could be made by modifying the folding pattern, and depth and width of the etched grooves.

The working models presented here have shown that the concept of the origami stent graft can be achieved using existing biocompatible materials such as stainless steel and SMA sheets, and using readily available technologies such as photochemical etching.

CHAPTER 7

FINAL REMARKS

7.1 Main achievements

This dissertation concerns the structural design of stent grafts. A new type of stent graft has been developed which incorporates into a single piece both the wire mesh and the covering membrane which are found in traditional stent grafts. The new design consists of a folded sheet of material, and has its basis in the ancient Japanese art of origami, and is therefore termed the origami stent graft. The principal findings are summarised in the following paragraphs.

Firstly, a detailed symmetric design of a foldable cylindrical tube for the new stent graft has been presented. Folding is achieved by dividing the structure into a series of identical foldable elements. Particular attention has been paid to two types of elements: rectangular elements and general elements. Folding patterns for each type of element was obtained. Both patterns allow the stent graft to be folded and expanded both radially and longitudinally.

The relationships among the design of the elements, the number of elements in the circumferential and longitudinal directions and the folded dimensions of the stent graft have been derived. It has been found that compact folding in the radial direction can be achieved by increasing the number of circumferential elements. However, a large number of elements may cause manufacturing difficulty. A compromise can be found to address both concerns. It has also been found that the stent graft can be folded compactly in the longitudinal direction as both the number of the circumferential and

longitudinal elements increase, and that the ratio of its constriction depends on the design of the element.

We have also identified a geometric mismatch during deployment. The elements have to deform when the structure is expanded. Optimum designs which minimise the deformation have been found.

Variations to the general folding patterns of both cylindrical and conical tubes have also been discussed, though without detailed geometric calculation.

Secondly, we have found that it is possible to make a foldable cylindrical tube with helical folds. Helical folds are introduced by adjusting the joining position of the two edges of a sheet that had been symmetrically jointed in the symmetric design. The main advantages of the stent graft with helical folds over the symmetric ones are improvement to the radial strength of the stent graft and ease of the deployment process by synchronizing the deployment of each element. The relationships among the number of elements in one complete circumference of a helix, the helical angle and the radius of the helical type stent graft have been derived.

The locations for the helical folds are optimised for easy folding by considering both the geometric aspects of folding and the buckling patterns of a thin-walled tube under torsion, which have been found analytically. Physical models of the tube with prefabricated helical folds have been produced and then twisted by applying torques at both ends. The model confirms that the tube with the helical folds resembling buckling patterns could be folded more easily under torsion.

Thirdly, we carried out numerical analysis using FEM in order to understand the strain of the fold with respect to the different widths of fold. From the results, it is found that the circumferential strain becomes smaller as the width of the groove increases. However, the reduction of the strain becomes less obvious when the width is greater than 1.2 mm.

The FE analysis has also been used to identify the deformed pattern of a thin cylindrical tube under certain prescribed loads (displacements). The geometry of the

deformed pattern resembles the pattern of the folds of the designed foldable cylindrical tube. Therefore, the stent graft can be folded into the desirable shape easily if the groove is produced.

The FE analysis is also used to identify the accuracy of the geometric analysis in the presence of a mismatch. It is found that the geometric analysis and FEM techniques strongly agree with one another with regard to deployment radius, but weakly agree in assessing overall length.

Finally, the stent graft has been manufactured to verify the concept. A number of demonstration models of the stent graft, which are of the same size as standard oesophageal and aortal stent grafts, have been produced successfully. The same materials as used in current stent grafts, stainless steel and shape memory alloy were used, but the sheet form was used rather than the wire form.

The patterns of folds on the stainless steel sheet are produced by photochemical etching. It is found that folding of the models in its fully folded configuration is easily accomplished if the folds are pre-folded to the preferred direction of deformation. Process techniques of SMA, such as photochemical etching to engrave folds into both sides of the sheet and heat-treatment to add ductility and re-shape from sheet to tubular shape are established. Optimal condition for production of the stent grafts were obtained in terms of the type of photoresist and its thickness; UV exposure intensity and time; baking temperatures; proportion of $HF/HNO_3/H_2O$ of the etchant and the temperature of heat-treatment.

It has been demonstrated that stent grafts with Ti-rich and Ni-rich TiNi SMA self-expanded smoothly and gradually by heating. The stent graft with Ni-rich TiNi SMA sheet was designed to expand at near body temperature. The work has proved that the concept of a foldable cylindrical tube can be applied to produce the stent graft using existing biocompatible materials such as stainless steel and SMA sheets.

7.2 Future work

The concept of the origami stent graft is novel and has raised considerable interest. However, the design must be improved in order to produce a marketable and reliable product. The next step for development of this concept involves the production of a prototype for clinical trials. It is recommended that the initial work on the design be directed towards oesophageal applications, since the oesophagus is relatively large, with relatively easy access. The currently obtainable size of the origami stent graft would also make it useful for abdominal aortic aneurysms (AAA) and thoracic aortic aneurysms (TAA). Coronary stent grafts are much smaller, and the difficulties of miniaturising the present design for use in coronary arteries would be too great for the near future.

We have noted that the current design lacks flexibility. The fully deployed stent graft with both stainless steel and SMA are rigid. Instead of producing the stent graft with only metal, using other biocompatible materials such as Dacron (a polyester) or PTFE with reinforcement may improve flexibility. A metal reinforcing frame could be attached to one of these flexible materials along the folds of the origami stent graft so that the expansion behaviour is identical to that of single-piece stent graft. Material thickness and mechanical properties also need to be considered in order to obtain adequate mechanical support. Thicker material can provide higher stiffness but would reduce flexibility.

Adhesive has been used to connect the ends of a sheet in order to form a cylindrical tube. Instead of adhesive, spot welding may also be used. Another option may be to use a tube instead of a sheet. Several existing techniques for etching a cylindrical tube (Jackman, et al. 1999; Mineta, et al. 2001) can be applied to produce the origami stent graft. However, producing the grooves inside of the tube by etching may prove to be complicated. Future work should include the development of a fold pattern that would produce a stent from a single-sided etch. In this research, photochemical

etching is used to produce the stent graft since the etching is inexpensive, and the facility is available at Oxford University. However, there may be advantages of using other processing methods for the manufacture of stent grafts, such as laser cutting. The laser method may produce smooth edges, but the costs are relatively high. It is also possible to polish sharp edges using advanced etching techniques. Advantages and disadvantages for both processes should be investigated.

Techniques for folding and expansion of the stent also need to be considered and improved. For stainless steel stent grafts, an existing balloon expansion tool could be used. Further development involves manufacturing of a new Ni-rich TiNi SMA sheet whose reverse transformation temperature of A_f is lower than the body temperature to produce a self-expanding stent graft with superelastic behaviour. Radial force and strengths of the stent graft with various A_f during and after expanding need to be examined to produce the SMA stent graft which has enough force to open and hold a blocked organ and weaken wall in the human body.

For this research the focus has been on the use of the structure as a medical stent. However, consideration should be given to other foldable/expandable medical devices that could make use of this design, such as vena cava filters and resetting tools in orthopaedics.

REFERENCE

Adam, A., Dondelinger, R. F., Mueller, P. R., (1997), *Textbook of Metallic Stents*, ISIS Medical Media, Oxford.

Agrawal, C. M. and Clark, H. G., (1992), Deformation Characteristics of a Bioabsorbable Intravascular Stent, Journal Article, *Invest Radiol*, 27(12), pp.1020-1024.

Allen, D. M., (1986), *The Principles and Practice of Photochemical Maching and Photoethcing*, Adam Hilger.

Allen, D. M., Leong, T., Lim, S. H. and Kohl, M., (1997), Photofabrication of the Third Dimension of NiTi Shape Memory Alloy Microactuators, *SPIE*, 3225, pp.126-132.

Auricchio, F., Lorete, M. D. and Sacco, E., (2000), Finite-Element Analysis of a Stenotic Artery Revascularization Through a Stent Insertion, *Computer Methods in Biomechanics and Biomedical Engineering*, 4, pp.249-263.

Bashar, A. H., Kazui, T., Washiyama, N., Terada, H., Yamashita, K. and Haque, M. E., (2003), Mechanical Properties of Various Z-Stent Designs: an Endovascular Stent-Grafting Perspective, *Artif Organs*, 27(8), pp.714-21.

Buehler, W. J., Gilfrich, J. V., Wiley, R. C., (1963), Effect Low Temperature Phase Changes on the Mechanical Properties of Alloys near Composition Ti-Ni, *J. Appl Phs*, 34, pp.1475-1477.

Calladine, C. R., (1983), *Buckling of Cylindrical Shells in Torsion*, *Theory of Shell Structures*, Cambridge, Section 14.7, pp. 521-532.

Chen, J. Z. and Wu, S. K., (1999), Chemical Machined Thin Foils of TiNi Shape Memory Alloy, *Materials Chemistry and Physics*, 58(2), pp.162-165.

Chung, S. and Qadir, A., (1998), Endoscopic management of advanced oesophageal cancer, *Eur J Gastroenterol Hepatol*, 10(9), pp.737-739.

Chuter, T. A., (2002), Stent-graft design: the good, the bad and the ugly, *Cardiovasc Surg*, 10(1), pp.7-13.

Cowling, M. G., (2000), Stenting in the oesophagus, *Hosp Med*, 61(1), pp.33-36.

Cowling, M. G. and Adam, A., (1998a), Radiological management of oesophageal strictures, *Hosp Med*, 59(9), pp.693-7.

Cowling, M. G., Hale, H. and Grundy, A., (1998b), Management of malignant oesophageal obstruction with self-expanding metallic stents, *Br J Surg*, 85(2), pp.264-266.

Dake, M. D., Miller, D. C., Semba, C. P., Mitchell, R. S., Walker, P. J. and Liddell, R. P., (1994), Transluminal placement of endovascular stent-grafts for the treatment of descending thoracic aortic aneurysms, *N Engl J Med*, 331(26), pp.1729-1734.

Dolmatch, B. L. and Blum, U., (2000), *Stent-Grafts / current clinical practice*, Thieme.

Domschke, W., Foerster, E. C., Matek, W. and Rodl, W., (1990), Self-expanding mesh stent for esophageal cancer stenosis, *Endoscopy*, 22(3), pp.134-136.

Donnell, L. H., (1933), *Stability of thin-walled tubes under torsion*, NASA.479, pp. 95-116.

Donnell, L. H., (1951), *Buckling of thin cylinders under torsion*, *Beams, Plates, and Shells*, McGraw-Hill International Book Company, Section 7.4, pp. 416-432.

Drake, C., (2003), Aortic aneurysms, myoblast transplants focal points at meet, *BBI Newsletter*.

Duerig, T., Pelton, A. and Stockel, D., (1999), An overview of nitinol medical applications, *Materials Science and Engineering A*, 273-275, pp.149-160.

Dumoulin, C. and Cochelin, B., (2000), Mechanical behaviour modelling of balloon-expandable stents, *J Biomech*, 33(11), pp.1461-1470.

Dyet, J. F., Watts, W. G., Ettles, D. F. and Nicholson, A. A., (2000), Mechanical properties of metallic stents: how do these properties influence the choice of stent for specific lesions?, Journal Article, *Cardiovasc Intervent Radiol*, 23(1), pp.47-54.

Edelman, E. R. and Rogers, C., (1996), Hoop dreams. Stents without restenosis, *Circulation*, 94(6), pp.1199-202.

Esato, K., Hoshino, S., Ishimaru, S., N., M. and N., Z., (1999), *Stent-grafting and Aortic Diseases* (in Japanese), Ishiyaku-shuppan, Tokyo.

Etave, F., Finet, G., Boivin, M., Boyer, J.C., Rioufol, G. and Thollet, G., (2001), Mechanical properties of coronary stents determined by using finite element analysis, *Journal of Biomechanics*, 34(8), pp.1065-1075.

Fallone, B. G., Wallace, S. and Gianturco, C., (1988), Elastic characteristics of the self-expanding metallic stents, Journal Article, *Invest Radiol*, 23(5), pp.370-376.

Fischman, D. L., Leon, M. B., Baim, D. S., Schatz, R. A., Savage, M. P., Penn, I., Detre, K., Veltri, L., Ricci, D., Nobuyoshi, M. and et al., (1994), A randomized comparison of coronary-stent placement and balloon angioplasty in the treatment of coronary artery disease. Stent Restenosis Study Investigators, *N Engl J Med*, 331(8), pp.496-501.

Flueckiger, F., Sternthal, H., Klein, G. E., Aschauer, M., Szolar, D. and Kleinhappl, G., (1994), Strength, elasticity, and plasticity of expandable metal stents: in vitro studies with three types of stress, *J Vasc Interv Radiol*, 5(5), pp.745-750.

Friend, C. M. and Morgan, N. B., (1999), *Medical applications for shape-memory alloys (SMA)/organized IMechE*, Professional Engineering Publishing for the Institution of Mechanical Engineers.

Fushimi, K., (1980), Origami in Science (in Japanese).

Garasic, J. M., Edelman, E. R., Squire, J. C., Seifert, P., Williams, M. S. and Rogers, C., (2000), Stent and artery geometry determine intimal thickening independent of arterial injury, *Circulation*, 101(7), pp.812-818.

Gotman, I., (1997), Characteristics of metals used in implants, *J Endourol*, 11(6), pp.383-389.

Gottsauner-Wolf, M., Moliterno, D. J., Lincoff, A. M. and Topol, E. J., (1996), Restenosis-an open file, *Clin Cardiol*, 19(5), pp.347-356.

Gruntzig, A. R., Senning, A. and Siegenthaler, W. E., (1979), Nonoperative dilatation of coronary-artery stenosis: percutaneous transluminal coronary angioplasty, *N Engl J Med*, 301(2), pp.61-68.

Guest, S. D. and Pellegrino, S., (1992), Inextensional wrapping of flat membranes, *1st International Seminar on Structural Morpholgy*, Montpellier.

Guest, S. D., (1994a), *Deployable Structures: Concepts and Analysis*, D.Phil. dissertation, University of Cambridge.

Guest, S. D. and Pellegrino, S., (1994b), The folding of triangulated cylinders, Part I: Geometric considerations, *Journal of Applied Mechanics*, 61, pp.773-777.

Haferkamp, H., Paschko, S. and Goede, M., (2001), New Laser Machining Processes for Shape Memory Alloys, *Proc*. *SPIE*. 4232, pp. 94-101

Hiatt, B. L., Carter, A. J. and Yeung, A. C., (2001), The drug-eluting stent:
is it the Holy Grail?, *Rev Cardiovasc Med*, 2(4), pp.190-196.

Hilbert, D. and Cohn-Vossen, S., (1952), *Geometry and imagination*, New York.

Hills, K. S., Chopra, K. B., Pal, A. and Westaby, D., (1998), Self-expanding metal oesophageal endoprostheses, covered and uncovered: a review of 30 cases, *Eur J Gastroenterol Hepatol*, 10(5), pp.371-374.

Holton, A., Walsh, E., Anayiotos, A., Pohost, G. and Venugopalan, R., (2002), Comparative MRI compatibility of 316L stainless steel alloy and nickel-titanium alloy stents, *J Cardiovasc Magn Reson*, 4(4), pp.423-430.

Jackman, R. J., Brittain, S. T., Adams, A., Whitesides, S. and Whitesides, G. M., (1999), Three-Dimensional Metallic Microstructures Fabricated by Soft Lithography and Microelectrodepostion, *Langmuir*, 15, pp.826-836.

Jacobs, T., Teodorescu, V., Morrissey, N., Carroccio, A., Ellozy, S., Minor, M., Hollier, L. H. and Marin, M. L., (2003a), The endovascular repair of abdominal aortic aneurysm: an update analysis of structural failure modes of endovascular stent grafts, *Semin Vasc Surg*, 16(2), pp.103-112.

Jacobs, T. S., Won, J., Gravereaux, E. C., Faries, P. L., Morrissey, N., Teodorescu, V. J., Hollier, L. H. and Marin, M. L., (2003b), Mechanical failure of prosthetic human implants: a 10-year experience with aortic stent graft devices, *J Vasc Surg*, 37(1), pp.16-26.

Kahn, H., Huff, M., A and Heuer, H., (1998), The TiNi Shape-Memory Alloy and Its Applications for MEMS, *Journal of Micromechanics and Microengineering*, 8(3), pp.213-221.

Kawaguchi, S. and Ishimaru, S., (2002), *Therapeutic & Engineering* (in Japanese), 14(4), pp.210-213.

Kawasaki, T., (1998), *Rose*, *Origami and mathematics* (*Bara to Origami to Sugaku to*), (in Japanese), Morikita, Japan, pp. 122-159.

Kobayashi, H., Kresling, B. and Vincent, J., (1998), The geometry of unfolding tree leaves, *Proceedings of the Royal Society*, 265, pp.147-154.

Kohl, M., Quandt, E., Schubler, A. and Trapp, R., (1994), Characterization of NiTi shape memory microdevices produced by microstructuring of etched sheets or sputter deposited films, *4th Int Conf. on New Actuators*, pp. 317-320.

Kresling, B., (1995), Plant "Design": Mechanical Simulations of Growth Patterns and Bionics, *Biomimetics*, 3(3), pp.105-122.

Kuribayashi, K., (1989), Millimeter-sized Joint Actuator Using a Shape Memory Alloy, *Sensors and Actuators*, 20, pp.57-64.

Kurnik, R. and Martens, K., (2003), *Clinical Group - MIT students report at Biotechnology and Engineering lecture*

Kutryk, M. J. and Serruys, P. W., (1999), *Coronary stenting current perspectives*, Martin Dunitz, London, UK.

Labinaz, M., Zidar, J. P., Stack, R. S. and Phillips, H. R., (1995), Biodegradable stents: the future of interventional cardiology?, *J Interv Cardiol*, 8(4), pp.395-405.

Lipscomb, I. P. and Nokes, L. D., (1996), *The application of shape memory alloys in medicine*, MEP,

Livingstone, J.,http://www.livingstone.demon.co.uk/page11.html

Maeda, M., Timmermans, H. A., Uchida, B. T., Uchida, H., Keller, F. S. and Rosch, J., (1992), In vitro comparison of the spiral Z stent and the Gianturco Z stent, *J Vasc Interv Radiol*, 3(3), pp.565-9.

Makutani, S., Yoshioka, T., Uchida, H., Tanaka, T., Yoshimura, H., Ohishi, H., Iwasaki, S., Ide, K., Ueda, K. and Maeda, M., (2000), Experimental study of esophageal covered stent for prevention of migration: use of clay to simulate stenosis of the esophagogastric junction or anastomosis site, *Nippon Igaku Hoshasen Gakkai Zasshi*, 60(8), pp.434-8.

Makino, E., Shibata, T. and Allen, D., M., (1998), Electrochemical Photoetching of Rolled Shape Memory Alloy Sheets for Microactuators, *Journal of the Surface Finishing*, 49(8), pp.85-91.

Makino, E., Mistuya, T. and Shibata, T., (2000), Micromaching of TiNi shape memory thin film for fabrication of micropump, *Sensors and Actuators*, 79, pp.251-259.

Marks, L. S., Ettekal, B., Cohen, M. S., Macairan, M. L. and Vidal, J., (1999), Use of a Shape-Memory Alloy (Nitinol) in a Removable Prostate Stent, *Tech Urol*, 5(4), pp.226-30.

Matsumoto, A., (1999), *Stent grafts*, Tyugai igaku Tokyo.

Migliavacca, F., Petrini, L., Colombo, M., Auricchio, F. and Pietrabissa, R., (2002), Mechanical behavior of coronary stents investigated through the finite element method, *Journal of Biomechanics*, 35(6), pp.803-811.

Mineta, T., Mitsui, T., Watanabe, Y., Kobayashi, S., Haga, Y. and Esashi, M., (2001), Batch fabricated flat meandering shape memory alloy actuator for active catheter, *Sensors and Actuators A*, 88, pp.112-120.

Mitchell, R. S., (1997), Endovascular stent graft repair of thoracic aortic aneurysms, Journal Article, *Semin Thorac Cardiovasc Surg*, 9(3), pp.257-68.

Miura, K., Sakamaki, M. and Suzuki, K., (1980), A novel design of folded map., *Congress of the International Cartographical Association*, Tokyo, Japan.

Miura, K., (1993), Concepts of deployable space structures, *Int J Space Struct*, 8, pp.3-16.

Miura, K., (2002), PCCP shells, *New Approaches to structural mechanics, shells and biological structures*, pp.329-339.

Moorleghem, W., V., Chandrasekaran, M., Reynaerts, D., Peirs, J. and Brussel, H., V., (1998), Shape memory and superelastic alloys: the new medical materials with growing demand, *Biomed Mater Eng*, 8(2), pp.55-60.

Nojima, T., (1999), Modelling of folding patterns in flat membrances and cylinders by using origami (in Japanese), *JSME*, 66(643), pp.354-359.

Obermeier, E. and Thielicke, E., *Microactuators and their technologies*, http://mat.ee.tu-berlin.de/papers/public00/pdf00/Thi00_1.pdf

Otsuka, K. and Wayman, C., M., (1998), *Shape Memory Materials*, Cambridge University Press, UK

Parodi, J. C., Palmaz, J. C. and Barone, H. D., (1991), Transfemoral intraluminal graft implantation for abdominal aortic aneurysms, Journal Article, *Ann Vasc Surg*, 5(6), pp.491-499.

Phillips, P. S., Kern, M. J. and Serruys, P. W., (1998), *Stenter's Notebook*, Physician's Press, U.S.A.

Prendergast, P. J., Lally, C., Daly, S., Reid, A. J., Lee, T. C., Quinn, D. and Dolan, F., (2003), Analysis of prolapse in cardiovascular stents: a constitutive equation for vascular tissue and finite-element modelling, *J Biomech Eng*, 125(5), pp.692-699.

Reynaerts, D., Peirs, J. and Brusse, H. V., (1996), Design of a shape memroy actuated gastrointestinal intervention system, *Actuator 96, 5th Int. Conf. New Actuators*.

Rieu, R., Barragan, P., Masson, C., Fuseri, J., Garitey, V., Silvestri, M., Roquebert, P. and Sainsous, J., (1999), Radial force of coronary stents: a comparative analysis, *Catheter Cardiovasc Interv*, 46(3), pp.380-391.

Rogers, C. and Edelman, E. R., (1995), Endovascular stent design dictates experimental restenosis and thrombosis, *Circulation*, 91(12), pp.2995-3001.

Rogers, C., Tseng, D. Y., Squire, J. C. and Edelman, E. R., (1999), Balloon-artery interactions during stent placement: a finite element analysis approach to pressure, compliance, and stent design as contributors to vascular injury, *Circ Res*, 84(4), pp.378-383.

Roseveare, C. D., Patel, P., Simmonds, N., Goggin, P. M., Kimble, J. and Shepherd, H. A., (1998), Metal stents improve dysphasia, nutrition and survival in malignant oesophageal stenosis: a randomized controlled trial comparing modified, Eur J Gastroenterol Hepatol, 10(8), pp. 653-657.

Ryhanen, J., (1999), *Biocompatibility evaluation of nickel-titanium shape memory metal alloy*, Ph.D. dissertation, University of Hospital of Oulu.

Saburi, T., (1998), *Ti-Ni shape memory alloys*, *Shape Memory Materials*, Cambridge University Press, Cambridge, UK, pp. 49-96.

Schetky, L., M., (1979), Shape-Memory Alloys, *Scientific American*, 241(5), pp.74-82.

Schrader, S. C. and Beyar, R., (1998), Evaluation of the compressive mechanical properties of endoluminal metal stents, *Cathet Cardiovasc Diagn*, 44(2), pp.179-87.

Schwertz, D. W. and Vaitkus, P., (2003), Drug-eluting stents to prevent reblockage of coronary arteries, *Cardiovasc Nurs*, 18(1), pp.11-6.

Serruys, P. W., de Jaegere, P., Kiemeneij, F., Macaya, C., Rutsch, W., Heyndrickx, G., Emanuelsson, H., Marco, J., Legrand, V., Materne, P. and et al., (1994), A comparison of balloon-expandable-stent implantation with balloon angioplasty in patients with coronary artery disease, *N Engl J Med*, 331(8), pp.489-95.

Skrobanek, K., D.,, Hagena, O., F., and Kohl, M., (1998) *Entwicklung von Mikromembranaktoren mit NiTi Formgedachtnislegierungen*, http://bibliothek.fzk.de/zb/berichte/FZKA6052.pdf

Smith, R., B., (2002), As the stent market heats up, so does litigation, *Mass High Tech, The Journal of New England Technology*, 20(14).

Sogame, A. and Furuya, H., (1998), Conceptual study on cylindrical deployable space structures, IUTAM-IASS Symposium on Deployable Structures: Theory and Applications, pp. 383-392

Stoeckel, D., (2000), Nitinol medical devices and implants, *Minimally invasive therapy and allied technologies*, 9(2), pp.81-88.

Takeuchi, S. and Shimoyama, I., (2000), A Three-Dimensional Shape Memory Alloy Microelectrode with Clipping Structure for Insect Neural Recording, *Journal of Microeletromechanical Systems*, 9(1), pp.24-31.

Tamai, H., Igaki, K., Kyo, E., Kosuga, K., Kawashima, A., Matsui, S., Komori, H., Tsuji, T., Motohara, S. and Uehata, H., (2000), Initial and 6-month results of biodegradable poly-l-lactic acid coronary stents in humans, Journal Article, *Circulation*, 102(4), pp.399-404.

Timoshenko, S. P. and Gere, J. M., (1961), *Buckling of Shells*, *Theory of Elastic Stability*, Section 11.11, pp. 457-509.

Tomus, D., Tsuchiya, K., Inuzuka, M., Sasaki, M., Imai, D., Ohmori, T. and Umemoto, M., (2003), Fabrication of shape memory TiNi foils via Ti/Ni ultrafine laminates, *Scripta Materialia*, 48, pp.489-494.

Watson, A., (1998), Self-expanding metal oesophageal endoprostheses: which is best?, *Eur J Gastroenterol Hepatol*, 10(5), pp.363-365.

Wey, J., Chan, C., Ouadros, E., Sergie, Z., Sousa, J. and Hang, L., (2003), *Abdominal Aortic Aneurysm - Brown University students reports at BioMed lecture*

You, Z., (1994), *Deployable Structures for Masts and Reflector Antennas*, D.Phil. dissertation, University of Cambridge.

You, Z. and Pellegrino, S., (1997), Foldable bar structures, *Int. J. Solids Structures*, 34(15), pp.1825-1847.

Appendix

The design of the stent graft presented in this dissertation has been submitted for a patent to cover the U.K, U.S.A, EU and Japan supported by ISIS Innovation Ltd. (Kuribayashi and You, PCT/GB02/01424 – "Deployable Stent", filing date: 27 March 2002). A spin out company from the University of Oxford called "Origami Instruments Ltd." will be set up in 2004 to explore this invention.